COUPLED CAVITY OPTOMECHANICAL SYSTEMS

A Dissertation

Presented to the Faculty of the Graduate School

of Cornell University

in Partial Fulfillment of the Requirements for the Degree of

Doctor of Philosophy

by

Mian Zhang

August 2015

COUPLED CAVITY OPTOMECHANICAL SYSTEMS

Mian Zhang, Ph.D.

Cornell University 2015

In the 70s, the interplay between microscale electronics and mechanics gave birth to micro- and nanoelectromechanical systems (MEMS/NEMS) that are prevalent in our daily life. The emergence of silicon photonics in the 90s was a result of the marriage between microelectronics and optics promising extreme communication bandwidth and processing power. A few years ago, the field of microscale optomechanics that harnesses the interaction between light and mechanics on a nanoscale emerged. The field witnessed the birth of many exciting technologies as quantum limited detection of ultra-weak forces, preparation of micromechanical oscillators close to their motional quantum ground states and enabling self-sustaining oscillations of mechanics with light.

The aim of this thesis is to explore and address a few challenges in coupled optomechanical systems. So far, most work in this area focuses on single device behaviors. One could imagine that like connecting many transistors together leads to complex computing machines, a network of coupled optomechanical devices have the potential to offer dynamics that are not accessible with single optomechanical devices. In this thesis, I show that indeed, light can be used to *synchronize* arrays of mechanical oscillators even when they are not physically connected.

I will also show in this thesis that coupling distinct optical and mechanical elements together could also enable a new paradigm of devices. We couple a single Carbon Nanotube (CNT) strongly to on-chip high-Q optical microcavi-

ties. Despite the tiny size of CNT, we show that the optical microcavity is still extremely sensitive to the CNT motion. We demonstrate that we can observe in real-time the thermal Brownian motion of a single CNT for the first time. The unique carbon-optical system also enables an almost completely dissipative optomechanical system that has not been achieved in any other type of systems to date.

BIOGRAPHICAL SKETCH

Mian Zhang grew up in Xi'An, China. He travelled to the UK after eighteen-years in China to complete his undergraduate studies in physics in the University of Bristol. During his undergraduate studies, he spent the third year in Rutherford Appleton Laboratory to learn ultrafast spectroscopy and optical tweezers. He later entered the Applied and Engineering Physics department at Cornell University to pursue the M.S/Ph.D. program under supervision of Prof. Michal Lipson. During his Ph.D., he worked on a variety of projects ranging from photodetectors, optomechanics, accelerometers and more recently nanophotonics concepts applied in neuroscience. He is heading to Harvard University as a postdoctoral fellow in Applied Physics this September to further sharpen his skills and broad his vision.

This thesis is dedicated to my parents.

ACKNOWLEDGEMENTS

My advisor Professor Michal Lipson has a tremendous positive influence towards me during my five and half years of study at Cornell. Her far reaching vision and yet down-to-earth approach always inspires me. I am grateful for the luxurious freedom I enjoyed as a Ph.D. student of her to work on several different projects while keeping a big picture, thanks to her openness and constant support through out the years. I would like to emphasize this incredible consistency on her side while myself have gone through better and worse times. Her constant action of support and encouragement impacts me above and beyond my Ph.D. career.

I would like to thank Professor Alex Gaeta, Professor Richard Rand and Professor Paulo Nussenzveig for being my committee members. I had many inspiring discussions with them throughout the years and many ideas and projects came as a result of such wonderful discussions. I would also like to thank Professor Paul McEuen who has been encouraging and critical about our collaboration project. In addition, I would like to thank other faculty members who supported my research and learning at Cornell, in particular Professor David Muller, Professor Chris Xu, Professor Farhan Rana and Professor Al Molnar.

Great thanks to the entire Cornell Nanophotonics Group (CNG), for being wonderful colleagues and friends over the years. This group is hard-working, intelligent, supportive and fun. My first thank goes to Professor Gustavo Wiederhecker, who was a postdoc in the group when I joined, for leading me into the field of cavity optomechanics. I am always impressed by his breadth as well as depth of knowledge and his ability to seemingly be able to solve nearly *everything* with Mathematica. Special thanks goes to other senior members of the group, Dr. Carl Poitras, Dr. Kyle Preston, Dr. Nick Sherwood, Dr. Arthur

Nitkowski, Dr. Mohammad Soltani, Dr. Biswajeet Guha, Dr. Lian-Wee Luo, Dr. Lucas Gabrielli, Dr. Hugo Lira, Dr. Jacob Levy, Dr. Michael Menard and Dr. Sasikanth Manipatruni. They have been a source of tremendous help and encouragement in the beginning of my Ph.D.

I would also like to thank current members in CNG. Shreyas Shah has been my major collaborator during my Ph.D. studies. His creativity and enthusiasm have been a constant source of energy that led to the fruitions of our challenging research. I would like to thank Dr. Jaime Cardenas, Dr. Rapheal St-Gelais, Dr. Lawrence Tzuang, Dr. Yoon-Ho Lee, Dr. Austin Griffith, Renato Domeneguetti, Moshe Zadka, Aseema Mohanty, Dr. Amin Tadayon, Dr. Felippe Barbarosa, Kevin Luke, Romy Fain, Chris Phare and Avik Dutt. It is great to have become colleagues and friends with you and I had great pleasure working with you. To the newer members of the group, Brain Stern, Brain Lee, Ipshita Datta, William Ji, Gaurang Bhatt, it has been fantastic to know you and I wish you all the success in future.

Special thanks to my collaborator Dr. Arthur Barnard. His knowledge of physics, technical expertise and dedication never cease to amaze me. It has been a very nurturing and productive collaboration with him.

I am extremely grateful for administrative support I received during my study at Cornell. Special thanks to Kim Cotton, Robert Roy, Cynthia Reynold, Sue Bulkley, Scott Coldren and Renee King.

Finally, I would like to thank my parents, Jianxun Zhang and Kangmin Ji, for their constant loving and support. I would also like to thank all my friends in the US and in China who have always been encouraging and supportive through out my years at Cornell.

TABLE OF CONTENTS

LIST OF TABLES

LIST OF FIGURES

CHAPTER 1

INTRODUCTION

Scaling played a paramount role in the development of modern technology. The emergence of microelectronics revolutionized signal processing and computing. Advanced fabrication techniques have led to an explosion of industrial and scientific research in the field of micro- and nanoelectromechanical (MEMS/NEMS) devices where microelectronics is combined with micromechanics [1]. MEMS enabled technology includes advanced navigation systems, high precision clocks and accelerometers. Combining microelectronics with photonics on the other hand, enabled the field of nanophotonics and optoelectronics devices [2]. For example, silicon photonics promises unparalleled bandwidth for on-chip data communication [3]. In recent years, a new field of optomechanics has emerged where light is controlled to interact with mechanics [4]. The scaling down of optical and mechanical devices push the devices into a regime where the force of light could control and alter the mechanics and vice versa. The field of optomechanics and optoelectromechanics, which I will discuss in this thesis, will be a integral part of future on-chip devices.

An optomechanical resonator consist of an optical and a mechanical resonator. The optical and mechanical degrees of freedoms are coupled such that the change of one influence the other. The first discussion of the optomechanical effect was by Braginsky in 1969 [5], where he discussed the radiation pressure, or the optical force interacting with a movable mirror. A typical representation of optomechanical system consists of an optical cavity formed by two opposite facing mirrors (a Fabry-Perot cavity) with one of the mirror free to move. The movable mirror is attached to a mechanical spring.

In a Fabry-Perot optical cavity, light can only be coupled into the cavity if the length of the of the cavity (L) is a half-integer multiple of the wavelength of the light (λ_l) ($L = \frac{1}{2}n\lambda_l, n \in 1, 2, 3, ...$). When such matching condition occurs, light passes multiple trips around the cavity and leads to energy build up in the cavity. In each reflection, the momentum of the light changes sign and due to the conservation of momentum, the mirror must absorbs the same amount of momentum. This leads to the motion of the mirror. As the mirror displaces by δx, the displaced cavity length is changed ($L_d = L + \delta x$). The optical resonant condition is no longer satisfied and the optical energy leaks out of the optical cavity. As the optical energy and the optical force in the cavity reduces, the mechanical spring brings the mirror back in its original position. The light energy builds up and the cycle repeats.

The first merit of cavity optomechanics provide is its high displacement sensitivity. Laser light which is often used to excite the optical cavity is the 'quietest' source as it may only be limited by the noise of the vacuum. This means that when the mechanical object makes a tiny displacement, there will be a footprint on the optical transmission signal as long as the induced amplitude or phase change of the light is above the quantum noise floor. It is not uncommon to reach sub fm/ $\sqrt{\text{Hz}}$ sensitivity in typical integrated optomechanical devices [6].

On the other hand, the interaction between the optical and mechanical degrees of freedom can lead to accurate control of nanomechanical devices, such as amplification and damping of the mechanical mode. Recently, it has been shown that light can cool (coherent damping) a mechanical mode to its ground state [11] and quantum coherent coupling is possible between light and the mechanical degree of freedom [12]. The quantum nature of light and the long

coherence time of micromechanical resonators may become an essential component for on-chip quantum information processing. The amplification in optomechanics can lead to self-sustaining oscillations of the mechanical oscillator when only driven by continuous-wave lasers, which is promising for compact frequency sources and mass sensing.

In this thesis, we explore the high sensitivity and the novel dynamics of optomehcanical system in two parts. For the optomechanical dynamics part, we study microscale double-disk optomechanical resonators and show that distant and dissimilar mechanical resonators can be synchronized to oscillate at the same frequency coupled only through light. The second part of the thesis address a unique enabling technology where we study the real-time dynamics of a single carbon nanotube (CNT) only a few nanometers in diameter by coupling it strongly to a high quality factor and high finesse optical microcavity.

1.1 Thesis Organization

We give a brief background in chapter 2 of the concept of cavity optomechanics that is used in this thesis. Chapter 3 describes our effort on achieving high mechanical quality factor in a double-disk optomechanical resonator. Chapter 4 discusses synchronization of two such devices coupled evanescently through the optical field. We show in chapter 5 that synchronization can be achieved in a much larger array of optomechanical resonators which means it is scalable. In chapter 6, we couple a single suspended CNT to the near field of a high finess optical cavity and show that we can monitor the mechanical vibrations of a single CNT in real-time.

CHAPTER 2

THEORETICAL BACKGROUND

We start our discussion of cavity optomechanics from whispering gallery mode (WGM) optical resonators, as all work in this thesis somewhat revolves around WGM optical resonators. The name WGM is originated from sound waves travelling along the walls of Whispering Gallery of St Paul's Cathedral. Optical waves can be trapped inside a circular high index dielectric medium just like the sounds waves can be trapped in the walls via total internal reflection. The optical medium can be in the form such as a sphere, a disk or a ring. When a propagating optical wave completes a round trip and travels back to its starting point, if it interferes constructively with itself, an optical resonance is formed. The discrete wavelengths where the resonances occur are called the optical resonant wavelengths. We call these resonances the *optical modes* of the cavity. The spatial-temporal geometry of the WGMs can be explicitly solved from Maxwell's Equations [7], but here we shall focus on the mode dynamics of the WGMs by simply denoting an optical mode as $a_m(t)$, which is the mth complex modal amplitude of the optical cavity. We further abbreviate the notation by removing m as we mostly work with only one resonance in the experiments described in this thesis.

2.1 Classical Equations for an Optomechanical Resonator

The beauty of working with the complex modal amplitude a is that one can analyze an optical system using coupled mode theory [8]. Under the rotating wave approximation, which assumes that the laser excitation wavelength is close to

the optical resonant frequency ($\omega_L \sim \omega_o$), the evolution of an optical resonant mode can be expressed as

$$\dot{a} = i(\omega_L - \omega_o)a - \frac{\gamma}{2}a + \sqrt{\gamma_{\text{ext}}}s \tag{2.1}$$

where γ is the optical loss rate, γ_{ext} is the external optical coupling rate, and s is the time dependent input optical amplitude with $P_{\text{in}} = |s|^2$.

The mechanical displacement x of any dielectric material interacting with the optical field, such as the cavity itself or an external object, can couple to the optical mode of the cavity through perturbing the optical resonant frequency ω (and even the damping rate γ as we shown later in the thesis). A measure for the strength of this interaction is the optomechanical coupling rate $g_{\text{om}} \equiv \frac{d\omega}{dx}$. Equation 2.1 now becomes

$$\dot{a} = i(\Delta + g_{\text{om}}x)a - \frac{\gamma}{2}a + i\sqrt{\gamma_{\text{ext}}}s \tag{2.2}$$

where $\Delta = \omega_L - \omega_o$ is the laser cavity detuning. At the same time, the optical field exert a force on the mechanical object with the magnitude $F_{\text{opt}} = \frac{dU}{dx}$ where $U = |a|^2 = N\hbar\omega$ is the total energy of N photons inside the cavity. The optical force has a magnitude of

$$F_{\text{opt}} = \frac{dU}{dx} = N\hbar\frac{d\omega}{dx} = \frac{|a|^2}{m\omega}g_{\text{om}} \tag{2.3}$$

The master equation that governs the mechanical object is then

$$\ddot{x} + \Gamma x + \Omega^2 x = \frac{g_{\text{om}}}{\omega}|a|^2 \tag{2.4}$$

Equations 2.2 and 2.4 fully describes the classical dynamics of a single optomechanical resonator.

2.2 Dynamical Back-actions

An optomechanical resonator can be understood as two second order linear systems with parametric (mechanical to optical) and nonlinear (optical to mechanical) coupling. Such coupling leads to interesting dynamical effects including the optical spring effect and heating and cooling of mechanical vibration modes. Our resonators work in the so called unresolved-sideband limit (USL) where the mechanical frequency is much less than the cavity damping rate ($\Omega << \gamma$). Physically, USL means the optics reaches equilibrium much faster than the mechanics. In this regime, we can analyze the dynamical effect between the optical and mechanical degree of freedoms by making some approximations to equations 2.2 and 2.4. We assume that the optics reaches the steady state with $\dot{a} = 0$. Equation 2.2 can then be explicitly solved for $a(x)$,

$$a(x) = i\frac{\sqrt{\gamma_{\text{ext}}}s}{i(\Delta + g_{\text{om}}x) - \frac{\gamma}{2}} \tag{2.5}$$

plug this into equation 2.2, we get

$$\ddot{x} + \Gamma x + \Omega^2 x = \frac{g_{\text{om}}}{m\omega}\frac{\gamma_{\text{ext}}|s|^2}{(\Delta + g_{\text{om}}x(t-\tau))^2 - \left(\frac{\gamma}{2}\right)^2} \tag{2.6}$$

Notice that we include a delay τ in the displacement on the RHS of the equation above. Although τ is much smaller than the mechanical period, the delay cannot be omitted in the analysis because it gives rise to the optical damping and amplification effect. This can be visualized by performing a retardation expansion of equation 2.6 with $x(t-\tau) \sim x(t) + \frac{2}{\gamma}\dot{x(t)} + O(\ddot{x(t)})$ where the delay is approximated by the optical cavity life time $\tau \sim \frac{2}{\gamma}$. The mechanical equation now reads

$$\ddot{x} + \Gamma' x + \Omega'^2 x = 0 \tag{2.7}$$

where

$$\Delta\Gamma = \Gamma' - \Gamma = -\frac{16 g_{\mathrm{om}}^2 s^2 \gamma_{ext}^2 \Delta}{m\gamma((\gamma/2)^2 + \Delta^2)^2 \omega_0}, \Delta\Omega = \Omega' - \Omega = \frac{8 g_{\mathrm{om}}^2 s^2 \gamma_{ext}^2 \Delta}{m\Omega((\gamma/2)^2 + \Delta^2)^2 \omega_0} \quad (2.8)$$

$\Delta\Gamma$ describe the optical induced damping and amplification of the mechanical resonator and $\Delta\Omega$ is the optomechanical spring effect. This approximation is somewhat oversimplified but nevertheless capture the essential dynamics that is relevant for the discussion in this thesis.

We introduce two ways to understand the physics of the optomechanical damping/gain and spring effect: a feedback picture and a scattering picture. In the feedback picture, the sign of the laser detuning determines whether the optical response lead or lag the mechanical motion. The optical response is retarded with respect to the mechanical motion because the optical cavity have a finite response time as describe previously. The optical response therefore can be decomposed in to a in-phase component which give rise to $\Delta\Omega$ and a quadrature component that give rise to $\Delta\Gamma$. In the scattering picture, when the laser is detuned from the cavity resonance, the photons can either absorb or emit a phonon creating two sidebands to the laser that are offset by the mechanical frequency Ω_m from the laser. The amplitude of the two sidebands are asymmetric due to the shape of the optical resonance resulting in the amplification or damping of the mechanical resonator.

2.3 Optical Readout of Mechanical Motion.

When an optomechanical resonator is interrogated at low optical powers, the optical force is small and does not significantly affect the mechanical oscilla-

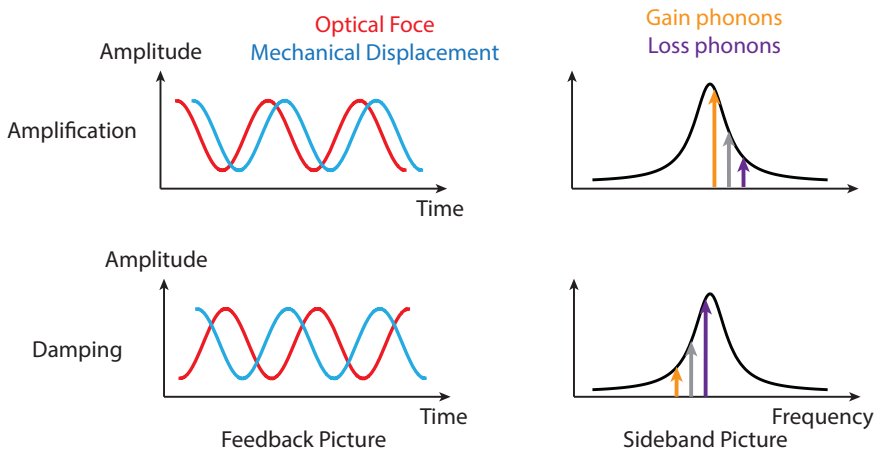

Figure 2.1: **Optomechanical gain and damping process.** The amplification and damping in the mechanical degree of freedom when the cavity is driven by a continuous wave laser can be understood using a feedback picture (left) or a scattering/sideband formalism (right). In the feedback picture, the delay between the optical and the mechanical response determines the sign of the effective change in the mechanical damping. In the sideband formalism, the cavity transmission creates asymmetry in the probability for the light to gain or loss phonon energies which effectively changes the damping.

tion. The light can therefore be used to readout the mechanical motion of the resonator. This can be visualized through a simple approximation of the optical transmission T where

$$T = |s + i\sqrt{\gamma_{\text{ext}}}a|^2 = s^2\left(1 - \frac{\gamma_{\text{ext}}}{(\Delta + g_{\text{om}}x)^2 - \left(\frac{\gamma}{2}\right)^2}\right) \tag{2.9}$$

For a small change of Δx the change in the optical transmission is approximately

$$\delta T \sim \frac{dT}{dx}\delta x = \frac{dT}{d\omega}\frac{d\omega}{dx}\Delta x = \frac{dT}{d\omega}g_{\mathrm{om}}\delta x \tag{2.10}$$

With a small displacement δx and $\Delta >> g_{\mathrm{om}}\delta x$

$$\frac{dT}{d\omega} = \frac{\Delta\gamma_{\mathrm{ext}}}{\left(\Delta^2 + \left(\frac{\gamma}{2}\right)^2\right)^2} \tag{2.11}$$

which is a constant for a given laser-cavity detuning Δ. Therefore at low optical power, the displacement of the mechanical resonator x is directly trasduced on to the optical transmission with a fixed gain. At the optimum laser-cavity detuning $\Delta = \gamma/2$, the optical trasduction is

$$\delta T = 2\eta g_{\mathrm{om}}\delta x \tag{2.12}$$

where $\eta = \gamma_{\mathrm{ext}}/\gamma$ is the ideality coupling factor describing the external optical coupling strength [9]. So we can see that for small amplitudes δx, the mechanical spectrum will be linearly imprinted onto the optical spectrum. This concept will be used through out the thesis.

2.4 Self-sustaining Optomechanical Oscillator

When the laser is blue detuned to amplify the mechanical motion, if it exceeds a certain threshold power to overcome the intrinsic mechanical damping ($\Gamma' \rightarrow 0$), the optomechanical resonator spontaneously starts oscillation and become a limit cycle oscillator, characterized by a sudden linewidth narrowing and amplitude growth of the mechanical power spectrum. The amplitude of the oscillation is limited by the nonlinearity in the optical transduction. The threshold power at which the oscillation occurs at the optimum laser-cavity detuning ($\Delta = \frac{\gamma}{2}$) can be obtained by setting $\Gamma' = 0$ in equation 2.8 which gives

$$P_{th} = \frac{\Omega_m m_{\text{eff}} \omega^4}{8\eta g_{\text{om}}^2 Q_m Q^3} \tag{2.13}$$

where $Q = \omega/\gamma$ is the optical quality factor, $Q_m = \Omega/\Gamma$ is the mechanical quality factor.

In chapter 4 and 5, we focus on the amplification and the limit cycle of optomechanical oscillators.

CHAPTER 3

HIGH QUALITY FACTOR OPTOMECHANICAL RESONATORS

3.1 Background

Optomechanical resonators have fostered record detection of ultra-weak forces [10], preparation of micromechanical oscillators close to their motional quantum ground states [11, 12], enabling self-sustaining mechanical oscillator dynamics [13, 14, 15], and optomechanical photodetection [16]. But like all micromechanical resonators, their performance suffers from the dissipation of mechanical energy. The dissipation of mechanical energy in such devices reduces their sensitivity, shortens their coherence time, increases their power consumption and degrades the phase noise performance [17, 18]. This mechanical dissipation is often dominated by anchor losses at the necessary supporting clamps [19, 20, 21], among other mechanisms responsible for the overall dissipation such as thermo-elastic damping [22], phonon scattering [20], and defect relaxations [23]. Recent efforts in reducing anchor losses in micromechanical devices include using spoke design [6, 21], phononic bandgaps [24, 25] and materials with high internal stress [26]. The spoke design creates an artificial bottleneck of energy flow at the cost of structural rigidity, whereas phononic bandgap materials are less suitable for lower frequency resonators as the size of the unit cell scales up and they occupy larger real estate.

3.2 A tuning fork analogue

Here we show that the structural loss of an optomechanical oscillator can be effectively eliminated through the destructive interference of elastic waves, by emulating the principle of a tuning fork resonator. A tuning fork resonator produces a long lasting sound when excited, as a result of its high mechanical quality factor. When a tuning fork vibrates, its two prongs oscillate 180 degrees out of phase. The elastic wave produced from each prong largely cancels out leading to no net motion therefore no loss at the base. Here, in order to create the tuning fork effect, we use double-disk optomechanical resonators [27, 28].

We emulate the tuning fork principle using a dual-disk resonator, consisting of a pair of thin silicon nitride (Si_3N_4) disks separated by a narrow gap (Fig. 3.1a,b). The thin SiO_2 sacrificial layer mechanically couples the top and bottom resonator, allowing the mechanical waves to interfere. This sub-wavelength gap also results in the evanescent coupling of the optical fields, creating coupled optical modes that span both the top and the bottom disks. The attractive optical forces efficiently excite the antisymmetric mechanical modes, illustrated in Fig. 3.1c,d as the freestanding edges moves in opposite directions. The symmetric mechanical mode is however much less sensitive to the optical excitation.

When the two freestanding edges are identical, the structural dissipation of the antisymmetric mechanical mode is minimized. The origin of the anchor loss in our structures is due to the displacement induced in the clamping area by the oscillation of each freestanding edge. Such displacement radiates elastic waves towards the pedestal and the substrate and therefore dissipates energy from the mechanical resonance (Fig. 1c,d). The antisymmetric mechanical mode excited

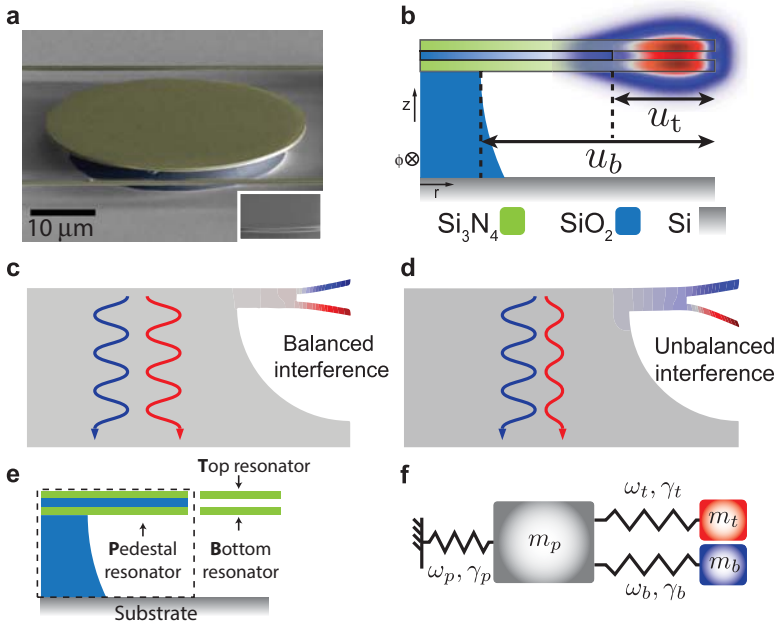

Figure 3.1: **Device schematic**. (**a**) Scanning electron micrograph of the fabricated device. The inset is a close-up of the freestanding double-disk edges. The two horizontal strings are for supporting tapered fibers. (**b**) Schematic of the cross section of the device, u_t and u_b are the undercut depth of the top and bottom layers, respectively. The false-color scale shows the transverse electric optical mode profile which spans the top and the bottom disks. (**c,d**) Finite-element model showing the impact of the thickness difference of the top and bottom cantilever, leading to an unbalanced interference of the elastic wave emitted by the moving edges. (**e, f**) A lumped theoretical model consists of three masses: m_t and m_b for the two edges and m_p for the pedestal, each with mechanical frequencies ω_t, ω_b, ω_p and damping rate γ_t, γ_b, γ_p

.

experiences much less structural loss than the symmetric mechanical mode due to the destructive interference between the elastic wave radiated from the top and the bottom disks.

3.3 Modelling the anchor loss

In order to gain a physical intuition of the dissipation process, the dual-disk mechanical mode structure could be dissembled into simpler building blocks, the two freestanding edges (resonators T and B) emulating a tuning fork and the pedestal (resonator P), as depicted in Fig. 3.1e. Since all the mechanical energy inside the pedestal leaks to the bulk substrate, the structural loss rate of the resonator can therefore be established as the mechanical coupling rate between the freestanding resonators and the pedestal resonators. The higher the coupling between the freestanding edges and the pedestal resonator the more energy dissipation there is through the pedestal.

The coupling strength of the freestanding edges to the pedestal is reflected in their dispersion curves as a function of the midlle SiO_2 layer thickness (t_m). In the case where there is no coupling, the mechanical frequencies of the edge modes would be independent of t_m, which is a parameter of the pedestal mode. Therefore the more sensitive the mode frequencies are to the SiO_2 layer thickness t_m, the stronger the coupling is to the pedestal. We numerically investigate the coupling strength between the freestanding edge and the pedestal resonators using a finite-element (FEM) solver (COMSOL) through varying the thickness t_m of the middle SiO_2 layer . As shown in Fig. 3.2a, the antisymmetric (blue curve) mechanical mode stiffens and the symmetric (red curve) edge

mode softens as t_m reduces. The rapid softening of the symmetric mechanical mode indicates a strong mechanical coupling to the pedestal mode. Whereas the antisymmetric mode displays an almost flat dispersion relation to t_m, indicating that the antisymmetric mode is insensitive to t_m of the pedestal resonator and therefore is weakly coupled to the pedestal mode. This is due to the cancelling of the elastic wave from the two counter oscillating edges.

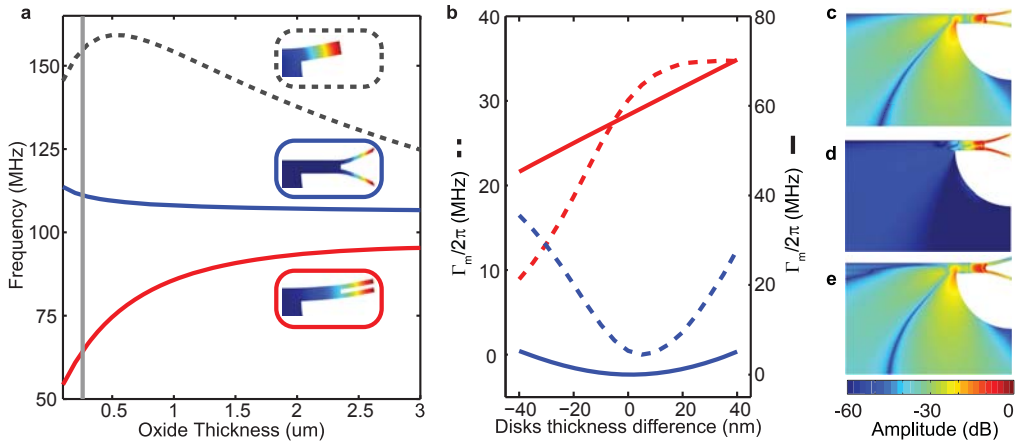

Figure 3.2: **Device Simulations**. (**a**) Dispersion of mechanical frequencies as function of middle SiO_2 thickness; grey-dashed: pedestal mode, solid-blue: antisymmetric (AS) mode, solid-red: symmetric (S) mode, vertical solid-grey shows position of 200 nm SiO_2 thickness. (**b**) Damping rate as function of top and bottom disks thicknesses difference for 3 μm (dashed, left scale) and 200 nm (solid, right scale) middle SiO_2 thickness, for the AS (blue) and S (red) modes. (**c-e**) $\hat{z}$ component of mechanical Poynting vector spatial distribution (false-color scale) for a top disk thicker $\delta t = 20$ nm (c), equal $\delta t = 0$ (e), and thinner $\delta t = -20$ nm (**f**) than the bottom one.

The vital role of the thickness difference in the freestanding edges can be visualized through the mechanical dissipation rate shown in Fig. 3.2b. Our numerical simulation of the structural loss rate as a function of the thickness difference between the two edges in Fig. 3.2b confirms that indeed the loss rate

is a minimum when the two disks are of equal thickness. Note that for a thick sacrificial layer (dashed curves) the minimum structural loss for the antisymmetric edge mode occurs when the top disk is slightly thicker. This is due to the symmetry breaking from the finite undercut radius of the bottom disk. Figs. 3.2c-e show the z-component of the mechanical energy flow (mechanical Poynting vector) for three top disk thickness differences when t_m = 200 nm. It is clear that the elastic wave radiation into the pedestal is drastically reduced when the two disks are of equal thickness.

3.4 Fabrication and experiment

We develop a pre-compensation technique to fabricate the freestanding edges of the double-disk structure and ensure that they are equal in thickness. We deposited a 240/200/220 nm Si_3N_4 /SiO_2 /Si_3N_4 film stack on a silicon wafer with 3 μm of thermal SiO_2 . The stoichiometric Si_3N_4 films are deposited via low pressure chemical vapor deposition technique and the SiO_2 layer is deposited via plasma-enhanced chemical vapor deposition and subsequently N_2 annealed at 1100 °C over 1 hour. The 20 nm difference in the thickness of the two Si_3N_4 layers is designed to pre-compensate the change in their relative thickness as a result of the releasing wet etching step. We pattern the wafer with e-beam lithography and transfer the pattern with reactive ion etching (CHF_3/O_2). The devices are then undercut in a buffered oxide etch (6:1). This wet etching process has a finite selectivity to Si_3N_4 and SiO_2 , roughly 1:100. Therefore it not only etches SiO_2 at 80 nm/min but also removes Si_3N_4 at a slower rate of 0.8 nm/min. As the top Si_3N_4 layer is more exposed, it etches slightly faster than the bottom Si_3N_4 layer. After the designed release time, the resulting structure

has two suspended Si_3N_4 layers with nearly identical thickness.

We experimentally demonstrate a high mechanical quality factor of 10^4 at 102.3 MHz, close to the material limited loss of Si_3N_4 at this frequency range [26]. This is more than a threefold improvement over previously demonstrated devices with uncompensated films whose typical measured mechanical quality factors are $Q_m = 2500$ [15]. We measure the mechanical quality factor of our devices by coupling a low power continuous wave laser to the devices through a tapered optical fiber, as show in the schematic of Fig. 3.3a. The devices are characterized inside a vacuum chamber (5-10 mTorr) at room temperature to minimize air damping. The mechanical spectrum can be observed through the optical transmission detected by a fast photodiode (Newport 1811A) which is connected to a radio-frequency spectrum analyzer. We test the optomechanical resonator by tuning the laser to an over-coupled optical resonance near 1530 nm with a loaded optical quality factor of 1.5×10^5. When the low power laser is slightly detuned from the cavity resonance, the thermal Brownian motion of the mechanical resonator is transduced to the optical signal as amplitude modulated radio-frequency (RF) signals. A typical RF spectrum of the detected photocurrent, which is proportional to thermal Brownian mechanical spectrum power density, is shown in Fig. 3.3c for an optimized cavity. The quality factor Q_m, is obtained from a Lorenztian fit through the relation $Q_m = \omega_m/\delta\omega_m$, where $\delta\omega_m = 2\gamma_m$ is the full width half maximum of the thermal Brownian peak and ω_m and γ_m are the mechanical frequency and damping rate. We used an input optical power of 6 μW, well below the estimated threshold power of regenerative oscillation of 180 μW. At this input power level, the optomechanical feedback [29] does not affect the measured Q_m significantly. This is ensured by optimally detuning the laser on both sides of the optical resonance and verify that the

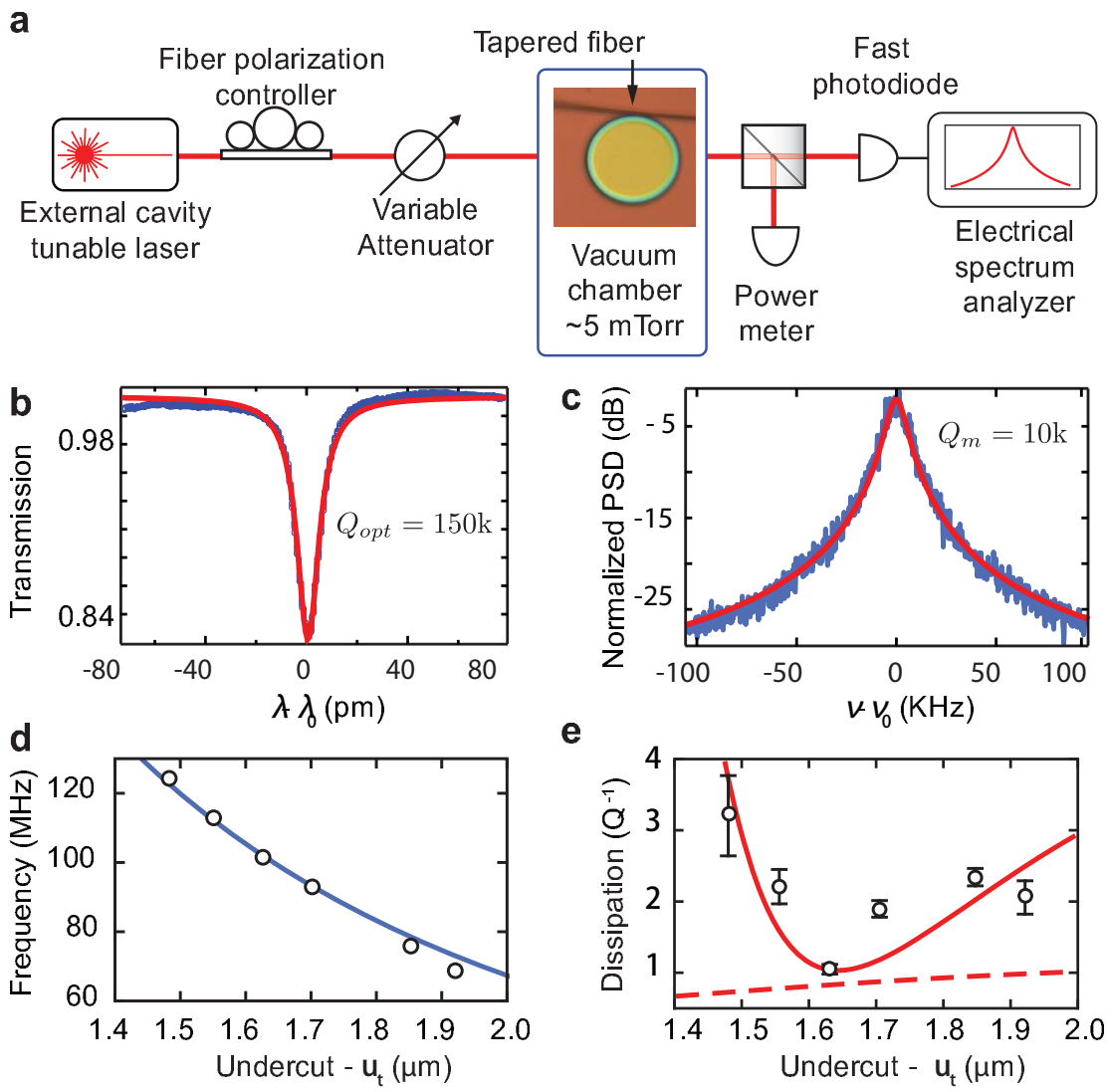

Figure 3.3: **Experimental results**.(**a**) Simplied schematic of the experimental setup. (**b**) Optical transmission showing a resonance centered at λ_0 =1530.6 nm with a loaded optical quality factor $Q_{\text{opt}} = 1.5 \times 10^5$. (**c**) Radio-frequency power spectral density of the transmitted optical signal. A typical AS mechanical mode resonant frequency centered at ν_0 = 102.3 MHz for the optimized thickness device showing a quality factor $Q_{\text{m}} = 10^4$. (d,e) Measured mechanical frequency (**d**) and dissipation (**e**) of the devices etched through different times. The solid curves are the fitted analytical model prediction, the dashed line is the thermoelastic damping contribution. The error bars in (e) are obtained from the standard deviation among five identical devices

difference between the blue and red-detuned Q-measurement is less than 1 percent. The measured mechanical frequencies (dissipation)) are shown as circles in Fig. 3.3d (Fig. 3.3e). The mechanical quality factors of the devices with precompensated layers have an average mechanical quality factor of $(8.0\pm0.8)\times10^3$.

3.5 Coupled mechanical resonator model

We show that the results from the numerical simulations and the experiment can be explained by a simple analytical lumped model of coupled resonators. We decompose the structure into the two freestanding edge resonators and the pedestal resonators as our qualitative analysis described previously. This analytical model agrees with the frequency dependence and the mechanical quality factors observed in both our numerical simulations and experimental results (Fig. 3.3d,e). In the analysis, we associate a mass-spring lumped model with each resonator identified in Fig. 3.1e. The resulting coupled system is illustrated in Fig. 3.1f. Note that when the masses move in opposite phase, there is no net motion of the pedestal and therefore the damping contribution from the pedestal damping γ_p is negligible. The normal modes of the coupled system are given by the eigenvectors of the matrix of the system:

$$M(\Omega) = \begin{pmatrix} i\Delta_p + \gamma_p & i\kappa/2 & i\kappa/2 \\ i\kappa/2 & i\Delta_t + \gamma_t & i\beta/2 \\ i\kappa/2 & i\beta/2 & i\Delta_b + \gamma_b \end{pmatrix}, \tag{3.1}$$

where $\Delta_{p,t,b} \equiv \Omega - \omega_{p,t,b}$ is the detuning of the sought eigenvalue (Ω) and the lumped resonators frequencies ($\omega_{p,t,b}$), κ is the coupling rate between the top and bottom resonators to the pedestal, and ω_p the pedestal frequency. β is

the coupling between the top and bottom resonators and $\gamma_{t,b,p}$ are the damping rate of the three oscillators We assume the frequency dependence of the freestanding edges (ω_t, b) on the undercut (u_t) and thickness (t_i) is given by a circular-plate analytical model, $\omega_i(t_i) = x t_i u_t^{-2} E^{1/2}[12\rho(1-\nu^2)]^{-1/2}$, where $(E, \rho, \nu) = (250\,\text{GPa}, 3100\,\text{kg/m}^3, 0.25)$ are respectively the Young modulus, density and the Poisson ratio for Si_3N_4 . The numerical factor $x \sim 1.4$ is comparable to the value obtained by solving the plate problem with a clamped-free boundary condition [30]. By solving the characteristic equation given by $\det[M(\Omega)] = 0$ we obtain a complex eigenvalue (Ω) whose real and imaginary parts correspond to the mechanical frequency and damping of the normal modes, respectively. The solid blue and red lines on Figs. 3d and 3e show the fitted model prediction for the mechanical frequency and dissipation $(Q^{-1} = 2\text{Im}[\Omega]/\text{Re}[\Omega])$, respectively. The bare frequenies $\omega_{p,t,b}(u_t)$ are calculated from the analytical circular-plate analytical model and is also used to calculated the bare damping rates $(\gamma_t, b = \omega_{p,t,b}/(2Q_{t,b}))$, with the bare quality factors $(Q_{t,b})$ inferred from FEM simulations. Since the model parameters impact very distinctively the real and imaginary parts of the complex eigenvalue, they were iteratively adjusted using both the measured frequencies (Fig. 3d) and damping rates (Fig. 3e). The fitted parameters are given by $(Q_p, \kappa, \beta, x) = (1.2; 110\text{Mhz}, 5.96\text{Mhz}, 1.36)$ for which their initial values are estimated also by FEM simulations. When the structural loss is eliminated, the dominant loss will be thermoelastic damping. We show in Fig. 3e, dashed-red line, the fundamentally limited dissipation based on thermoelastic damping prediction using the typical Si_3N_4 parameters $(c_p, \kappa_t, \alpha, T) = (710\,\text{JK}^{-1}; 3.2\,\text{Wm}^{-1}\text{K}^{-1}; 2\times10^{-6}\,\text{K}^{-1}, 300\,\text{K})$, representing respectively the specific heat, thermal conductivity, thermal expansion coefficient, and temperature [22, 26, 31, 32]. This shows that our demonstrated device is within

a factor of 1.3 of the material limited damping. Despite the simplicity of the model, the obtained fit parameters are in good agreement with values inferred from the FEM simulations.

3.6 Conclusion

Reducing the structural loss using destructive elastic wave interference is not only limited to double disk optomechanical oscillators. Using the same methodology, one could design for example an identical pair of loosely spaced singly or doubly clamped cantilevers. When they are excited in an anti-symmetric fashion, their support loss can be eliminated. Our method opens a path towards the deterministic design of micro- and nanomechanical resonators that are limited only by material losses.

CHAPTER 4

SYNCHRONIZATION OF TWO COUPLED OPTOMECHANICAL OSCILLATORS

4.1 Background

Christiaan Huygens in 17th century noticed that clocks hanging close to each other on the same wall often become synchronized, which he called an odd kind of sympathy [33]. He realized that the tiny motion of the wall caused by the swing of the pendulums is enough to induce synchronized motion between the two clocks. Later synchronization has found to be a universal phenomena. In nature, fireflies can flash synchronously possibly for better chances of mating. In human heart, regular beating occurs because of the synchronized oscillations of individual pacemaker cells. In fact, it is not uncommon that the pacemaker cells could oscillate asynchronously giving rise to a condition called arrhythmia. The circadian cycle is the synchronization of ones' biological metabolism to the external cycle of day and night [34]. Some neurons in the brain exhibit complex network dynamics including synchronization [35]. In the world of technology, synchronization is the basis for modern communication, navigation and signal processing. The electric grid also relies on synchronized generators to provide a stable and high power electrical source [36]. Synchronization could also enable novel computing and memory concepts [37, 38] such as pattern recognition [39].

Synchronization of a large network of nanoscale oscillators could revolutionize timing technologies. Synchronized oscillator arrays could enable high power, high accuracy and low cost frequency sources integrated in a pla-

narized process. For scientific interests, coupled oscillators arrays integrated on a chip could put many large complex networks exhibiting exotic nonlinear behaviours in practice [40, 41, 42, 43]. The major challenge with building a large network of coupled oscillators are non-configurable and short range coupling which limits the control, the size and the topologies of the oscillator networks [44, 45, 46, 47, 48]. Previously, synchronization between two micro- and nanoscale oscillators has been observed in MEMS and spin-torque systems. The two MEMS oscillators by Shim et al. [42] couple through a mechanical beam which limits how far away the oscillators can be placed.

We show in this chapter that we can synchronize two physically disconnected micromechanical oscillators through only an optical field. Recently, it is proposed that micromechanical oscillators can be coupled and synchronized through an optical field. This could form an all-to-all coupling that could overcome the neighbourhood restriction [45, 49]. Here we use two double-disk optomechanical oscillators (OMO) that we discussed in the previous chapter and couple them together with light. The two optically coupled OMOs [right (R) and left (L)] with different mechanical frequencies are placed close to each other but separated by a narrow gap of $\sim$ 400 nm which precludes any mechanical coupling. The optical coupling means the mechanical displacement of one OMO will lead to a force on the other OMO through the optical field. This force is responsible for the effective mechanical coupling between the two OMOs. As the OMOs are pumped by a blue-detuned CW laser into self-sustaining oscillations, the R (L) OMO not only experiences the oscillation at its natural frequency but also a modulated optical force at the L (R) OMO's mechanical frequency. As the coupling between the two oscillators is increased, each OMO is eventually forced to oscillate at an intermediate frequency between their natural frequen-

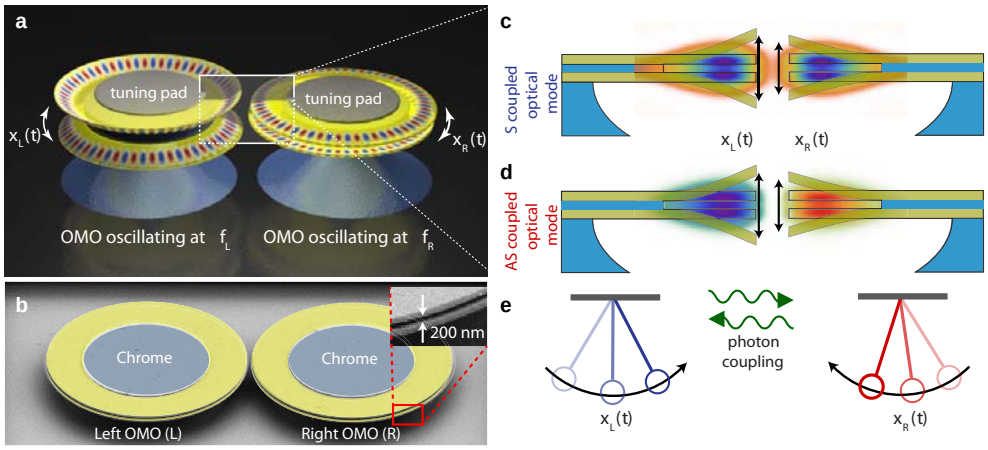

Figure 4.1: **Design of the optically coupled optomechanical oscillators (OMOs)**. (**a**) Schematic of the device illustrating the mechanical mode profile and the optical whispering gallery mode. (**b**) False-colored scanning electron micrograph (SEM) image of the OMOs with chrome heating pads (blue) for optical tuning by top illumination. (**c**,**d**) The symmetric (S) and anti-symmetric (AS) coupled optical supermodes. The deformation illustrates the mechanical mode that is excited by the optical field. (**e**) The dynamics of the coupled OMOs can be approximated by a lumped model for two optically coupled damped-driven nonlinear harmonic oscillators.

cies (Ω_R and Ω_L), that is, the onset of synchronization [50, 49, 51]. We also show that this optical coupling, as oppose to mechanical coupling can be turned on and off through thermal optical tuning. We observe both the individual free-running and synchronized oscillation dynamics by switching on and off the purely optical coupling between two OMOs. This work lays the foundation for building OMO arrays which is described in the next chapter and large scale OMO networks [52, 53, 54].

4.2 Device and fabrication

Our OMO consists of two suspended vertically stacked Si_3N_4 disks, where the optical and mechanical modes of such a cavity are localized around the OMO's free-standing edge (figure 7.1a,b) . The two disks are 40 μm in diameter and 200 nm in thickness, while the air gap between them is 190 nm wide. Such a small gap and the relative low refractive index of Si_3N_4 ($n \approx 2.0$) induce a strong optical coupling between the top and bottom disks. The resonant frequency of the optical modes of the stacked disks depend strongly on their separation [27]; therefore any mechanical vibration that modulates the vertical gap width also modulates the optical resonant frequency. The principle of the double-disk OMO is similar to that of a traditional Fabry-Perot optical cavity except that the moving mirror is replaced by the moving free-standing edge and the optical force is changed from radiation pressure to gradient force.

We fabricate the double-disk OMOs using standard lithography techniques. The double disk devices are patterned using electron-beam lithography followed by dry and wet etching steps. The two 210 nm thick stoichiometric Si_3N_4 films are deposited using low-pressure chemical vapour deposition (LPCVD). The 190 nm SiO_2 layer is deposited by plasma-enhanced chemical vapour deposition (PECVD). The underlying substrate is a 4 μm SiO_2 formed by thermal oxidation of a silicon wafer. The OMOs are defined by electron beam lithography which is then patterned by reactive ion etching. We also patterned heaters for thermo-optic tuning (detailed in sections below) which are subsequently defined by photolithography lift-off process. After defining the circular pads with lift-off resist, 200 nm of chrome is deposited on the device using electron beam evaporation and the residual chrome is lift-off afterwards. In order to release

the structure, the device is immersed in buffered hydrofluoric acid (6 : 1) for an isotropic etch of the SiO_2 in between the disks and the substrate layer. The device is then dried with a critical point dryer to avoid stiction between the two Si_3N_4 disks.

4.3 Coupled optical cavities

We describe in this section how the two double-disk OMOs are coupled optically. The two OMOs are separated by a distance of $d_g = (400 \pm 20)$ nm, minimizing direct mechanical coupling. This gap results in evanescent optical coupling between the OMOs when their optical resonant frequencies are close. The optical coupling leads to two optical supermodes spatially spanning both OMOs: a symmetric, lower frequency mode $b_+(t)$ (figure 7.1c) and an anti-symmetric higher frequency mode $b_-(t)$ (figure 7.1d). Their eigenfrequencies are given by $\omega_\pm = \bar{\omega} \pm \kappa/2$, where $\bar{\omega} = (\omega_L + \omega_R)/2$ and ω_L (ω_R) is the uncoupled optical resonant frequency of the L (R) OMO and κ is the optical coupling rate: a reflection of the distance between the two cavities. The optical supermodes can be analytically solved using coupled mode theory [8], assuming that the coupling is a weak perturbation to the individual cavity eigenmode ($\kappa << \omega_{FSR}$).

4.3.1 Coupled mode equations

The optical modes a_1 and a_2 of each optical cavity are coupled through the optical near-field. Due to scattering, there is also coupling between the clockwise (cw) and counter-clockwise (ccw) optical modes, therefore we need to consider

four optical modes, $a_1^{(cw,ccw)}$ and $a_2^{(cw,ccw)}$. The coupled equations satisfied by these modes are given by [8, 55] ,

$$\begin{pmatrix} \dot{a}_1^{cw} \\ \dot{a}_1^{ccw} \\ \dot{a}_2^{cw} \\ \dot{a}_2^{ccw} \end{pmatrix} = \begin{pmatrix} -\frac{\gamma_1}{2} - \mathrm{i}\omega_1 & \frac{\mathrm{i}\beta}{2} & \frac{\mathrm{i}\kappa}{2} & 0 \\ \frac{\mathrm{i}\beta}{2} & -\frac{\gamma_1}{2} - \mathrm{i}\omega_1 & 0 & \frac{\mathrm{i}\kappa}{2} \\ \frac{\mathrm{i}\kappa}{2} & 0 & -\frac{\gamma_2}{2} - \mathrm{i}\omega_2 & \frac{\mathrm{i}\beta}{2} \\ 0 & \frac{\mathrm{i}\kappa}{2} & \frac{\mathrm{i}\beta}{2} & -\frac{\gamma_2}{2} - \mathrm{i}\omega_2 \end{pmatrix} \begin{pmatrix} a_1^{cw} \\ a_1^{ccw} \\ a_2^{cw} \\ a_2^{ccw} \end{pmatrix} + \sqrt{\gamma_1 \eta_c} s_1(t) \begin{pmatrix} 1 \\ 0 \\ 0 \\ 0 \end{pmatrix} \tag{4.1}$$

where ω_m are optical resonance angular frequencies, γ_m is total damping rate, $\kappa/2$ is the inter-cavity optical coupling rate, $\eta_c = \gamma_e/(\gamma_{i_1} + \gamma_e)$ is the coupling ideality factor, γ_e is the external loss rate (due to the bus waveguide) and γ_i is the intrinsic damping rate [9].

The system of Eqs. (4.1) can be diagonalized exactly, each eigenvector is governed by an equation of the form

$$\dot{b}_{(m,\pm)} = \left[-\mathrm{i}\left(\bar{\omega} + (-1)^m \xi/2 \pm \beta/2\right) - \bar{\gamma}/2\right] b_{(m,\pm)} (\pm)^m \frac{\kappa \sqrt{\gamma_1 \eta_c} s_1(t)}{2\xi}, \text{ for } m = 1, 2, \tag{4.2}$$

where $\bar{\omega} = (\omega_1 + \omega_2)/2$, $\bar{\gamma} = (\gamma_1 + \gamma_2)/2$, $\xi = \kappa\sqrt{1 - (\delta/\kappa)^2}$ and $\delta = (\gamma_1 - \gamma_2)/2 + \mathrm{i}(\omega_2 - \omega_1)$. The original fields $a_{1,2}^{cw,ccw}$ can be recovered from the eigenvectors through the relation,

$$\begin{pmatrix} a_1^{cw} \\ a_1^{ccw} \\ a_2^{cw} \\ a_2^{ccw} \end{pmatrix} = \frac{1}{2\xi} \begin{pmatrix} -\kappa b_{(1,-)} + (\xi + i\delta) b_{(2,-)} \\ -\kappa b_{(1,+)} + (\xi + i\delta) b_{(2,+)} \\ \kappa b_{(1,-)} + (\xi - i\delta) b_{(2,-)} \\ \kappa b_{(1,+)} + (\xi - i\delta) b_{(2,+)} \end{pmatrix} \tag{4.3}$$

where $b_{(m,\pm)} = (a_m^{ccw} \pm a_m^{cw})$, Eq. (4.3) will be used to calculate the optical transmission function in the section 4.3.2 below.

4.3.2 Steady-state transmission

To obtain the low-power steady-state optical transmission spectrum, we assume that the laser driving term in Eq. (4.1) is oscillating at ω, i.e., $s_1(t) = s_1 e^{i\omega t}$. Eq. (4.2) can be written in a rotating frame $c_{(m,\pm)}(t) = \tilde{c}_{(m,\pm)}(t)e^{i\omega t}$. The resulting equations will be of the form,

$$\dot{\tilde{b}}_{(m,\pm)} = [i\Delta_{(m,\pm)} - \bar{\gamma}/2]\,\tilde{b}_{(m,\pm)}(\pm)^m \frac{\kappa s_1 \sqrt{\gamma_1 \eta_c}}{2\xi}, \text{ for } m = 1, 2, \tag{4.4}$$

where $\Delta_{(m,\pm)} = \omega - (\bar{\omega} + (-1)^m \xi/2 \pm \beta/2)$ is the laser-cavity frequency detuning for each of the optical supermodes. The steady-state solution to (4.4) is given by

$$\tilde{b}_{(m,\pm)} = (\mp)^m \frac{\kappa s_1 \sqrt{\gamma_1 \eta_c}}{2\xi\,[i\Delta_{(m,\pm)} - \bar{\gamma}/2]}, \text{ for } m = 1, 2. \tag{4.5}$$

The driving laser excites directly only the mode a_1^{cw}, therefore the steady state optical field transmitted through the bus waveguide is given by,

$$s_1^{out}(\omega_l) = s_1 - \sqrt{\gamma_1 \eta_c} a_1^{cw} \tag{4.6}$$

where the optical field $a_1(\omega_l)$ is given by Eq. (4.3). The normalized field transmission, $t(\omega) = s_1^{out}(\omega)/s_1$ is given by,

$$t = 1 - i\frac{\gamma_1 \eta_c \kappa}{2\xi^2} \sum_{j=1,2} \left(\frac{\xi + i\alpha\kappa}{(-1)^j \beta + \xi + 2\bar{\Delta} + i\bar{\gamma}} + \frac{(-1)^j \kappa}{(-1)^j \beta - \xi + 2\bar{\Delta} + i\bar{\gamma}} \right), \tag{4.7}$$

where $\bar{\Delta} = \omega_l - \bar{\omega}$ is the detuning from the average frequency of the two cavities. The normalized power transmission is obtained from the relation $T(\omega) = |t(\omega)|^2$.

We measure the optical transmission of the coupled cavity system using a tapered optical fiber as shown in figure 4.2. The tapered optical fiber is positioned

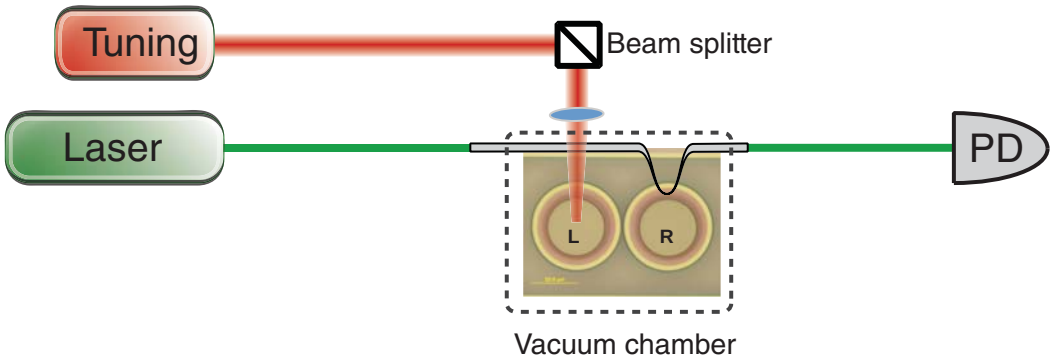

Figure 4.2: **Measuring the optical transmission**. Schematic of the experimental setup for characterizing the optical transmission of the coupled cavity system with tuning using external laser heating. PD: photodiode.

in the proximity of one of the OMOs and excites the coupled optical supermodes through optical evanescent coupling. We sweep the laser wavelength to obtain the transmission spectrum as shown in figure 4.3. The optical mode we work with is a high Q mode highlighted in green in figure 4.3a. A closer look of this mode (Fig. 4.3b) reveals the split supermodes that results from the coupling between the two disks and the cw and ccw directions. In figure 4.3c, we show the transmission $T(\omega)$ using the best-fit parameters $\bar{\omega}/(2\pi) = 188.442$ THz, $\bar{\gamma}/2\pi = 299$ MHz, $(\kappa,\beta)/2\pi = (1700, 298)$ MHz, and $\eta_c = 0.65$. The fit loaded optical quality factor is $Q = \bar{\omega}/\bar{\gamma} = 630,000$.

4.3.3 Top illumination thermal tuning

We integrate Chrome heaters on top of each cavity so that the system can be reconfigured to exhibit either coupled or single OMO dynamics by control-

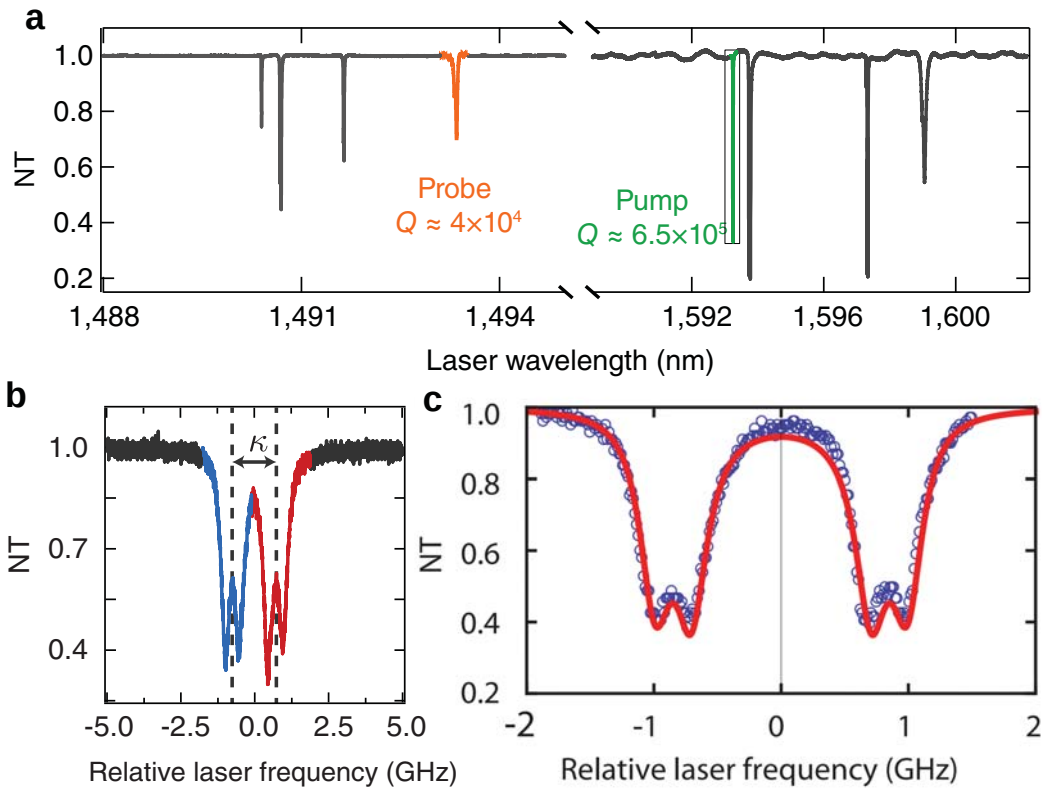

Figure 4.3: **Optical transmission**. (**a**) Transmission spectrum of the coupled disks. The two colored resonances represents the two optical modes we work with in the experiment, one for driving the system and one for probing the system. (**b**). S (blue) and AS (red) optical supermodes with optical coupling rate . NT: normalized transmission.(**c**) Best-fit steady-state normalized optical transmission (red-line), calculated using equation (4.7), and measured transmission spectrum (blue circles). The fit parameters are described in the text.

ling the optical mode coupling between the two oscillators. While the distance between the two OMOs is fixed (i.e. fixed κ), their optical coupling can be turned off (on) through increasing (decreasing) the optical frequency mismatch $\delta = \omega_R - \omega_L$ between them. For large optical frequency mismatch among the two OMOs ($\delta \gg \kappa$) the supermodes reduce to the uncoupled optical modes of the individual OMO, $(b_+, b_-) \rightarrow (a_L, a_R)$. This can be readily seen from the expression of the optical supermodes amplitudes, which are given by linear combinations of the uncoupled modes of the left $a_L(t)$ and right $a_R(t)$ cavities: $b_\pm(t) = a_L(t) - a_R(t)\mathrm{i}\kappa/(\delta \mp (\delta^2 - \kappa^2)^{1/2})$. We tune δ experimentally using thermo-optic effect, for which the optical frequency dependence on temperature can be approximated as $\omega_j(T_j) = \omega_0^{(j)} - g_{\mathrm{th}} T_j$ for $j = L, R$, where $\omega_0^{(j)}$ is the intrinsic optical frequency and g_{th} is the thermal-optic tuning efficiency. The optical coupling can therefore be continuously tuned through changing the relative temperature of the two OMOs: at $\Delta T = 0$ the OMOs have identical optical resonant frequencies and the optical coupling is maximized, manifested by the almost symmetric resonance dips in the optical transmission spectrum (figure 4.3b,c). Whereas for $\Delta T = \pm 25K$, the relative frequency difference is large ($\delta \gg \kappa$) and the optical mode does not couple the two OMOs. The OMOs follow the usual single-cavity optomechanical dynamics [56].

The thermo-optic tuning is accomplished by heating each individual disk from top-illumination. We choose to use 200 nm thick chrome pads as the heating element since they absorb 25% of 1550 nm light at normal incidence, taking into account its reflectivity. Chrome is also resistant to buffered oxide etch which follows in the fabrication steps. The heating light source is provided by a near-IR laser (JDS SWS16101), operating at 1550 nm, and amplified by a high power EDFA (Keopsys KPS-CUS-BT-C-35-PB-111-FA-FA) that can provide

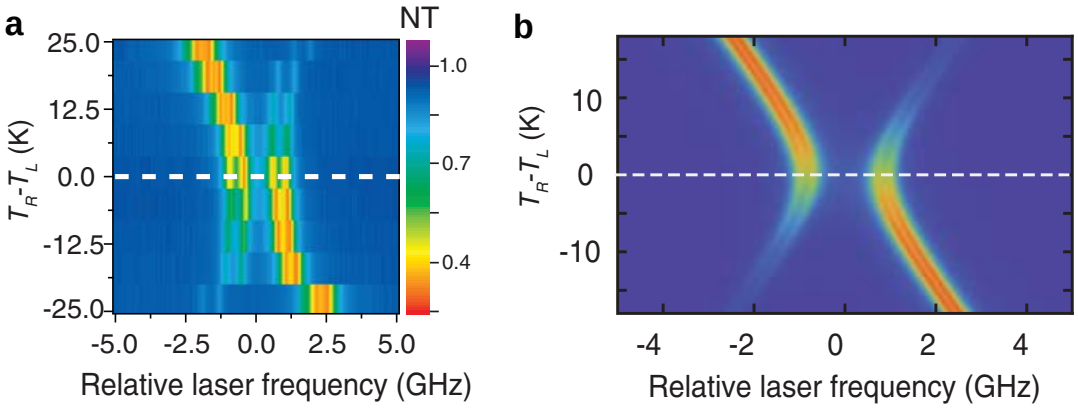

Figure 4.4: **Thermal-Optical tuning of the coupling**. (**a**) Measured thermal optical tuning of the coupled cavities as a function of the cavity temperature difference between the two cavities. Negative values are achieved by switching the cavity being heated by the laser. The color scale indicate transmission. (**b**) Theoretical optical transmission showing the thermal tuning of the coupled cavities, the false-color scale indicates the transmission. This map is obtained from (4.7) using $\omega_1(T) = \omega_{1_0} + g_{th}\Delta T$, in good agreement with the experimental data.

a maximum power of 2 W. The light is sent to the microscope optics which focus the light on to the device. Typically during an experiment, 50 mW of laser power incident on the device is needed to achieve the desired tuning range. The heat absorbed by the chrome pads induces a temperature change $\Delta T = R_{th}P_{abs}$, where $R_{th} = \partial\Delta T/\partial P_{abs} \approx 5.2 \times 10^3$ K/W is the simulated effective thermal resistance of our device. Due to thermo-optic effect, the temperature frequency shift rate is given by the perturbation expression,

$$g_{th} = \frac{\partial\omega_T}{\partial\Delta T} = -\frac{\omega_0}{2n_g}\frac{\int \alpha(r,z)T_{rel}(r,z)|\boldsymbol{E}|^2 dV}{\int |\boldsymbol{E}|^2 dV} \tag{4.8}$$

where $0 < T_{rel}(r,z) < 1$ is the dimensionless relative temperature distribution of the device, α is the material-dependent thermo-optic coefficient, and n_g is the optical mode group index. If we define the overlap integral $\Gamma = \int_{SiN} |\boldsymbol{E}|^2 / \int_{all} \boldsymbol{E}|^2$,

Eq. (4.8) is approximately given by $g_{th} \approx -(T_{rel}^{(\mathrm{SiN})})\omega_0 \alpha_{\mathrm{SiN}} \Gamma/(2n_g)$. In Fig. 4.5 we show the simulated relative temperature field $T_{rel}(r,z)$, at the edge of the disk $T_{rel} = T_{rel}^{(\mathrm{SiN})} \approx 0.83$. From these results we can estimate the top illumination laser power needed to tune the cavity's optical frequency by $\Delta\omega_T$,

$$P_{abs} = \frac{\Delta\omega_T}{g_{th} R_{th}} \approx \frac{2n_g}{R_{th}(T_{rel}^{(\mathrm{SiN})})\alpha_{\mathrm{SiN}}\Gamma}\left(\frac{\Delta\omega_T}{\omega_0}\right) \tag{4.9}$$

For our device, tuning of $\delta\lambda \approx 0.2$ nm is sufficient to completely decouple the two cavity modes. Using $n_g \approx 1.8$, $\alpha_{\mathrm{SiN}} = 3 \times 10^{-5}\ \mathrm{K}^{-1}$, and $\Gamma \approx 0.59$, Eq. (4.9) gives a tuning efficiency $g_{th}/2\pi \approx -256$ MHz/K, therefore a laser power of $P = P_{abs}/25\% \approx 24$ mW is needed to control the optical coupling between the cavities (see section 4.3.2).This value is in reasonable agreement with the experimental power range.

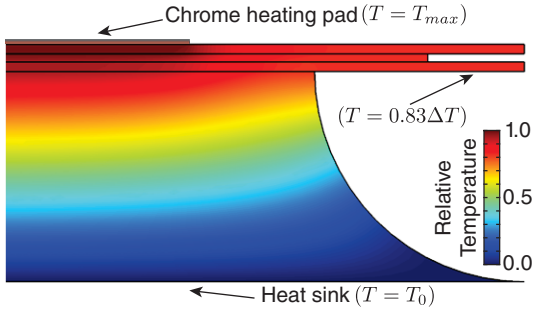

Figure 4.5: **Laser heating of a double-disk cavity**. Simulated temperature ($\Delta T = T - T_0$) profile of the optical micro cavity. The bottom boundary act as a heat reservoir with constant temperature $T_0 = 300$ K. In the mirroring edge, where the optical modes are localized, the temperature is $T \approx 0.83\Delta T$

4.4 Coupled Optomechanical Oscillators and Experimental Characterization

In this section, we discuss how the mechanics is coupled through the optical coupling describe in the previous section. We further show our experimental result on synchronization which is due to this effective mechanical coupling.

4.4.1 Mechanical equations and optomechanical Coupling

The mechanical degrees of freedom of each cavity x_1, x_2 follows the usual optomechanical equations [57, 58, 56, 59],

$$\ddot{x}_1 = -\Gamma_1 \dot{x}_1 - \Omega_1^2 x_1 + \frac{g_{om}}{m_{eff}^{(1)} \omega_0} \left(\left| a_1^{cw} \right|^2 + \left| a_2^{ccw} \right|^2 \right) + F_1^T(t), \tag{4.10a}$$

$$\ddot{x}_2 = -\Gamma_2 \dot{x}_2 - \Omega_2^2 x_2 + \frac{g_{om}}{m_{eff}^{(2)} \omega_0} \left(\left| a_1^{cw} \right|^2 + \left| a_2^{ccw} \right|^2 \right) + F_2^T(t), \tag{4.10b}$$

where $\Omega_i, \Gamma_i, m_{eff}^{(i)}$ represent the mechanical resonant frequency, dissipation rate, and effective motional mass. $F_T(t)$ is the thermal Langevin random force with expectation value $\left\langle F_i^T \right\rangle = 0$ and correlation function $\left\langle F_i^T(t) F_i^T(t+\tau) \right\rangle = 2k_B T m_{eff}^{(i)} \Gamma_i \delta(\tau)$, where k_B is the Boltzmann constant and $\delta(\tau)$ is the Dirac delta function. In contrast to the phonon-laser regime [60], we ignore terms which couples, through the mechanical displacement field, the optical modes $b_{(\pm,1)}$ with $b_{(\pm,2)}$; this is justified because $\kappa \gg \Omega_{L,R}$. Here we used the optical force as the positive gradient of the energy, this is a convention but must be consistent with whether the cavity frequency increases or decreases with increasing mechanical displacement; in our case the optical frequency decreases with the mechanical displacement [58]

The full optomechanical dynamics is obtained by solving simultaneously Eqs. (4.10) and (4.1), such dynamics is discussed in detail in section 4.5. It is however instructive to analyze how a prescribed mechanical motion of the two mechanical oscillators is read-out through the optical modes (see section 4.4.2), also how the optical force term in Eqs. (4.10) couples to the two of them. –

4.4.2 Optical transduction of mechanical oscillations

To account for the mechanical effect on the optical transmission we first assume that the mechanical motion is independent of the optical fields [46], which is equivalent to ignoring the dynamical back-action. Therefore we can use Eqs. (4.2) for the optical eigenvectors and simply replace the optical cavity's resonant frequency by $\omega_i \rightarrow \omega_i + g_{om}x_i$, where x_i is the mechanical displacement amplitude for each cavity. The resonant frequency of each eigenmode $b_{(m,\pm)}$ will be given by,

$$\omega_{(1,\pm)}(x_i, x_j) = \bar{\omega}(x_i, x_j) \pm \xi(x_i, x_j)/2 \pm \beta/2, \tag{4.11a}$$

$$\omega_{(2,\pm)}(x_i, x_j) = \bar{\omega}(x_i, x_j) \pm \xi(x_i, x_j)/2 \pm \beta/2, \tag{4.11b}$$

where $\bar{\omega}(x_i, x_j) = \left[\omega_i(x_i) + \omega_j(x_j)\right]/2$, $\xi(x_i, x_j) = \kappa\sqrt{(1 - [\delta(x_i, x_j)/\kappa]^2}$ and $\delta(x_i, x_j) = (\gamma_i - \gamma_j)/2 + [\omega_j(x_j) - \omega_i(x_i)]$. Due to the nonlinear $\xi(x_i, x_j)$ dependence on the mechanical displacement amplitudes $x_{1,2}$, the usual analytical approach to derive the optomechanical transduction coefficient does not apply [46]. However we can get insight into the problem if we consider the strong optical coupling limit, i.e., $\delta(x_i, x_j)/\kappa = g_{om}(x_i - x_j)/\kappa \ll 1$ which means that the optical frequency splitting between the cavities is large compared to the mechanically induced frequency shift, therefore $\xi(x_i, x_j) \approx \kappa + O(\delta^2/\kappa^2)$. To further simplify the anal-

ysis we assume that the two cavities share identical optical optical properties, i.e., $\omega_1(x_1 = 0) = \omega_2(x_2 = 0) = \omega_0$ and $\gamma_1 = \gamma_2 = \gamma_0$. In this case Eq. (4.11) is approximated by,

$$\omega_{(m,\pm)}(x_1, x_2) \approx \omega_{0(m,\pm)} + g_{om}\,(x_1 + x_2) \tag{4.12}$$

where $\omega_{0(m,\pm)} = \omega_0 + (-1)^{m+1}\kappa/2 \pm \beta/2$. Combined with the above relations, Eq. 4.2 yields the following equation for the optical eigenmodes $b_{(m,\pm)}$,

$$\dot{b}_{(m,\pm)} = \left[-\mathrm{i}\omega_{0(m,\pm)} - \mathrm{i}g_{om}(x_1 + x_2) - \bar{\gamma}/2\right] b_{(m,\pm)}(\pm)^m \frac{\sqrt{\gamma_1\eta_{c1}}\,s_1 e^{\mathrm{i}\omega t}}{2}, \text{ for i=1,2.} \tag{4.13}$$

The equations above (4.13) can be formally integrated for a prescribed mechanical motion ($x_i = A_i \sin(\Omega_i t + \phi_i)$). The homogeneous solutions ($s_1 = 0$) decay exponentially and does not contribute after the initial transients. To find a particular solution satisfying (4.13) we employ a common approach relying on the Jacobi-Anger expansion [46, 49],

$$\exp\left[\mathrm{i}\mu_1 \cos(\Omega_1 t + \phi_1) + \mathrm{i}\mu_2 \cos(\Omega_2 t + \phi_2)\right] = \sum_{p,q=-\infty}^{\infty} i^{p+q} J_p(\mu_1) J_q(\mu_2) e^{\mathrm{i}(p\Omega_1 + q\Omega_2)t + \mathrm{i}(\phi_1 + \phi_2)}, \tag{4.14}$$

where $\mu_i = g_{om}A_i/\Omega_i$ is the optomechanical modulation depth. Inserting Eq. (4.14) in (4.13) and solving the resulting equations gives,

$$b_{(m,\pm)}(t) = \frac{(\pm)^m s_1 \sqrt{\gamma_1\eta_{c1}}}{2} e^{\mathrm{i}\left[\omega_l t + \sum_{j=1,2}\mu_j \cos(\Omega_j t + \phi_j)\right]} \sum_{p,q} \frac{i^{p+q} J_p\,(\mu_1)\, J_q\,(\mu_2)\, e^{\mathrm{i}(p\Omega_1 + q\Omega_2)t}}{\bar{\gamma}/2 + i\,(-\Delta_{0(m,\pm)} + p\Omega_1 + q\Omega_2)}, \tag{4.15}$$

where the sum over m, n extends over $[-\infty, \infty]$, and $\Delta_{0(m,\pm)} = \omega_l - \omega_{0(m,\pm)}$. From Eq. (4.15) we can clearly see the that cavity field exhibit tones at combinations of the mechanical frequencies ($m\Omega_1 + n\Omega_2$) of the two cavities.

4.4.3 Intrinsic Optical and Mechanical Parameters

We measure the optomechanical transduction of the coupled OMOs using the setup shown in figure 4.6. As we discussed in the previous chapter, the mechanical vibration of the OMO is printed on the optical transmission which can be analyzed with a radio-frequency spectrum analyzer (RSA). The detailed setup for measuring the mechanical degree of freedom of the system is shown in figure 4.6. The green (red) line indicates the pump (probe) laser path. The pump laser drive the system while the weak probe laser could measure the system without inducing significant perturbations. Both the pump and the probe laser are fibre-coupled, tunable, near-infra (IR) lasers (Tunics Reference and Ando AQ4321D). Their optical power is controlled using independent variable optical attenuators. The pump and probe light are individually sent to a polarization controller and combined with a $50:50$ directional fiber coupler. A fraction of the power is monitored by a power meter which indicates the equivalent input optical power to the system. To prevent the back scattered light from entering the laser, an optical isolator is used before feeding the laser into a vacuum probe station (Lakeshore TTPX) operating at a pressure of 10^{-5} mT. The light is evanescent coupled to the OMOs through a tapered optical fiber waveguide by using a micro positioning system.

A small portion of the transmitted light (10%) is also monitored by a power meter. The remaining transmitted light is split with a wavelength division multiplexing coupler to separate the pump and the probe laser. Since the pump power used is low, especially for sub-threshold measurements, the pump light is optionally amplified with a low noise erbium pre-amplifier (EDFA, Amonics AEDFA-PL-30) before coupling to a 125 MHz bandwidth photodiode (New Fo-

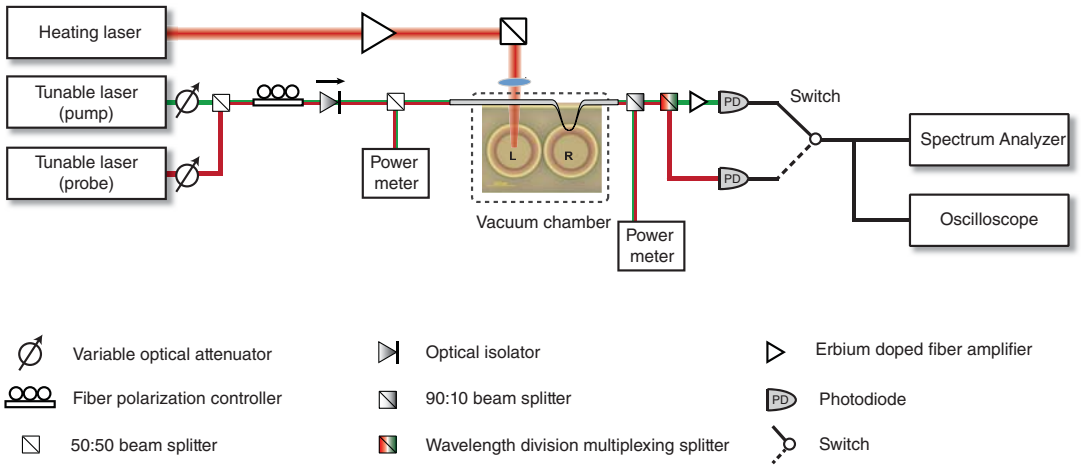

Figure 4.6: **Detailed experimental setup.**

cus 1181). An additional detector (Thorlabs PDB150C-AC) can be switched on when the probe measurement is necessary. Half of the detected signal is sent to an oscilloscope and the remaining is coupled to a radio-frequency spectrum analyser (RSA, Agilent E4407B).

We measured the mechanical quality factors of the two coupled OMOs using a low power laser coupled to the lower frequency optical supermodel (right peak in Fig. 4.3a). The excited optical supermodes spatially span both cavities therefore picking up the mechanical oscillation of both OMOs. The RF spectrum (100 averages) showing the two mechanical modes is shown in Fig. 4.7 from which we can extract the mechanical properties of each OMO. The fit parameters are the mechanical frequencies and quality factors: $(f_L, f_R) = (50.283, 50.219)$ MHz and $(Q_{m_L}, Q_{m_R}) = (3.4 \pm 0.3, 2.3 \pm 0.2) \times 10^3$.

A measure for the efficiency of the optomechanical interaction is the optomechanical coupling constant, defined as $g_{\text{om}} = \partial\omega/\partial x$ where ω is the optical fre-

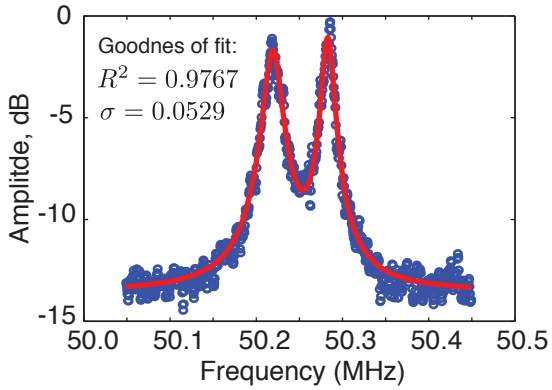

Figure 4.7: **Mechanical modes RF spectrum.** Double-Lorentzian best-fit steady-state normalized RF spectrum (red-line), and measured RF spectrum (blue circles). The fit parameters are described in the text.

quency and x is the mechanical mode amplitude [56, 61, 27]. Our device exhibits a large optomechanical coupling rate, calculated to be $g_{\mathrm{om}}/2\pi = 49$ GHz/nm (detailed below). The mechanical mode that couples most strongly to the optical field is also illustrated by the deformation of the disks edge in figures 7.1 which has a natural frequency of $\Omega_m/2\pi \approx 50.5$ MHz. Note that the two cavities are not identical and without the optical coupling they oscillate at different mechanical frequencies.

To obtain the optical and mechanical modes of the optomechanical disk cavity we rely on finite element simulations using COMSOL®. From these numerical simulations we derive parameters for the lumped model that describes the optomechanical dynamics, such as the effective motional mass m_{eff}, and the optomechanical coupling rate g_{om}. The optical modes are sought by solving the Helmholtz vector wave equation with an ansatz $\boldsymbol{E}(r,z,\phi) = \boldsymbol{E}(r,z)\exp(im\phi)$. In the table 4.1 we show the mode radial electric field profile for the lowest order optical transverse-electric (TE) modes. The mechanical displacement field is

sought by enforcing complete cylindrical symmetry, $\boldsymbol{u}(r,\phi,z) = \boldsymbol{u}(r,z)$, the mode profiles are also shown on table 4.1. From the sought eigenmodes, the optomechanical coupling coefficients for the supported optical modes are calculated using boundary perturbation theory [62, 63],

$$g_{om} \equiv \frac{\partial\omega}{\partial x} = \frac{\omega_0}{2}\frac{\int (\boldsymbol{U}\cdot\hat{n})\left(\Delta\epsilon_{12}\left|\boldsymbol{E}\cdot\hat{t}\right|^2 + \Delta\epsilon_{12}^{-1}\left|\boldsymbol{D}\cdot\hat{n}\right|^2\right)dA}{\int \epsilon\left|\boldsymbol{E}\right|^2 dV}, \tag{4.16}$$

where the dimensionless displacement field is defined as $\boldsymbol{U} \equiv \boldsymbol{u}/\max|\boldsymbol{u}|$, the relative permitivity differences are given by $\Delta\epsilon_{12} = \epsilon_1 - \epsilon_2$ and $\Delta\epsilon_{12}^{-1} = 1/\epsilon_1 - 1/\epsilon_2$, the unit vectors $\hat{t}$ and $\hat{n}$ indicate the tangential and normal components of the vectors. The effetive motional mass is calculated as,

$$m_{eff} = \int \rho\left|\boldsymbol{U}\right|^2 dV. \tag{4.17}$$

4.4.4 Single Cavity Measurements

We characterize the individual dynamics of the two OMOs by switching their optical coupling off ($T = \pm 25K$, figure 4.4b). Each cavity is individually excited with a continuous-wave laser through a tapered optical fibre. When one OMO is tested, the remaining one is heated by the heating laser with high power ($\sim$ 50 mW) to ensure that they are completely decoupled. As the laser frequency is tuned (from a higher to a lower frequency) into the optical resonance, the transmitted laser signal is detected by a photodiode (PD) and analyzed using a RF spectrum analyser (RSA). The RF spectral maps are obtained by detuning the laser from blue to red into the optical resonance in a stepwise fashion, as controlled by a voltage applied to laser's external cavity piezo; the laser used has a tuning coefficient of 1.1 GHz/volt. For each voltage step, the RF spectrum

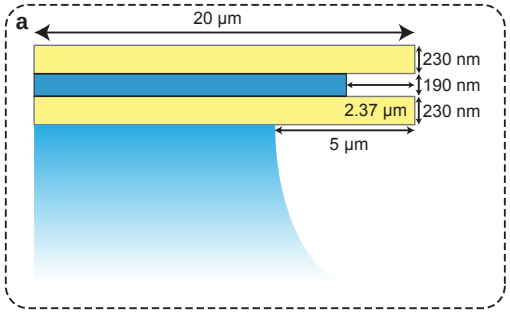

Mechanical mode	$\frac{\Omega_m}{2\pi}$ (MHz)	m_{eff} (pg)
	50.5	110
	28.7	194

Profile ($\lvert \boldsymbol{E} \cdot \hat{r} \rvert$)	Mode TE^n_m	λ_0 (nm)	$g_{om}/2\pi$(GHz/nm)
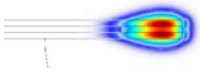	TE^1_{115}	1582.28	49.4
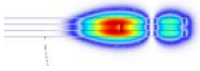	TE^2_{110}	1584.87	11.3
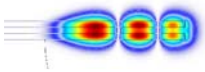	TE^3_{106}	1582.31	17.9
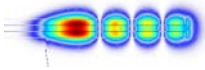	TE^4_{101}	1591.01	10.6

Table 4.1: **Optical and mechanical modes parameters.** (**a**) Geometry of the optomechanical cavity used to calculate the modes and parameters shown in the tables. For the optical modes profiles, it is shown the modulus of the radial electric field $|\boldsymbol{E} \cdot \hat{r}|$; g_{om} is calculated using Eq. (4.16). whereas for the mechanical modes it is shown the displacement amplitude $|\boldsymbol{u}|$ as colors and the deformation represents the normalized displacement.

is recorded. Therefore, the step size determines the vertical resolution of the RF spectra map whereas the resolution bandwidth of the RSA determines the horizontal resolution. Here we used a detuning step size of 3 MHz and a resolution bandwidth of 1 kHz (100 Hz video bandwidth). This allows us to obtain a high resolution map while keeping the data collection time reasonable ($\approx$ 20

minutes). The RF spectra show the mechanical modes have natural mechanical frequencies of $(f_L, f_R) = (\Omega_L, \Omega_R)/2\pi = (50.283, 50.219)$ MHz, and intrinsic quality factors of $(Q_m^{(L)}, Q_m^{(R)}) = (3.4 \pm 0.3, 2.3 \pm 0.2) \times 10^3$ (figure 4.8a,b). Note that these intrinsic frequencies are slightly lower than the OMO self-sustaining oscillation frequency. This is due to the optical spring effect as described in chapter 2. Due to the increased optomechanical back-action and intracavity optical power the OMOs have their frequencies increased and amplitudes grown as the laser is tuned into the optical resonance. Above a specific laser-cavity detuning, indicated by the horizontal white dashed lines on figure 4.8a,b the intrinsic mechanical losses are completely suppressed by the optomechanical amplification. At this point the optomechanical resonator starts self-sustaining oscillations and becomes an OMO characterized by sudden linewidth narrowing and oscillation amplitude growth [45, 46, 49]. It is clear from figure 4.8a,b that each cavity has only one mechanical mode in the frequency range of interest. Due to the slight difference in geometry, these frequencies differ by $\Delta f = f_L - f_R = (70.0 \pm 0.5)$ kHz.

4.4.5 Coupled Cavity Measurements

The mechanical modes of each cavity can be approximated by a lumped model consisting of two damped harmonic oscillators, which are driven by the nonlinear optical supermode forces,

$$\ddot{x}_j + \Gamma_j \dot{x}_j + \Omega_j^2 x_i = F_{\text{opt}}^{(j)}(x_R, x_L)/m_{\text{eff}}^{(j)}, \text{for } j,k = L,R$$

where $x_j, \Omega_j, \Gamma_j, m_{\text{eff}}^{(j)}$ represent the mechanical displacement, mechanical resonant frequency, dissipation rate, and effective motional mass of each mechanical degree of freedom. The optical force is proportional to the optical energy stored in the coupled optical modes, which depend both on x_R and x_L,

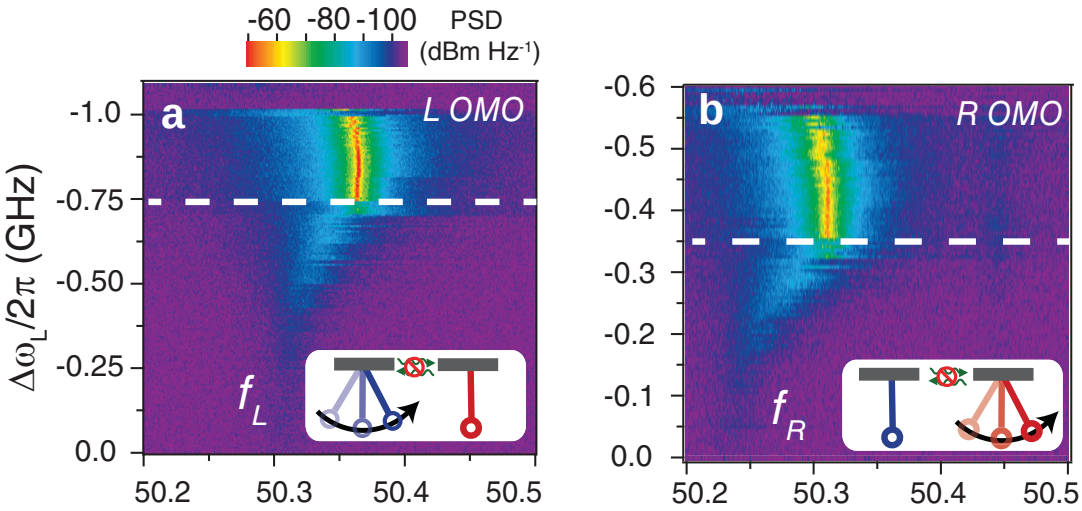

Figure 4.8: **RF spectra of the OMOs** (**a**, **b**) RF power spectra of cavity L (a) and R (b) as a function of laser frequency when the coupling is turned off. The horizontal white lines indicate the onset of self-sustaining oscillation. PSD: power spectral density.

i.e. $F^{(j)}_{\text{opt}}(x_R, x_L) \propto |b_{\pm}(x_R, x_L)|^2$. Therefore the optical field not only drives but also mechanically couples each OMO. The nonlinear nature of this driving and coupling force form the basis for the onset of synchronization. In a first order linear approximation when the two OMOs are evenly coupled ($\omega_L = \omega_R$), the effective mechanical coupling force between the two oscillators is given by $F^{(i)}_{\text{coup}} = -k_I x_j + k_Q \dot{x}_j$ where k_I and k_Q are the position and velocity coupling coefficients (see subsection 4.6.2). In the unresolved side band limit (optical damping rate $\gamma \ll \Omega_j$), these coupling coefficients are determined by both the input optical power P_{in} and laser-cavity detuning Δ as $k_I \propto P_{\text{in}}\Delta((\gamma/2)^2 + \Delta^2)^{-2}$ and $k_Q \propto P_{\text{in}}(\gamma/2)\Delta((\gamma/2)^2 + \Delta^2)^{-3}$. Therefore, by varying Δ and P_{in}, hence the effective mechanical coupling strength, synchronization of the two OMOs can be captured.

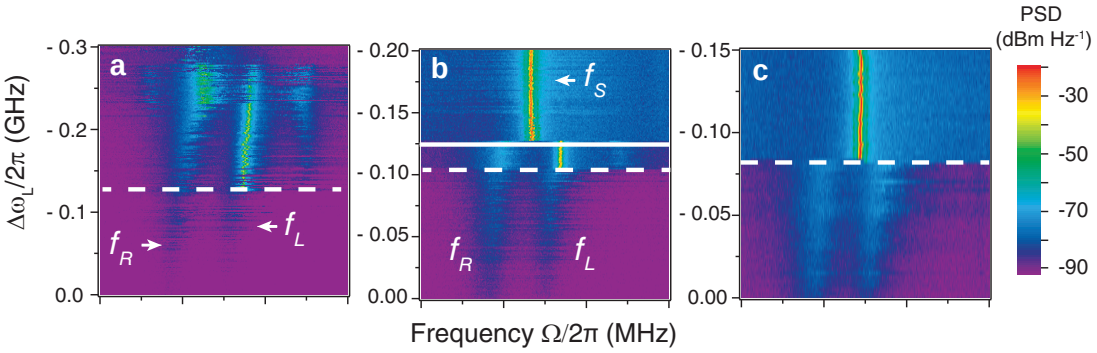

Figure 4.9: **RF spectra of the OMOs and synchronization** (**a**) When the coupling is turned on, at an input power $P_{in} = (1.8 \pm 0.2)$ μW cavities L and R do not synchronize and oscillate close to their natural frequencies. (**b**) At $P_{in} = (11 \pm 1)$ μW synchronization occurs after the horizontal solid white line after a brief region of unsynchronized oscillation (between the dashed and solid white lines). (**c**) The system oscillate directly in a synchronized state at input optical power $P_{in} = (14 \pm 1)$ μW.

We show the onset of spontaneous synchronization by switching their optical coupling on. Using the heating laser, we tune the optical coupling to its maximum value, indicated by the dashed white line ($T_R - T_L = 0$) in figure 4.4b. The laser frequency sweeping is performed at various optical power levels corresponding to different effective mechanical coupling strength. The optical power ranges from slightly above the estimated oscillation threshold (i.e weaker mechanical coupling), $P_{\text{th}}^{(L,R)} \approx (640, 880)$ nW, up to several times their threshold power (i.e. stronger mechanical coupling). At a relative low input power, $P_{\text{in}} = (1.8 \pm 0.2)$ μW, the mechanical peaks at f_R and f_L are simultaneously observed on the RF spectrum shown in figure 4.8c, below the dashed-white line. When the laser frequency is closer to the optical resonant frequency, more energy is available and the L OMO starts self-sustaining oscillation. Since cavity R has a higher oscillation threshold, due to its lower mechanical quality factor,

it requires more optical power and only oscillates at a redder detuning; it can be noticed from figure 4.8c that both OMOs oscillate close to their natural frequency. Therefore they exhibit asynchronous oscillations at this lowest power level. At a higher input optical power level of $P_{\text{in}} = (11 \pm 1)$ µW, the first oscillation takes place at $\Delta\omega_L/2\pi \approx -0.10$ GHz, and similarly to the case shown in figure 4.8c, the L OMO oscillates first. However, as the laser frequency further moves into the optical resonance, there is enough energy for both OMOs to start self-sustaining oscillations; the two OMOs spontaneously oscillate in unison at an intermediate frequency of $f_S = \Omega_S/2\pi = 50.37$ MHz due to the increased effective mechanical coupling, which is a clear sign of synchronization. At this time, the output optical RF power is increase by more than 5 dB in comparison with the L OMO oscillating only case showing that the two OMOs are phase-locked. At an even higher optical input power, $P_{\text{in}} = (14 \pm 1)$ µW, the OMOs do not oscillate individually, instead they go directly into synchronized oscillations above the white-dashed line in figure 4.8e.

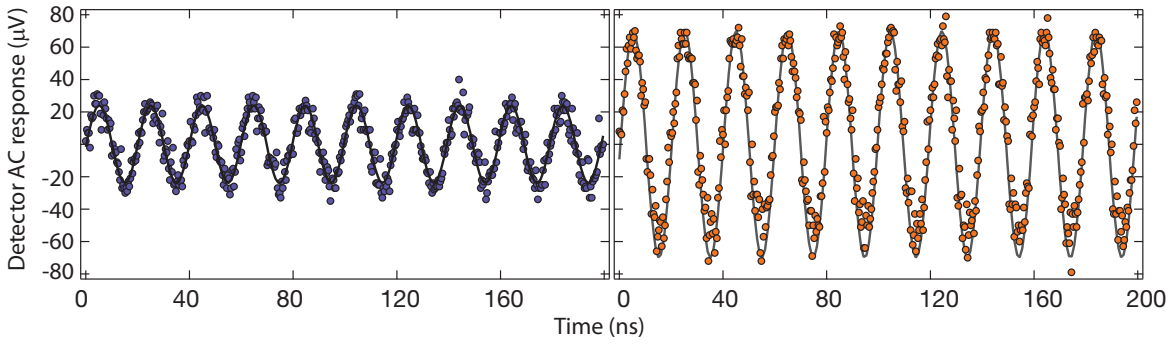

Figure 4.10: **Detector voltage time trace for the L OMO oscillating only state (left) and the synchronized state (right).** The synchronized optical RF power is more than 3 time higher than the L OMO oscillating only state.

We record the real-time trace of the output detector signal with an oscillo-

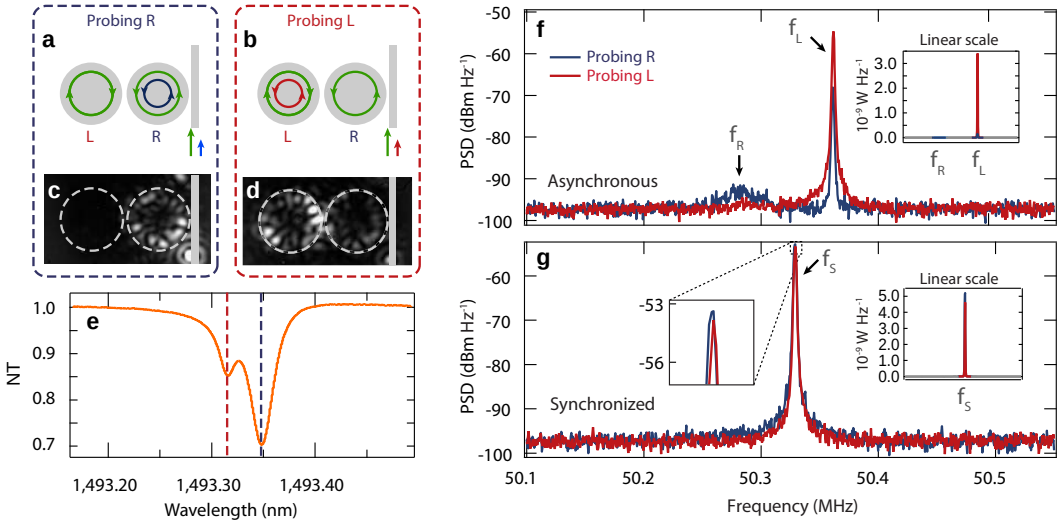

Figure 4.11: **Pump-probe measurements of the oscillations of individual OMO operating as in fig. 4.8d.** (**a**,**b**,**c**,**d**) The uneven probe intensity distribution of the cavities, observed by an infrared CCD camera when the pump laser is off. (**e**) Normalized transmission (NT) spectrum for the probe resonances. The red (blue) dashed line corresponds to the probe wavelength region for probing the *L* (*R*) OMO, as illustrated in (a,b). (**f**) The red (blue) curve is the *L* (*R*) cavity probe transmission RF spectrum when the two OMOs are asynchronous: a strong peak at f_L is observed but with very different amplitude for two probing conditions.(**g**) Same curves shown in (f) but with the OMOs synchronized: the two probing conditions have almost identical amplitudes.

scope for both the asynchronous state (between dashed and solid line in Fig 4.9b) and the synchronized state (above solid line in Fig 4.9b). As shown in the RF power spectrum in Fig 4.9b and figure 4.10 The oscillation output RF power is increased by more than 5 dB as a the two OMO synchronizes. This is expected since when both OMOs are synchronized, their phases add coherently result in a maximum of four-fold (6dB) increase in the total output power.

4.4.6 Pump-Probe Confirmation of Synchronization

To experimentally verify that both structures are indeed oscillating at the synchronized frequency, we probe the mechanical oscillation of each cavity individually. This demonstrates that the single oscillation peaks observed in figures 4.8d,e are not caused by one OMO resonantly driving the other; it also verifies that amplitude death of one of the OMOs does not occur, a known phenomenon in coupled nonlinear oscillators [64]. Therefore, the pump probe measurements provide direct evidence for the synchronization of the two OMOs. The individual probe of each cavity, as shown in figure 4.3, relies on the asymmetric coupling of one the higher order optical supermodes. This asymmetry arises due to their different optical resonant frequency which stems from the slight difference in the geometry of the two OMOs. This leads to a different mode splitting for the higher and lower order optical modes. In the devices we have tested, the majority of them show similar non-identical mode splitting.

Due to its lowers optical quality factor (Q) and reduced optomechanical coupling g_{om}, the threshold power for self-sustaining oscillations [6] of the probe resonance is $P_{th_{probe}} \approx 20$ mW, which is roughly $20,000$ times larger than the pump resonance threshold optical power $P_{th_{pump}} \approx 1$ µW. We used a probe power of $P_p = (20 \pm 2)$ µW, ensuring a low-noise detected probe signal without affecting the cavity oscillation dynamics. We used a weak CW probe laser to excite an optical resonant mode that is not strongly coupled between the two OMOs (figure 4.3 a,b); this scheme allows us to selectively probe the oscillations of the L or R OMO. While these probe optical modes exhibit a low optical quality factor ($Q_{opt} \approx 4 \times 10^4$) that minimizes probe-induced perturbations to the mechanical oscillations, the pump condition is identical to the one used in figure

4.8d. When the L OMO is probed, and the pump detuning range is between the dashed and solid lines in figure 4.8d, the probe RF spectrum shows a strong peak at f_L, which is shown in the red curve in figure 4.11d. When the R OMO is probed, a peak also appears at this frequency, but it is 13 dB weaker as shown in the blue curve in figure 4.11d; a weak peak at f_R can also be noticed on the blue curve, indicating small amplitude oscillations of the R OMO. These results confirm that the oscillation state is very asynchronous in this detuning range with the L OMO oscillating at much larger amplitude. When the pump laser detuning is above the horizontal solid line in figure 4.8d there is only a single RF peak at the synchronized frequency f_S when probing either OMO (figure 4.11e); moreover, they differ in amplitude by less than 0.5 dB. This shows that both cavities are indeed oscillating with similar strength at the synchronized frequency.

4.5 Synchronization Numerical Simulation

4.5.1 Simulation approach

We confirm that the OMOs are indeed synchronized by performing numerical simulations corresponding to each of the power levels we tested. To simulate the synchronization dynamics and obtain the results shown in figure 4.12, we numerically integrate the system of equations (4.1), including the displacement dependent optical resonant frequencies, i.e. $\omega_{1,2}(x) = \omega_{1,2} + g_{om}x_{1,2}$, together with the two harmonic oscillator equations (4.10). This is accomplished using the *NDSolve* function in the commercial software Mathematica®. In the absence

of the random thermal noise force in Eq. (4.10), it is numerically challenging to capture the dynamics before the regenerative oscillation threshold is reached, this is because the steady-state is a static one, i.e., $\dot{x}_{1,2} = 0$. To overcome this issue we add a weak (low-temperature $T = 1$ K) noise that prevents the dynamics to reach such static equilibrium. Since *NDSolve* is a deterministic solver we include the thermal drive by assigning to $F^T_{1,2}(t)$ the outcome of a random variable with with expectation value and correlation function given by

$$\left\langle F_i^T \right\rangle = 0 \tag{4.18}$$

$$\left\langle F_i^T(t) F_i^T(t+\tau) \right\rangle = 2k_B T m^{(i)}_{eff} \Gamma_i \delta(\tau), \tag{4.19}$$

where k_B is the Boltzmann constant. The discontinuity of this random driving term can lead to instabilities in *NDSolve*, to overcome this we smooth out thenoise term by interpolating the random force with a correlation time $t_c = (2\pi/\Omega_i)/30$. Such short correlation time ensures that the noise power spectrum density (PSD) is white within the frequency range of interest.The reliability of this approach is confirmed by verifying that for weak pump powers ($P \ll P_{th}$), the integrated power spectrum density $S_{x_i}(\Omega) = |x_i(\Omega)|^2$ satisfy the fluctuation-dissipation theorem [65].

$$\left\langle x^2(\Omega) \right\rangle = \frac{1}{2\pi} \int_0^\infty S_{xx}(\Omega) d\Omega = \frac{k_B T}{2 m^{(i)}_{eff} \Omega_i^2} \tag{4.20}$$

A complete analysis of the noise in synchronized systems is beyond the scope of this work, since an accurate numerical noise dynamics will require the simulation of the coupled non-linear stochastic dynamics of the optomechanical cavities[66, 67]. The computational complexity of such systems is also high due to the requirement for slow convergence, first order, fixed time step simulation [68, 69, 70].

4.5.2 Simulation results

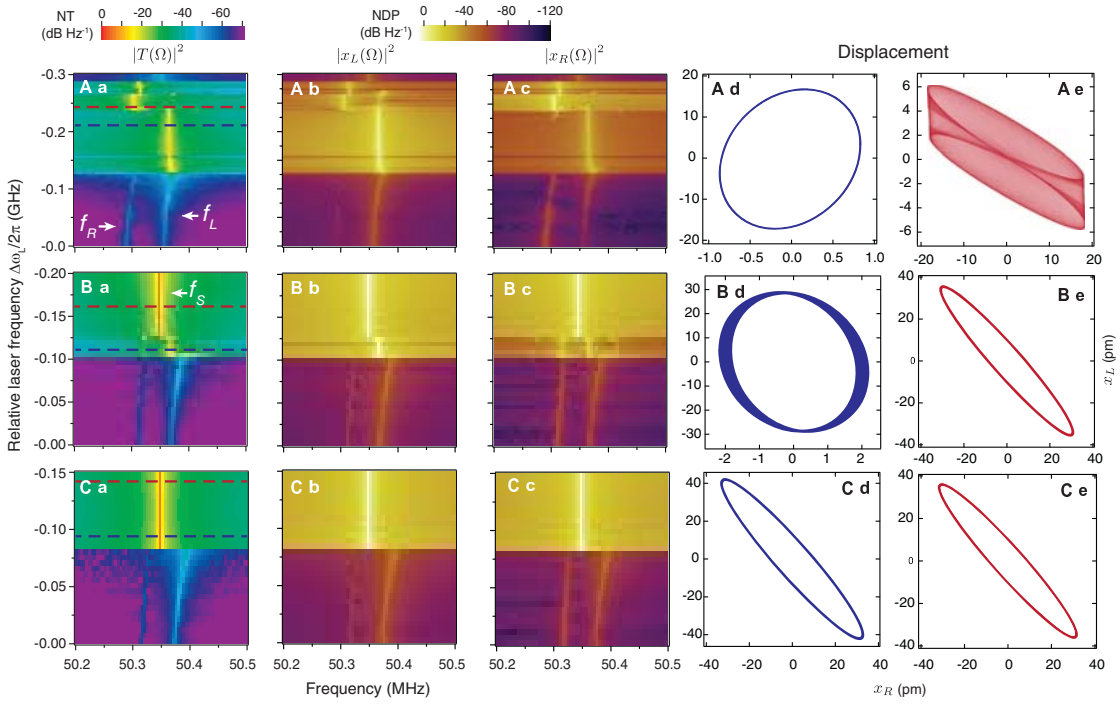

Figure 4.12: **Numerical simulation of the coupled oscillation dynamics**. From **a** to **e**: transmission RF spectra, displacement power RF spectra of the L and the R OMOs, and the displacement phase diagram of the L and the R OMOs, for input powers at (**A**)P_{in} = 4.9 µW, (**B**)P_{in} = 15.8 µW and (**C**) P_{in} = 17.9 µW. x_L (x_R): displacement of the L and R OMOs.

The simulation also allows us probe not only the optical transmission PSD, but also the mechanical displacement PSD and time series of each OMO. The complete simulation results for the pump laser powers described previously are shown in fig. 4.12. The only parameter we adjusted to obtain the maps shown in the experimental measurements and 4.12 was the optical pump power.

In figures 4.12A (P_{in} = 4.9 µW), the mechanical power spectrum of the oscillators (fig. 4.12A(b,c)) shows that for ($-0.25 < \Delta\omega/2\pi < -0.13$ GHz), only L

OMO is oscillating; the R OMO is forced to oscillate at the L OMO's frequency but have not yet reached its oscillation threshold. This is illustrated by the displacement state space figures shown in fig. 4.12A(e) for $\Delta\omega/2\pi = -0.21$ GHz (blue dashed line in fig. 4.12A(a)), note that $|x_L|$ is about 20 times larger than $|x_R|$. At $\Delta\omega/2\pi = -0.25$ GHz, marked by the red-dashed line in fig. 4.12A(a), the situation changes and the R OMO oscillates with larger amplitude ($|x_R| \approx 3.5|x_L|$) but at different frequencies; the result is a Lissajous figure that fills in the whole state space.

In figures 4.12B ($P_{in} = 15.8$ μW), in the asynchronous region, indicated by the blue dashed line, the L OMO oscillates with an amplitude roughly 15 times of the R OMO in agreement with the measured RF spectrum and the pump probe measurement. In the unified frequency region, for both power levels $P_{in} = 15.8$ μW and $P_{in} = 17.9$ μW in fig. 4.12C, the phase diagram shows the two oscillators are synchronized and their amplitude differ less than 20% in agreement to the pump-probe measurements. The synchronization phase for figs. 4.12C(d-e) is roughly $\phi = 160°$, also all the simulations for our system resulted in phase differences close to π, in agreement with the discussion in [49] that the anti-phase synchronization is a more stable state when the oscillations amplitude x_L, x_R are not identical. The simulated spectra in figure 4.12 exhibit all the essential features observed and show good agreement with the measured spectra. It also allows us to confirm under which conditions the two OMOs are indeed oscillating.

The criteria for the optimum fitting is the matching of the laser frequency at which the bifurcation occurs, which is sufficient for explaining all of the nonlinear phenomnena observed. The difference in the simulation power level and

experimentally measured power level may be due to the variations in etched geometry, film thickness and optical losses. Fitting the entire spectra may provide a closer numerical match but it requires a full analysis taking account of of non-linear error propagation, detector and spectrum analyzer response function and multidimensional fitting that is beyond the scope of this thesis.

4.6 Toy model for synchronization

In this section we derive an approximate model to describe the essential features of our coupled oscillators. Although we develop a first order linear approximation of the two coupled optomechanical oscillators, **they constitute an intrinsically a nonlinear system**, as described in detail elsewhere [49].

4.6.1 Optically mediated mechanical coupling

The optical force driving terms in Eqs. (4.10) can be written in terms of the diagonal modes $b_{(m,\pm)}$ from Eq. (4.15) by using Eqs. (4.3). As in section 4.4.2, for large optical coupling the terms are only resonant with the driving laser one at a time, therefore we can focus on the effect of a particular choice of $(m, \pm)$. To simplify the notation we use $\Delta_{0(m,\pm)} \equiv \Delta_m$ and $b_{(m,\pm)} \equiv b_m$ below. We also assume that effective motional mass of the individual oscillators are identical, i.e. $m_{\text{eff}}^{(j)} = m_{\text{eff}}$. The driving force in each oscillator is proportional to $|b_m|^2$,

$$F_{\text{opt}}^{(j)} = \frac{g_{\text{om}}}{\omega_{0(m)}}|b_m|^2 = -\frac{g_{\text{om}} P_{in}\gamma_1\eta_{c1}}{4\omega_{0(m)}}\left|\sum_{p,q}\frac{i^{p+q}J_p(\mu_1)J_q(\mu_2)\,e^{\mathrm{i}(p\Omega_1+q\Omega_2)t}}{\bar{\gamma}/2 + i(-\Delta_m + p\Omega_1 + q\Omega_2)}\right|^2, \tag{4.21}$$

which contains both DC terms and oscillatory terms.

Although our oscillators may exhibit large oscillation amplitude ($g_{om}x_j > \bar{\gamma}$), it is instructive to analyze the small amplitude dynamics arising for the the driving term in Eq. (4.21). This treatment is entirely analogous to the one used to derive the optomechanical damping and spring effect in uncoupled OMO's [56, 58]. For the small amplitude oscillation, the modulation parameters are small, i.e., $\mu_i = g_{om}x_i/\Omega_i \ll 1$, therefore the Bessel functions in (4.21) can be approximated by their small argument limit, $J_n(\mu) \approx \frac{1}{n!}(\frac{\mu}{2})^n$. We neglect any terms which are quadratic in the $\mu_{1,2}$, which also account for summing Eq. (4.21) only over $p, q = 0, \pm 1$ since higher order terms will result in terms which are $O(\mu^2)$. The $p, q = 0$ terms result in a DC component of the force,

$$F^{(j)}_{\mathrm{opt}_{DC}} = \sum_{j=L,R} \frac{g_{\mathrm{om}}}{\omega_{0(m)}} \left(\frac{P_{in}\gamma_1\eta_{c1}}{\Delta_m^2 + (\bar{\gamma}/2)^2} \right). \tag{4.22}$$

The impact of the DC term above is to shift the static equilibirum position of the mechanical oscillators. As a result, the actual optical detuning is also shifted, to account for this DC shift we substitute $\Delta_m \to \Delta'_m$, where $\Delta'_m = \Delta_m + g_{\mathrm{om}}(x_1 + x_2)$.

When $p, q = \pm 1$ the resulting terms are quadratic in $\mu_{1,2}$ and **will be neglected in this first order approximation**, therefore the lowest order AC terms are given by combinations $(p, q) = (0, \pm 1)$ and $(p, q) = (\pm 1, 0)$.

$$F^{(j)}_{\mathrm{opt}_{AC}} = \frac{g^2_{\mathrm{om}}P_{in}\gamma_1\eta_{c1}}{\omega_{0(m)}} \sum_{j=L,R} A_j \left[-\cos(\Omega_j t) f_{\mathrm{I}}(\Delta'_m, \Omega_j) + \sin(\Omega_j t) f_{\mathrm{Q}}(\Delta'_m, \Omega_j) \right] \tag{4.23}$$

where the functions $f_{I,Q}(\Delta)$, which correspond to the in-phase ($\propto \sin(\Omega_j t)$) and quadrature of phase component ($\propto \cos(\Omega_j t)$) of the AC force, are given by

$$f_{\mathrm{Q}}(\Delta'_m, \Omega_j) = \frac{4(\frac{\bar{\gamma}}{2})\Delta'_m}{2\Omega_j^2\left((\frac{\bar{\gamma}}{2})^4 - \Delta'^4_m\right) + \Omega_j^4\left((\frac{\bar{\gamma}}{2})^2 + \Delta'^2_m\right) + \left((\frac{\bar{\gamma}}{2})^2 + \Delta'^2_m\right)^3}, \tag{4.24a}$$

$$f_{\mathrm{I}}(\Delta'_m, \Omega_j) = \frac{2\Delta'_m\left((\frac{\bar{\gamma}}{2})^2 + \Delta'^2_m - \Omega_j^2\right)}{2\Omega_j^2\left((\frac{\bar{\gamma}}{2})^4 - \Delta'^4_m\right) + \Omega_j^4\left((\frac{\bar{\gamma}}{2})^2 + \Delta'^2_m\right) + \left((\frac{\bar{\gamma}}{2})^2 + \Delta'^2_m\right)^3}. \tag{4.24b}$$

We can now use the transformations $\sin(\Omega_j t) \to x_j/A_j, \cos(\Omega_j t) \to \dot{x}_j/(A_j\Omega_j)$ and rewrite (4.23) as

$$F^{(j)}_{\mathrm{opt}_{AC}} = \frac{g^2_{\mathrm{om}} P_{in}\gamma_1\eta_{c1}}{\omega_{0(m)}} \sum_{j=L,R}\left[-x_j f_{\mathrm{I}}(\Delta'_m,\Omega_j) + \frac{\dot{x}_j}{\Omega_j} f_{\mathrm{Q}}(\Delta'_m,\Omega_j)\right] \tag{4.25}$$

Equation (4.25) above shows that for each oscillator the driving force will have a component proportional to its displacement (x_j) and its velocity ($\dot{x}_j$). But there are also terms proportional to the displacement and velocity of the opposing OMO; these are the terms that couple the two OMOs and form the basis for synchronization in our system. **Note that if higher order terms were kept in the expansion of Eq.** (4.21)**, nonlinear terms would appear in Eq.** (4.25).

Above we derived the small amplitude form of the optical forces driving our coupled oscillators, we did not use the fact that our cavities are in the so-called unresolved sideband regime where the mechanical frequencies are much smaller than the optical linewidth, i.e., $\Omega_j/\bar{\gamma} \approx 0.2 \ll 1$. In this limit, Eqs. (4.24) can be written as,

$$f_{\mathrm{Q}}(\Delta'_m) \approx \frac{4(\frac{\bar{\gamma}}{2})\Delta'_m}{\left((\frac{\bar{\gamma}}{2})^2 + (\Delta'_m)^2\right)^3}, \tag{4.26a}$$

$$f_{\mathrm{I}}(\Delta'_m) \approx \frac{2\Delta'_m}{\left((\frac{\bar{\gamma}}{2})^2 + (\Delta'_m)^2\right)^2}. \tag{4.26b}$$

Now we can write the (4.10) as two coupled harmonic oscillators,

$$\ddot{x}_1 + \Gamma'_1\dot{x}_1 + (\Omega'_1)^2 x_1 = -k_{\mathrm{I}}x_2 + k_{\mathrm{Q}}\dot{x}_2, \tag{4.27a}$$

$$\ddot{x}_2 + \Gamma'_2\dot{x}_2 + (\Omega'_2)^2 x_2 = -k_{\mathrm{I}}x_1 + k_{\mathrm{Q}}\dot{x}_1, \tag{4.27b}$$

where the modified frequency and damping rate are given by (assuming $\delta\Omega_j^2 \approx$

$2\Omega_j\delta\Omega_j$),

$$\Gamma'_j = \Gamma_j - \beta_j f_Q(\Delta'_m), \tag{4.28a}$$

$$\Omega'_j = \Omega_j + \frac{\beta_j}{2} f_I(\Delta'_m), \tag{4.28b}$$

$$k_Q^{(j)} = \beta_j \Omega_j f_Q(\Delta'_m), \tag{4.28c}$$

$$k_I^{(j)} = \beta_j \Omega_j f_I(\Delta'_m) \tag{4.28d}$$

with $\beta_j = g_{\mathrm{om}}^2 P_{in}\gamma_1\eta_{c1}/(m_{\mathrm{eff}}^j \omega_{0(m)}\Omega_j)$.

Therefore, in the small modulation regime ($\mu_{1,2} \ll 1$), our system resemble harmonic oscillators in which both the damping and frequency are controlled by the optical field; this result is exactly what one would get from uncoupled OMOs. With the reduction of the mechanical damping rate for a blue detuned laser. ($\Delta'_m > 0$), these two damped oscillators may undergo a bifurcation when the effective damping rate (Γ'_i) reverses sign. In this first order approximation there is no additional nonlinearity to prevent the oscillations to grow unbound, however it is known that the higher order terms in the force expansion ((4.21)) will balance the amplitude growth and eventually lead to a stable periodic orbit (limit cycle) [45, 46, 49]. The optical coupling in our system couples the two harmonic oscillators with both amplitude and velocity dependent terms, with coupling strengths k_I, k_Q, respectively. The functional dependence of such coupling is the same as the self-induced optical spring and damping rate, as given by (4.28).

4.6.2 Approximate Kuramoto model

In the small amplitude approximation that lead to Eq. (4.27), one can also derive slowly-varying phase and amplitude equations that describe the dynamics

of our system. To accomplish this we assume the following form for our displacement amplitudes,

$$x_1(t) = r_1(\tau) \exp \mathrm{i}\phi_1(\tau) \exp \mathrm{i}\Omega t, \tag{4.29a}$$

$$x_2(t) = r_2(\tau) \exp \mathrm{i}\phi_2(\tau) \exp \mathrm{i}\Omega t. \tag{4.29b}$$

where $\Omega = (\Omega_1 + \Omega_2)/2$ is the average frequency of oscillation. Substituting this ansatz in Eqs. (4.27) and assuming that the negative damping induced by the optical wave exactly balances the intrinsic viscosity of the oscillators ($\Gamma' \approx 0$) we obtain the following amplitude and phase equations,

$$\dot{r}_1 = -\frac{k_Q r_2}{4\Omega^3}\left(\left(\Omega^2 + \Omega_2^2\right)\cos(\Delta\phi)\right) - \frac{k_\mathrm{I} r_2 \sin(\Delta\phi)}{2\Omega}, \tag{4.30a}$$

$$\dot{r}_2 = -\frac{k_Q r_1}{4\Omega^3}\left(\left(\Omega^2 + \Omega_1^2\right)\cos(\Delta\phi)\right) + \frac{k_\mathrm{I} r_1 \sin(\Delta\phi)}{2\Omega}, \tag{4.30b}$$

$$\dot{\Delta\phi} = 2\Delta\Omega + \frac{\left(R^2 - 1\right)\cos(\Delta\phi)\left(\gamma k_\mathrm{Q} + 2k_\mathrm{I}\right)}{2R\Omega} + \frac{\left(R^2 + 1\right)\sin(\Delta\phi)k_Q}{R} \tag{4.30c}$$

where $\Delta\phi = \phi_1 - \phi_2$, $R = r_1/r_2$ and $\Delta\Omega = \Omega_1' - \Omega_2'$. Note that in this approximation the limit cycle has zero amplitude; this is the case because we neglected the higher order terms when deriving Eq. (4.27). Despite such limitations of this toy model, the phase dynamics given by Eq. (4.30) enables us to visualize how does the Arnold tongue ($|\Delta\Omega| < k_\mathrm{I}$) behaves as we vary the laser detuning. We assume that limit cycles of the individual oscillator will have similar amplitude ($R = 1$) and require $\dot{\Delta\phi} = 0$ for a synchronized oscillation. When $|\Delta\Omega| < k_\mathrm{I}$ this conditions can be satisfied and defines an Arnold tongue for this simple model; inside the Arnold tongue the system can synchronize ($\dot{\Delta\phi} = 0$). In Fig. 4.13 we show the Arnold tongue plot for our system, in Fig. 4.13a we plot it in the usual way, as function of the coupling coefficient (k_I), whereas in Fig. 4.13b we plot the tongue as a function of the laser detuning by using Eq. (4.28). Due to the model simplicity and lack of higher order terms, it does not predict the precise

values for the synchronization region observed in the experiment (Fig. 4.13b), however it does agree qualitatively; for higher optical power levels the tongues get wider and allows a given mechanical frequency difference to synchronize at larger detuning, as shown in figure 3 of the main text.

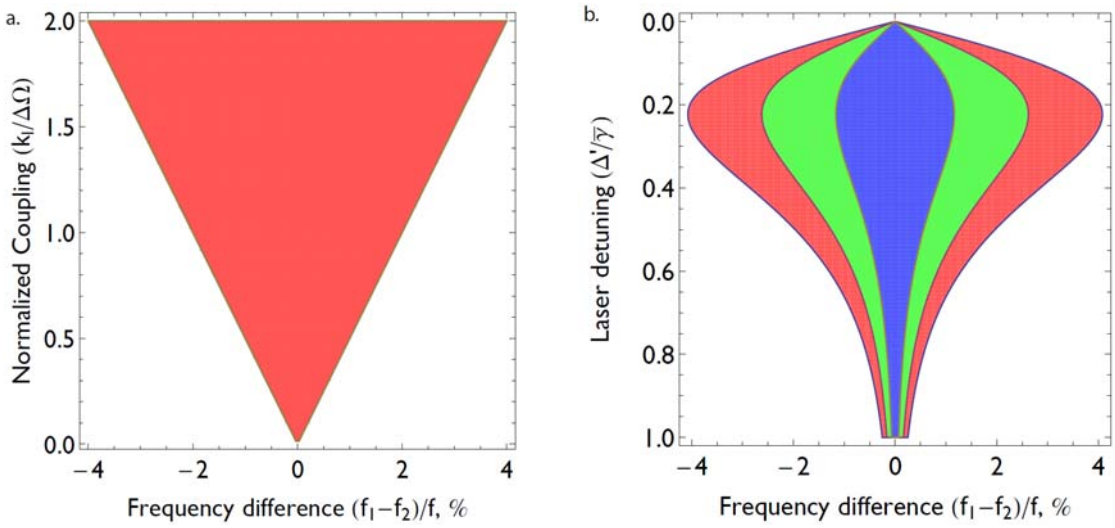

Figure 4.13: **Arnold tongue for the simplified Kuramoto model, inside the tongues the system can exhibit synchronized oscillation.** (**a**) Usual tongue as a function of the coupling parameter k_I. (**b**) Tongue when k_I is explicitly written in terms of the laser-cavity detuning. The three tongues in (b) are obtained with the optical input power values of $P_{in} = 1, 5, 15$ µW, the lower power is the blue whereas the highest power is red tongue. f is the average mechanical frequency of the oscillators.

4.7 Conclusion

We have demonstrated the onset of synchronization between two optomechanical oscillators coupled only through the optical radiation field. The ability to control the coupling strength is promising for realizing oscillator networks in

which the oscillators can be addressed individually. Furthermore, established and future micro-photonics techniques such as electro-optic and thermo-optic techniques can now be extended to switch, filter and phase shift the coupling of these oscillators. These results may enable a new class of devices in sensing, signal processing and on-chip non-linear dynamical systems.

CHAPTER 5

SYNCHRONIZATION IN OPTOMECHANICAL OSCILLATOR ARRAYS

5.1 Background

Synchronization many coupled oscillator systems is a ubiquitous phenomena found in nature [34]. Heart beat is a result of synchronized motion of pace maker cells [71], circadian rhythm arises because of coordinated body physiology[72] and power grid relies on collective dynamics of many power generators [73]. On the nanoscale, synchronization has emerged as a paradigm for emergent collective dynamics in complex systems [40, 74, 75, 76]. Nanomechanical oscillators fabricated on a chip naturally have a spread of mechanical frequencies due to unavoidable fabrication variations [77]. Synchronization could allow these oscillators to work coherently together enabling high power and low noise integrated frequency sources which play a key role in the essential time keeping in modern technology [42].

Synchronizing a large array of oscillators could dramatically improve the phase noise performance of the oscillation signals in comparison to operating individually [78, 79]. Phase noise describes the fluctuation of the phase of the oscillation signal in a self-sustaining oscillator system, which is a key figure of merit in characterizing an oscillators performance [80]. Theory predicts that the phase noise is reduced to $1/N$ as N oscillators in a network are synchronized [79, 81]

The roadblock in realizing a large synchronized oscillator network on a chip is the need for scalable oscillator units and means to couple them efficiently

and controllably [82, 45]. Synchronization between only two nanomechanical oscillators has been experimentally demonstrated in nanomechanical systems coupled through mechanical connections [42], electrical capacitors [83] , off-chip connections [84] and more recently though an optical cavity [15, 85]. However all these approaches are not scalable. Mechanical connections are limited in bandwidth and are lossy due to the necessary anchors. Capacitive coupling is limited in topology and is vulnerable to environmental electric field.

Here we show that synchronization can occur in a large array of nanomechanical oscillators mediated through a common optical cavity field, and demonstrate that the noise performance in the synchronized oscillator arrays can be reduced by almost 10 dB below the noise performance of an individual oscillator. We address the scaling and coupling challenging by showing experimentally that nanomechanical oscillator arrays with up to seven oscillators can be synchronized using light with less than a milliwatt of optical power.

5.2 Mechanical coupling mediated through a common optical cavity field

Free running micromechanical oscillators can be synchronized when coupled purely through a common electromagnetic field as predicted by theories [82, 46, 49]. A conceptual view of array of mechanical resonators coupled through a common electromagnetic field is illustrated in Figure 1a. Each mechanical resonator possesses a slightly different frequency of oscillation (Ω_i) but are only connected through a common optical field (blue background). When a continuous wave laser is coupled to a common electromagnetic field mode

spanning several micromechanical oscillators, the light can provide both the drive for self-sustaining oscillations and the necessary coupling between the individual oscillators for synchronization through optical forces. The frequency for each individual mechanical oscillator is set by their natural mechanical frequency Ω_i. When the laser power is just above the self-sustaining oscillation threshold of the mechanical oscillators, and the mechanical frequencies of these individual oscillators are slightly different, they are expected to vibrate at their own frequencies. When the laser power is high and the coupling is strong enough to overcome the difference in Ω_i, the mechanical oscillators can reach synchronization

The effective coupling between the mechanical resonators can be visualized through the following equation

$$\begin{aligned} \ddot{x} + \Gamma_i \ddot{x} + \Omega_i^2 &= F_{\text{opt}}^{(i)}, \\ F_{\text{opt}}^{(i)} &\propto |b(x_1, ..., x_j)|^2 \end{aligned} \tag{5.1}$$

where x_i,Γ_i,Ω_i are the mechanical displacement, damping and the mechanical frequency of the ith OMO and $b(x_1, , x_j)$ is the coupled optical supermode that spatially spanning all cavities. It is clear from the equation above that the optical force (F_{opt}) depends on the energy stored in the optical supermodes which is affected by the displacement of each individual cavity. Therefore the optical field provides an effective nonlinear mechanical coupling between the different oscillators that form the basis for synchronization [15]. The onset of synchronization, which intrinsically relies on nonlinearity [50], could therefore be captured as F_{opt} is increased through increasing the optical driving power[85, 15]

The individual oscillator is we use here consists of a double-disk OMO con-

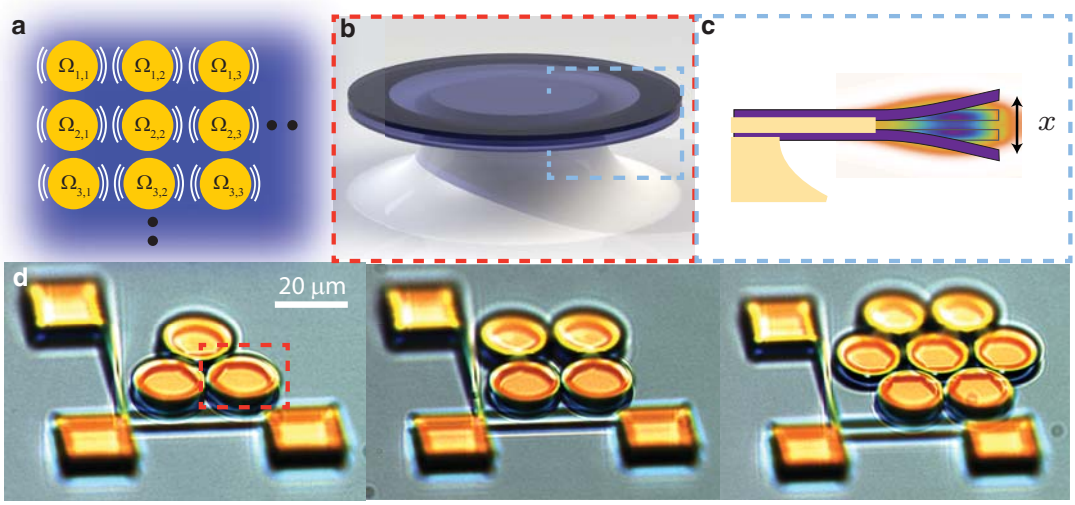

Figure 5.1: **Experiment concepts** (**a**) Concept of mediating coupling between mechanical oscillators (yellow) by a coupled global optical field (blue). The optical field provide energy for each mechanical oscillator to vibrate at their natural frequencies $\Omega_{i,j}$ and also provide coupling between each mechanical oscillator. When the optical coupling is strong, the oscillators synchronize and vibrate at a common frequency. (**b**) A schematic of each individual double-disk. The edges are partly suspended to allow for mechanical vibration (**c**) Cross-section of a double-disk showing the mechanical and the optical mode shape. (**d**) Microscope images of coupled optomechanical double-disk oscillator arrays. The oscillators are mechanically separated by a narrow gap (~ 150 nm) and coupled solely through the optical evanescent field. The squares and strings consists of tapered fiber support.

sisting composed of two free-standing silicon nitride circular edges that support high quality (Q) factor optical and mechanical modes as shown in figure 5.2b [86, 87]. The co-localized modes lead to a strong coupling between the optical and the mechanical degree of freedom. When the cavity is excited by a continuous wave laser above the oscillation threshold, the mechanical edges oscillate coherently and modulate the laser producing a radio frequency (RF) tone at the mechanical frequency of the vibrating edges. The loaded optical quality factors

of these resonators are $Q_o \sim 500,000$. The measured mechanical frequencies of the OMOs are centered at ~ 132.5 MHz with quality factors of $Q_m \sim 1100$. Fabrication variation causes the mechanical frequency of different OMOs in an array to spread around ± 0.5 MHz. The interaction strength between the optical and the mechanical mode is characterized by the optomechanical coupling strength $g_{\text{om}} = d\omega/dx \sim 2\pi \times 50$ GHz/nm [15].

We fabricate an array of micromechanical oscillator arrays with double-disk OMOs that are optically coupled through the evanescent field27. The OMOs are physically separated by a narrow gap (~ 150 nm) which precludes any mechanical connections while the optical evanescent field can still propagate through the gap. Mechanical coupling through the substrate connection is negligible as the mechanical mode we excite is a high Q mode that is well isolated from the substrate [87].

The challenge in coupling optically large arrays of mechanical structures is the variation in the natural variations of their optical frequencies of each of the oscillators due to variation in the exact fabricated dimensions. We overcome this challenge by ensuring that the optical coupling is large compare to the frequency variation and the individual decay rate of each cavity. The optical coupling strength we designed ($\kappa_{(i,j)} \sim 5$ GHz) is much larger than the optical decay rate of the cavity ($\gamma_i \sim 400$ MHz) and to the cavity optical frequency spread from fabrication variations. This ensures that the optical modes are strongly coupled which means the light travels between the cavities many times before it is lost via other channels.

We excite the optical supermodes that spatially span over all cavities to ensure that there is optical coupling among all cavities (Fig. 5.2a dashed boxes). The strong optical coupling between the optical modes of each individual cavity (a_i) leads to the formation of optical supermodes $b_i(a_i, , a_j)$ that have different optical frequencies and spatial geometries. We can estimate the spatial distribution of the optical supermodes by analytically finding the eigenmode of the coupling matrix using coupled mode theory. Figure 5.2a illustrates the spatial profile of different optical supermodes b_i when the optical resonant frequency of individual cavity (ω_i) is identical. The colored halos around the disks illustrate the field distribution in the particular supermodes. The red and purple highlights a phase difference between the cavity fields. These optical supermodes have different resonant frequencies which are highlighted in figure 5.2a, where the mode shapes are arranged such that the high (low) frequency modes are to the left (right) of the figure. Note that not all supermodes have a field that span over all cavities. We position a tapered optical fiber to the close proximity of one OMO in the arrays to couple light to the system (Fig. 2). We monitor the transmission through the tapered fiber by an amplified photodiode and feed the electrical signal to a spectrum analyzer.

5.3 Optical Transmission

The strongly coupled optical modes can be diagonalized to the optical supermode basis since the optical part of the coupled system is linear. Similar method has been used in previous work of two coupled double disk OMOs [15].

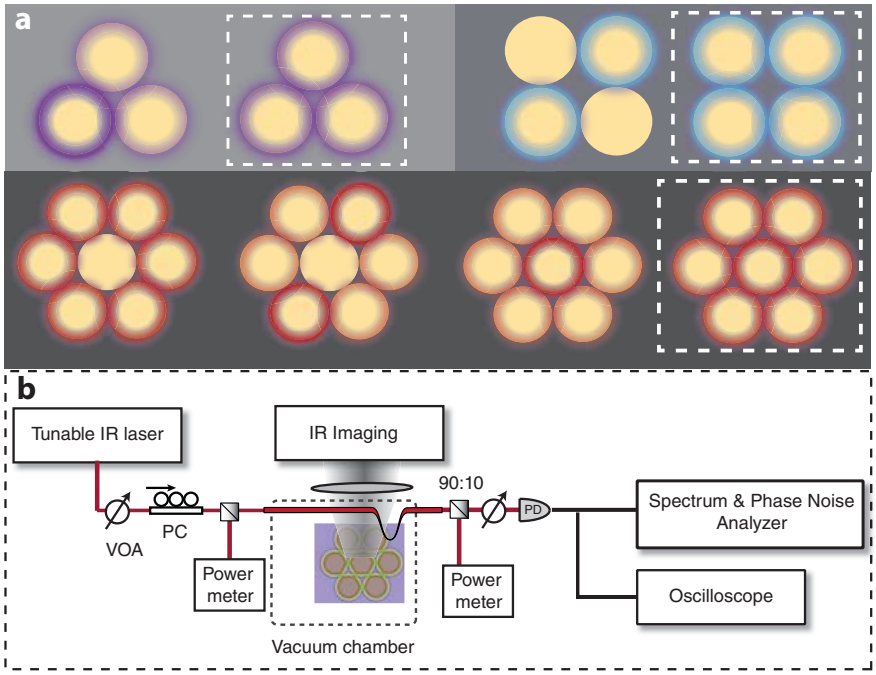

Figure 5.2: **Experimental configuration** (**a**) Optical supermodes spatial structures. The colored halos shows where the optical cavity field resides for different types of arrays. The more opaque colors illustrate higher cavity field intensities when compared to the rest of the cavities. The supermodes that spatially span over all cavities with equal intensities are identified by dashed lines. (**b**) Experimental setup. The coupled optomechanical oscillator array is placed in a vacuum chamber and excited by a tunable infra-red (IR) camera through a tapered optical fiber. The optical transmission is detected by an amplified photodiode and analysed by an oscilloscope and spectrum analyser.

$$\begin{pmatrix} \dot{a}_1 \\ \dot{a}_2 \\ \dots \\ \dot{a}_i \end{pmatrix} = \begin{pmatrix} -\frac{\gamma_1}{2} - \mathrm{i}\omega_1 & \frac{\mathrm{i}\kappa_{12}}{2} & \dots & \frac{\mathrm{i}\kappa_{1i}}{2} \\ \frac{\mathrm{i}\kappa_{21}}{2} & -\frac{\gamma_2}{2} - \mathrm{i}\omega_2 & \dots & \frac{\mathrm{i}\kappa_{2i}}{2} \\ \dots & \dots & \dots & \dots \\ \frac{\mathrm{i}\kappa_{i1}}{2} & \frac{\mathrm{i}\kappa_{i2}}{2} & \dots & -\frac{\gamma_i}{2} - \mathrm{i}\omega_i \end{pmatrix} \begin{pmatrix} a_1 \\ a_2 \\ \dots \\ a_i \end{pmatrix} + \sqrt{\gamma_1 \eta_c} s_1(t) \begin{pmatrix} 1 \\ 0 \\ \dots \\ 0 \end{pmatrix} \tag{5.2}$$

where γ_i, Ω_i are the total damping rate and the resonant frequency of each individual optical mode a_i. κ_{ij} is the optical coupling strength between ith and

jth OMO. η_c is the optical criticality factor, the ratio between the cavity damping rate and the external coupling rate. $s(t)^2$ is the optical power that excites the array of resonators through the first cavity. In the strong coupling regime ($\kappa_{ij} \gg \gamma_i \ \forall i, j$), individual optical modes hybridize and fully splits into optical supermodes b_i where some supermode span over all cavities. The strong coupling is visualized by the fully split optical supermodes shown in the optical transmission in figure 5.3. To visualize the spatial geometry of the optical supermode, we approximateγ_i and Ω_i of individual OMO are identical. We can then exactly diagonalize the coupling matrix in equation 5.2 where the Jacobian would indicate the spatial geometry of the coupled optical mode as shown in figure 5.2.

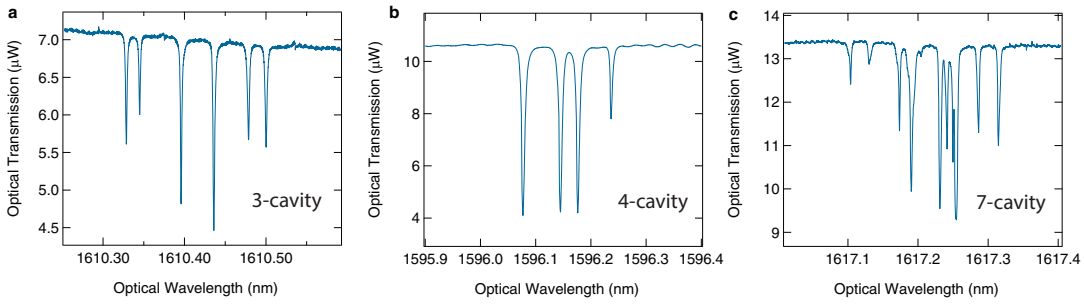

Figure 5.3: **The optical transmission** in the (**a**) three, (**b**)four and (**c**) seven cavity arrays respectively. The well split resonant mode and the high extinction of each split supermodes shows that the optical modes are strongly coupled.

Figure 5.3 shows images from the IR camera when the supermodes spanning over all cavities are excited. It is clear from the image that all cavities light up with approximately equal intensities.

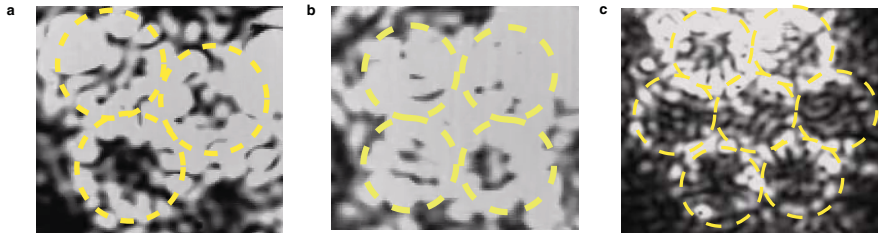

Figure 5.4: **Image of the scattered light** when sychronization is onset for (**a**) three-cavity (**b**) four-cavity and (**c**) seven-cavity arrays. The radius of the disks are 20 μm.

5.4 Mechanical modes

The mechanical modes of the double disk is the flapping mechanical mode where we can control the mechanical frequency of the mode by the undercut depth of the sacrificial silicon dioxide layer. In the particular device we used in the experiment, we fabricated the devices with mechanical frequency near 132 MHz and quality factor near 1000 (Fig. 5.4). In the OMO arrays, when the system is coupled to a laser at very low power, we measured a distribution of mechanical frequencies corresponding to different OMOs. Figure 5.4 shows the mechanical spectrum in the three, four and seven cavity arrays respectively. In the three OMO array, the mechanical frequencies are clearly different where as in the four OMO and seven OMO arrays, the mechanical mode frequencies overlaps.

In synchronized oscillator arrays, the phase noise reduces as the number of synchronized oscillators increase. Experiments and theories [88, 81, 84] show that the noise reduces as $1/N$ where N is the number of synchronized oscillators. This can be intuitively understood as coordinated oscillators while having the same frequency but having an increased effective mass which improves

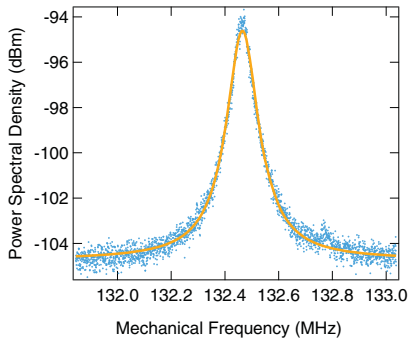

Figure 5.5: **Mechanical spectrum of a single doubled disk OMO forming the array in this experiment.**

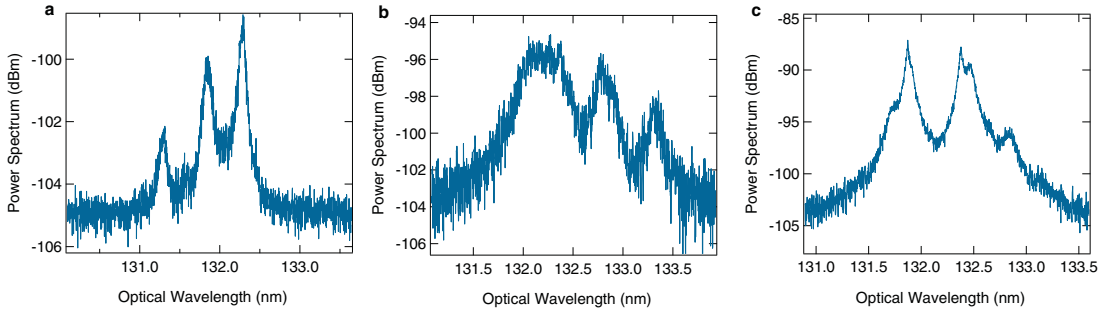

Figure 5.6: **The mechanical spectrum** in the (**a**) three, (**b**)four and (**c**) seven cavity arrays respectively. The disorder in mechanical frequencies is evident from the distribution is evident from the splitting of the peaks.

their resistance to environmental thermomechanical fluctuations. In our system, proving synchronization by studying the dynamics of individual cavities in the arrays is desirable but it is technically challenging given the compact size of the array. Therefore we choose the phase noise as a figure of merit as it is fundamentally limited by the thermomechanical process.

5.5 Synchronization in different sizes of arrays

We show the onset of synchronization by increasing the excitation laser power which effectively increases the coupling between the OMOs. The laser wavelength is blue detuned relative to the spectrum of the even optical supermode (Fig. 5.2a dashed boxes). In the case of three coupled OMO array, as the laser power increases well beyond the oscillation threshold for each individual oscillator, the RF spectrum of the OMOs show strong oscillation peaks as well as sidebands and a broad noise floor (Fig 5.5a). The increase in the noise floor is due to finite interaction between the mechanical modes mediate by the optical field but not yet strong enough to transition into a locked state. This sidebands are formed due to beating between the different mechanical modes observed in other photonic cavity coupled systems. As the laser power further increases, the onset of synchronization (Fig. 5.5a) is evident as the peaks on the RF spectrum merge into a single large peak and the noise floor is reduced. The much weaker sidebands around the main oscillation signal are now due to quasi-periodicity in the synchronized state 20. In the case of four couples OMO array, similar to the three cavity case, the beatingbetween different mechanical modes and the broad noise floor also appears. When the optical power is further increased to $P_{\text{in}} = 360\mu\text{W}$, synchronization is evident again from the appearance of a single oscillation peak (Fig. 5.5b). and from the dro p in the noise floor. In the case of seven coupled OMO array, we observe similar beating behaviours and high noise floor before synchronization. As the optical power increases above the synchronization threshold, the noise floor drops and a single narrow peak appears (Fig. 5.5c).

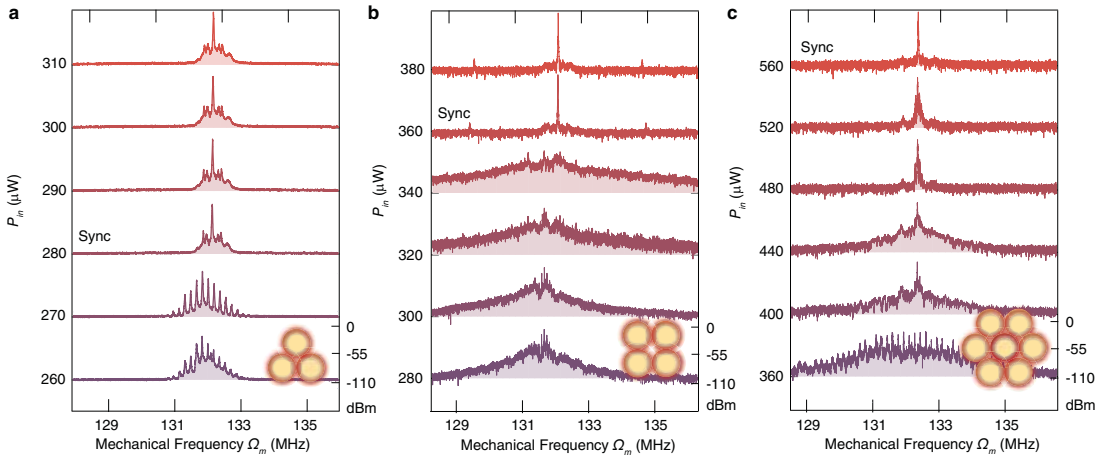

Figure 5.7: **Synchronization in arrays of OMOs** Optical power spectrum of three- **(a)** four-**(b)** and seven-**(c)** OMO system as the input optical power increases. The vertical scale is from -110 dBm to 0 dBm for each trace. Synchronization is characterized by the sudden noise floor drop and the emergence of a single frequency in the optical power spectrum

5.6 Phase noise in synchronized oscillators

Leesons model predicts the phase noise of self-sustaining oscillators from the linewidth of the oscillation signal. The linewidth ($\Delta\Omega$) of a thermally limited oscillator is given by

$$\Delta\Omega = \frac{k_B T}{2P_{\text{out}}}\Gamma_m^2 \tag{5.3}$$

where k_B is Boltzmann's constant, T is the temperature, P_{out} is the output power of the oscillator and Γ_m is the natural damping rate of the oscillator. Since the double disk we use have a small effective mass (m_{eff}), which means a low oscillator power, the phase noise is limited by thermomechanical noise. The oscillator power P_{out} is given by,

$$P_{\text{out}} = \frac{1}{2} m_{\text{eff}} \Omega^2 x^2 \tag{5.4}$$

where x is the displacement amplitude of the oscillator. Equation (5.3) can be represented as,

$$\Delta\Omega = \frac{k_B T}{4 m_{\text{eff}} \Omega^2 x^2} \Gamma_m^2 \tag{5.5}$$

The phase noise performance of an optomechanical oscillator, when limited by thermomechanical noise, improves when the laser power is increased. At high laser driving powers, the phase noise roughly stays constant as the laser power is further increased. We calibrate the single oscillator phase noise performance by measuring the phase noise at 10 kHz carrier offset at different laser driving powers. Figure 5.6 clear shows that the phase noise does not vary significantly when the power is above $4 \times P_{th}$. where $P_th = 10\mu W$ is the typical threshold power for individual OMO. This is in agreement with the experimental observation reported by Mani et. al [89]. and theory by Fong et. al [90].

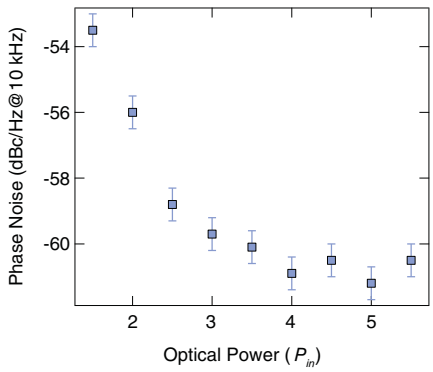

Figure 5.8: **Phase noise of a single OMO as a function of the laser driving power.**

Leeson's model for phase noise [91] states that the phase noise represented in dBc/Hz at an offset frequency of Δf is $L(\Delta f)$ where,

$$L(\Delta f) = 10\text{Log}_{10}\left(\frac{\Delta\Omega}{2\pi\Delta f^2}\right) \tag{5.6}$$

Substituting the parameters and $x \sim g_{om}/\gamma = 10$ pm to equation 5.6, we obtain the thermal mechanical noise limit of our oscillators is −62 dBc/Hz at 10^4 kHz carrier frequency offset, agreeing well with our experimental measurements.

We corroborate the observation of synchronization through monitoring the phase noise of the optomechanical oscillator arrays. The phase noise of the modulated output light is expected to drop as the oscillators are synchronized [79]. This can be used as an indicator for the onset of synchronization when the individual oscillator phase is inaccessible, as observed in many other coupled oscillator systems [92, 93]. We measure the phase noise of our oscillators at 10 kHz offset from the carrier oscillation frequency, where the phase noise of our oscillator is dominated by thermomechanical fluctuation [89, 90, 94], a fundamental limit imposed to the mechanical oscillator due to the thermal bath of the environment. Our individual OMO oscillates with a typical phase noise of - 61±2 dBc/Hz at 10 kHz carrier offset when the OMOs are being driven at high optical driving powers ($\sim 10P_{th}$) in agreement with estimation using Leesons model of thermomechanical noise limited self-sustaining oscillators [91]. To confirm the drop of phase noise can be used to reflect the onset of synchronization in optomechanical systems, we measured the phase noise in a two synchronized OMOs system as previously reported [95]. Indeed, we observe the phase noise dropped by ~3 dB as the two OMOs move from one OMO oscillating state to a synchronized oscillation state. As shown in figure 5.6a, the single OMO phase noise at low power is ~ -60 dBc/Hz and is gradually increased as the laser power is increased. The increase of phase noise is due to phase slipping between the two OMOs [84]. As the OMOs are more and more strongly coupled with the increase of laser power, they are synchronized characterized by a drop

in phase noise of ~ 3 dB below the individual oscillation state. As the oscillators are nearly identical, synchronized oscillations can be viewed as two oscillators working coherently providing a larger effective mass while not reducing the oscillation frequency [94].

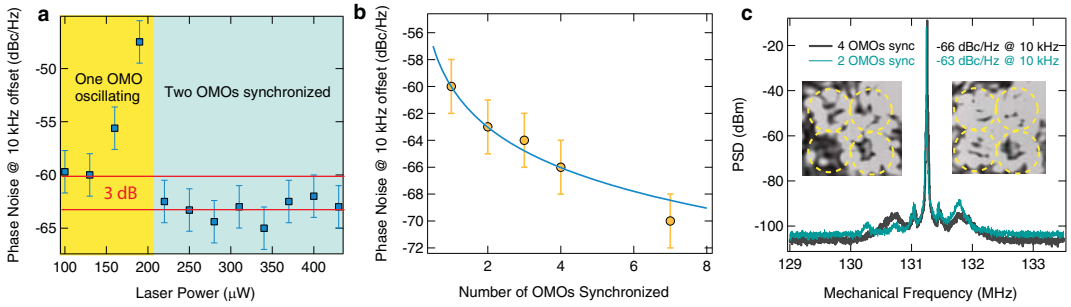

Figure 5.9: **Phase noise reduction in arrays** (**a**) phase noise in a two-OMO system at 10 kHz carrier offset as a the laser power is increased. The noise increases due to mode competition between possible oscillation states and then decreases by ~ 3 3dB below the noise level of one OMO oscillation state. (**b**) The phase noise of the synchronized oscillation signal for different sizes of OMO arrays. The blue curve is the phase noise level predicted by theory for identical synchronized oscillators (**c**) Power spectrum of a state where four OMO are oscillating (black) and of a state two OMO oscillating (green). The phase noise drops by ~ 3 dB following the transition.

We show that in large arrays of OMOs, the phase noise of the synchronized signal can be reduced below the noise of an individual OMOs thermomechanical noise limit by almost 10 dB. We measure the phase noise of each type of array by driving the system at high optical powers and the detuning where the phase noise is a minimum. The lowest phase noises measured in each array of different sizes are plotted in figure 5.6c which is close to the $1/N$ dependence predicted by theory [79, 45].

The drop in phase noise can also be used to indicate the number of OMOs

synchronized in different oscillation states in a single array. We measure the phase noise in an 2×2 array as the oscillators change from a state where only two OMOs are oscillating to a state where all four OMOs oscillating, as we observed from the light scattering intensities captured on the IR camera. Figure 5.5b shows the power spectrum of the transmitted light at when the laser is tuned from exciting an optical mode that spans two cavities to an optical mode that spans all four cavities (Fig. 5.2a) while staying at the same optical power. Following the transition, the four OMO oscillation state shows an increase of $\sim$ 3dB in the oscillation signal and $\sim$ 3dB drop in the phase noise. At the same time, all four resonators lights up on the IR camera. This strongly indicates that such transition is caused by the four oscillators being synchronized.

5.7 Conclusion

In conclusion, we demonstrate synchronization in highly integrated arrays of micromechanical oscillators coupled through the optical field. We show the onset of synchronization in the array by tracking the emergence of a single oscillation frequency in the optical power spectrum. Synchronization is further corroborated by our study of the phase noise in the arrays. The reduction of phase noise with oscillator array size and the scalability of our devices could enables low noise frequency and high power integrated frequency sources. Our work paves a path towards large scale monolithically fabricated oscillator networks that have the potential to compete with the performance of bulk resonators and to exhibit rich nonlinear dynamics opening the door to novel metrology, communication and computing techniques.

CHAPTER 6

COUPLING A CARBON NANOTUBE TO A HIGH FINESS OPTICAL MICROCAVITY

6.1 Introduction

Carbon nanotubes (CNTs) are one dimensional strand of carbon atoms [96, 97]. The atoms are arrange such that CNTs are folded cylinders of graphene sheets. These 1d structures possess some of the most exotic properties that are known today. CNTs have the largest tensile strength and are the stiffest material [98] and they also are some of the smallest transistors [99]. However, because the CNTs is tiny (normally a few nm in diameter), it is extremely challenging to make them interacting efficiently with the environment. Even the size of a tightly focus laser spot under a high numerical aperture microscope objective can be hundreds of times larger than a typical CNT. This means that typical measurements of CNT requires long averaging times and the small interaction strength between the CNTs and the measurement tool produce very low signal-to-noise ratio signals forbidding the observation of fast dynamics. Previous measurements of CNTs often relies on drive and detect measurements and long averages [100]. Passive measurements such as detecting the thermal Brownian motion of CNTs has only started recently and have very limited progress [101, 102]

The idea of using an optical cavity is to optically readout the mechanical motion of carbon nanotubes as discussed in chapter 1. Recently, there is emerging interest in coupling CNTs to microwave microstructures [101] and fiber optical cavities to access the mechanical properties of the CNTs [102]. However,

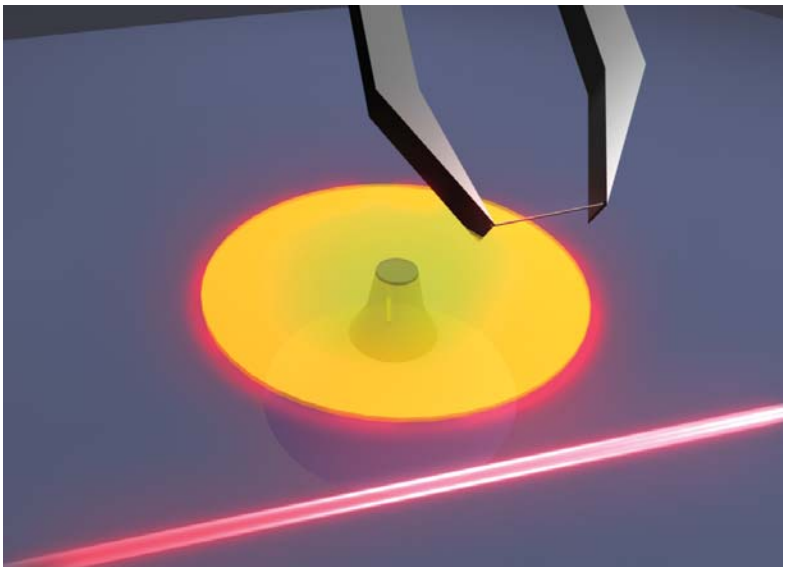

Figure 6.1: **An artistic impression of a pair of gold microtweezers holding a CNT over the evanescent optical field of a microdisk cavity.** The optical cavity is excited by a tapered optical fiber waveguide.

efficiently coupling them to optical fields is challenging since the diameter of a CNT is more than two orders of magnitude smaller than the wavelength of light. Here we demonstrate a novel platform that shows strong interaction between a single CNT and an optical microresonator. This work is done in collaborate with Arthur Barnard and Professor Paul McEuen at Cornell Physics department. We use electrically contacted microtweezers to pick up individual while simultaneously using the tweezer probes to measure the photocurrent response of the nanotube. We choose a free-standing silicon nitride optical disk cavity as it is high quality factor, high finesse, relative small modal volume and easily coupled with light.

We developed electrically contacted microtweezers to pick up individual CNT and place them with nm-scale accuracy near an optical cavity [103]. The optical cavity is designed so that the evanescent optical field propagating out-

side of the cavity can be directly accessed by the CNT while not being perturbed by the microtweezers [6]. This is in stark contrast to the traditional approach of directly integrating CNTs on to the chip using planarized process. The advantage of studying CNTs in a controllable fashion like the microtweezers positioning here is that it allows the construction of a full set of spatial dependent data. This is critical in the understanding of CNT dynamics. Being able to move the CNT into and out of the optical evanescent field enables a direct comparison of the signals with and without the CNT. This allows identification of signals that originates from the CNTs.

6.2 Experimental setup

We designed and build a vacuum chamber (also a cryostat) to accommodate the microtweezers picking up CNTs and tapered fiber optical cavity coupling simultaneously. The project is supported through an instrumentation project by the Kavli Institute for Nanoscience at Cornell, so we often refer this chamber as the Kavli cryostat. The idea is to pick up a CNT from a CNT growth chip and move the microtweezers with the CNT to an optical cavity chip which is mount on the same stage. The vacuum chamber hosts a colder finger cryostat (Janis ST-500) at the center and emerging from the bottom of the vacuum chambe. We attached a cryogenic compatible xyz-piezo sample stage (Attocube ANPx340/LT, ANPz101eXT/LT) on the cold finger which can be cooled down to 10 K. This stage allows the sample to travel up to 20×20 mm in the sample plane and 12 mm vertically out of the plane. The large dynamic range of the stage plays a crucial role in transporting the lifted CNT over to the optical cavity.

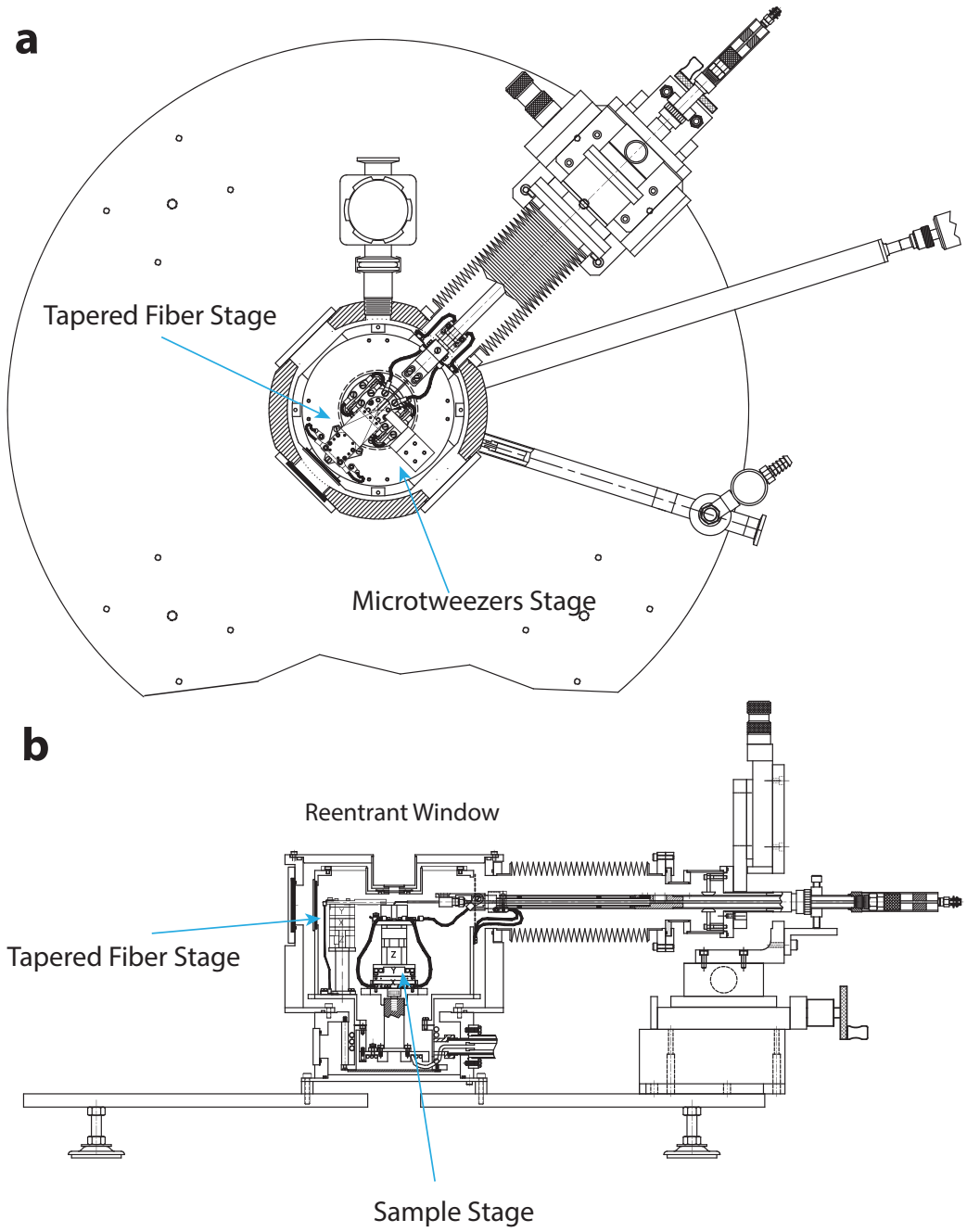

Figure 6.2: **Experimental chamber designed for the CNT optics experiment.**(**a**) Top view of the chamber we designed for picking up CNTs and placing them near a tapered fiber coupled optical cavity. The two sets of xyz piezo stages holding the tapered fiber and the microtweezers are at 90 degrees to each other pointing to the sample holder. (**b**) Cross-section view of the chamber where a re-entrant window is shown. The reentrance at the center of the chamber lid allows short working distance objective to get close to the sample for fine imaging.

Around the sample mount, we installed two xyz-piezo stages at 90 degrees to each other facing the sample mount to hold the tapered optical fiber (with an Attocube ANPx101/RES/LT, ANPz101/RES/LT) and the microtweezers (with a PiezoJena miniTRITOR) respectively. We designed the tapered optical fiber holder to hold a straight taper under tension such that the gap between the cavity and the tapered fiber can be readily controlled (Fig. 6.2).

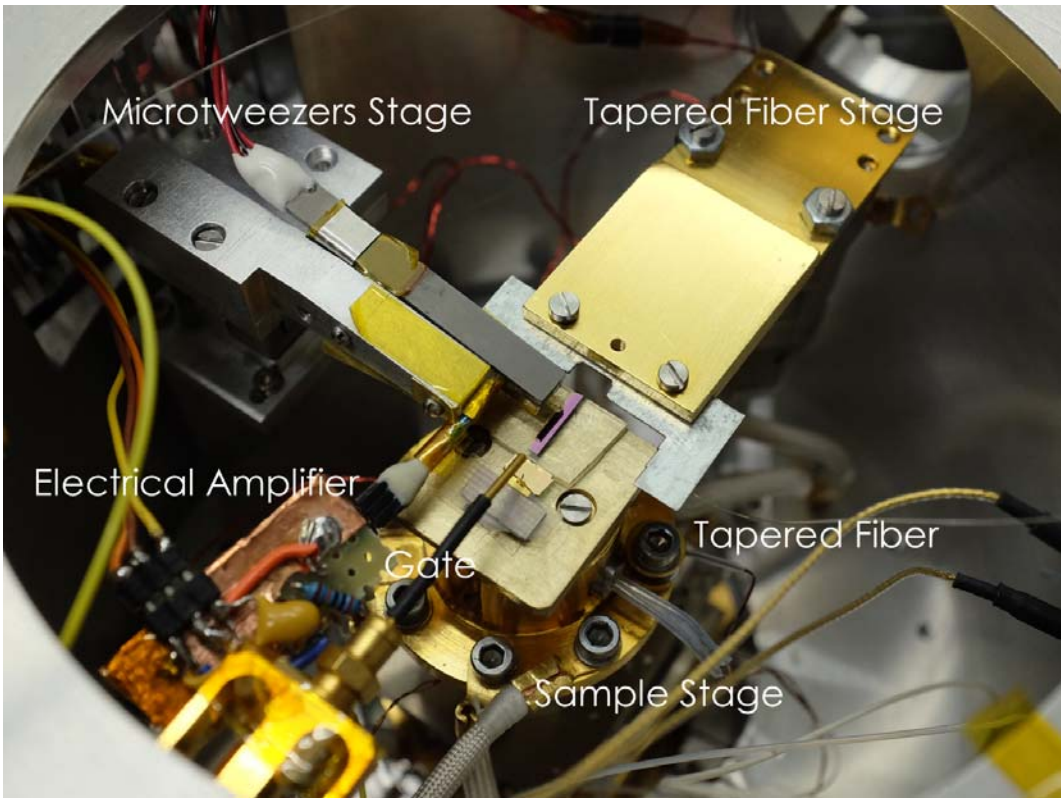

Figure 6.3: **Photo of the Kavli Chamber** A photo showing the inside of the vacuum chamber with the tapered optical fiber, microtweezers, optical cavity chip and CNT growth chip installed.

Besides the high versatility in low-T compatible motion control, optical and electrical feedthrough, the probe station is also designed for high resolution imaging. We design an re-entrant window as shown in figure 6.2 to allow high NA long working distance objectives (Mitutoyo) to be used. High resolution imaging is critical in realizing the fine control for CNT pick-up and positioning.

6.3 Device fabrication

CNTs are grown using chemical vapor deposition (CVD) on a micro-patterned corrugated substrate. The resulting structure consists of flow-aligned CNTs with suspended regions between corrugations. Using two-terminal electrically contacted home-built microtweezers we pick up CNTs, with electrical end-point detection used to determine when a tube spans the tweezer probes. We move the microtweezers above the surface of the growth substrate with piezo stages until electrical conductivity is observed. We then lift-up the microtweezers to free the tube from the substrate. The separation of the microtweezers can be tuned from 5 to 30 μm via piezo actuation, which enables us to buckle the CNT out of plane as well as to tension it, controlling the mechanical, electronic and optical response.

In the course of the experimental development, we continuously optimized the fabrication process to increase the optical quality factor of the cavity. The Si_3N_4 optical cavities are fabricated on standard thermal SiO_2 (thickness $\sim$ 3.5 μm) on Si wafers. A thin layer ($\sim$ 350 nm)of stoichiometric Si_3N_4 is deposited on the wafer using LPCVD technique at 800 C. Individual optical cavities with varying radius (6 – 50 μm) is then patterned using electron beam lithography. We also patterned a thin mechanical tether near the optical cavity to use as a 'parking lot' for the tapered optical fiber. The Van der Waal's force between the tapered fiber and the tether allows the position of the tapered fiber to be continuously fine tuned even when it is positioned very close to the cavity. Without such intervention, snapping due to electrostatic or Van der Waals force between the fiber and the cavity can make fine positioning difficult.

The particular e-beam resist we used for the highest optical quality factor measured is the MaN-2410 resist which is negative tone with a thickness of ~ 1μm. The resist is developed and reflowed at 135 C° for 5 minutes to reduce the side wall roughness at the cost of increased side wall angle. The pattern is then transferred onto the wafer using reactive ion etching with CF_4. Using CF_4 as oppose to C_2F_2 or CHF_3/O_2 aims at reducing fluorocarbon polymerization [104] on the side walls at the cost of increased side wall angle. The resists are then removed by immersing the wafer in a hot piranha (H_2SO_4:H_2O_2) bath at 60 C for 20 minutes. Removing the resist using piranha as opposed to oxygen plasma prevents the stress build up in the Si_3N_4 layer which could cause the disk to deform when suspended. Following the resist removal, we further cleaned the wafer through a standard MOS clean process (10 minutes dilute NH_4OH/H_2O_2 and 10 minutes dilute HCL/H_2O_2 at 75 °C). We then anneal the processed wafer at 1200 C for 2 hours to reduce hydrogen content in the Si_3N_4 film which reduces optical absorption loss [105]. The patterned wafer is then cladded with a 50 nm layer of high temperature oxide (HTO) to prevent contamination of the optical cavity from further processing steps.

The wafer is then diced into 10 × 1.5 mm chips and release in diluted hydrofluoric acid (49% HF:H_2O 6:1) for approximately 30 minutes to undercut the Si_3N_4 disks for about 3 μm. The etching time is chosen such that a symmetric optical mode profile is ensured while still maintaining the Si_3N_4 layer, since HF has a finite etching selectivity (~ 100:1) of SiO_2 to Si_3N_4 . To further enhance the optical quality factors, we perform cycles of heated piranha (120 °C) clean, dilute HF (1:100 to H_2O) dip and H_2 annealing to remove organics compound on the surface, absorptive defects in Si_3N_4 and stripping the native oxide layer [106].

6.4 Basic CNT-optical cavity characterization

6.4.1 Optical cavity response to CNT

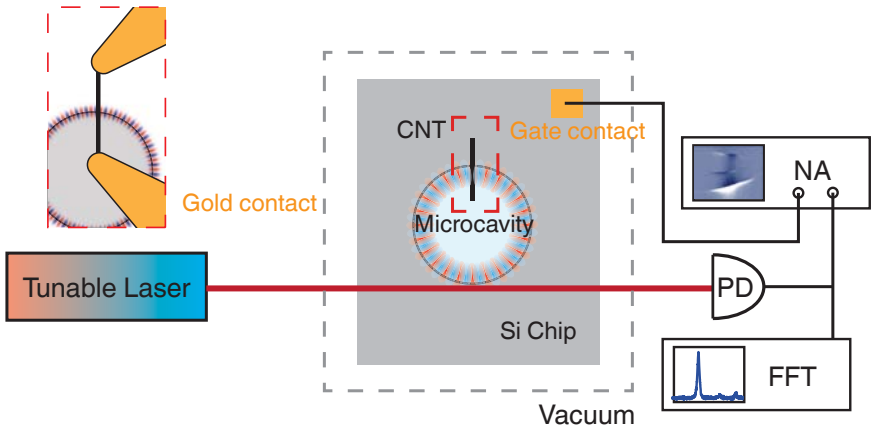

Figure 6.4: **A schematic of the experimental setup for the CNT optical cavity system.** The red dashed box is a close up of the tweezers-cavity region highlighting how the CNT is positioned. The silicon chip hosting the optical cavity is also electrically contacted so the CNT could also be gated. PD: photodiode, NA: network analyzer, FFT: fast Fourier transform.

We position the microtweezers with a CNT held between the two contacts close to the edge of the microdisk to measure the photo-response of the CNT. The two arms of the microtweezers are controlled to have a minimum separation of $\sim 10\mu$m such that when the CNT is positioned over the optical cavity, the metallic tweezers arms do not perturb the optical cavity field. We move the CNT incrementally closer to the top surface of the optical cavity with the tweezers piezo stage (negative Z). At the same time, we constantly sweep the wavelength of the laser around a high finesse resonance of the cavity to monitor the cavity transmission. This method gives us a direct measure of how the presence of a single CNT changes the optical cavity transmission, namely, the

cavity decay rate γ, the cavity extinction T_{ext} and the cavity resonant frequency ω_{cav}.

We experimentally measures two types of CNT-optical cavity interaction. The first type of CNT introduce a combination of dispersive and dissipative effect on the optical cavity transmission. The CNT both refract and scatters the light corresponding to an effective real and imaginary index of refraction [107]. The second type features a predominantly dissipative effect on the optical cavity. The CNT mainly absorb and scatters light whereas the refraction is much less than the other two contributions. Our measurements suggests that the first type of interaction involves a semiconducting CNT where a there is a bandgap at the wavelength of the laser excitation. In the second scenario, the CNT is either metallic or has a very small bandgap. Here the CNT would have a large optical absorption cross section. The strength of the CNT optical interaction is characterized by the dispersive and dissipative optomechanical coupling constant $g_\omega = \frac{\mathrm{d}\omega_{\text{cav}}}{\mathrm{d}x}$ and $g_\gamma = \frac{\mathrm{d}\gamma_{\text{tot}}}{\mathrm{d}x}$. Figure 6.4.1 shows the optical transmission when the two types of CNTs are placed close to and far away from the optical cavity. From the linewidth of the transmission, we extract the optomechanical coupling coefficient for the semiconducting CNT to be $g_\omega \sim 100$ kHz, $g_\gamma \sim 80$ kHz when the CNT is close to the surface of the cavity. For the metallic CNT, the optomechanical coupling coefficient is $g_\gamma \sim 1.2$ MHz.

We measure a strong photocurrent response of the CNT when it is placed in the evanescent field of the microdisk optical cavity [108]. As the laser wavelength is scanned over the optical resonance centered at 1553 nm, both the optical transmission of the microdisk measured through the tapered optical fiber and the photocurrent measured across the CNT show a Lorentzian response,

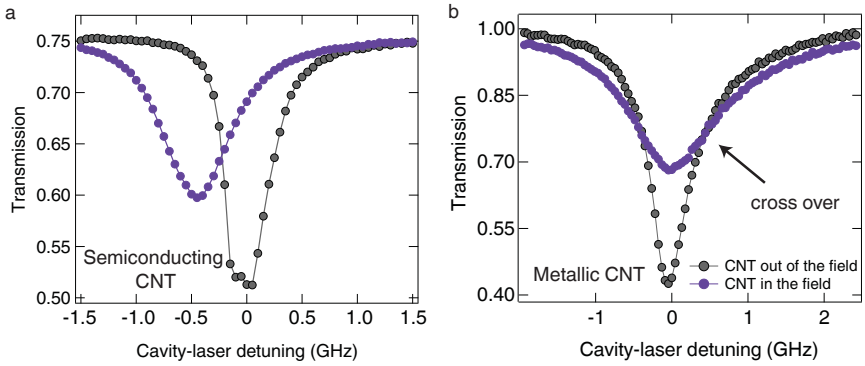

Figure 6.5: **DC measurements with the CNT optical cavity system** (**a**) The optical cavity transmission with a semiconducting CNT close to (purple) and far away (grey) from the evanescent field of the optical cavity. (**b**) The optical cavity transmission for a metallic CNT.

with a loaded optical quality factor of 2×10^5 (Fig 6.4.1a,b). The photocurrent exhibits a linear response to the optical power at an input optical power up to 1 μW (Fig 6.4.1c). The extracted responsively of the device is 38 μA /W which is orders of magnitude larger than when the we illuminate the CNT with a focused light. The responsivity is highly dependent on the position of the CNT relative to the field. When it is moved over a distance of less than 1 μm, the responsivity increases to 0.35 mA/W. We show in the following sections that we could use the photocurrent generated by the CNT to image the standing optical wave inside the optical microcavity.

6.4.2 Optical detection of CNT mechanics

Suspended carbon nanotubes (CNTs) are sensitive to small forces which makes them a prime candidate for force sensors. This same property, combined with their unique photonic and electronic properties makes them attractive for building novel hybrid nanosystems [102, 109]. In previous sections, we investigated

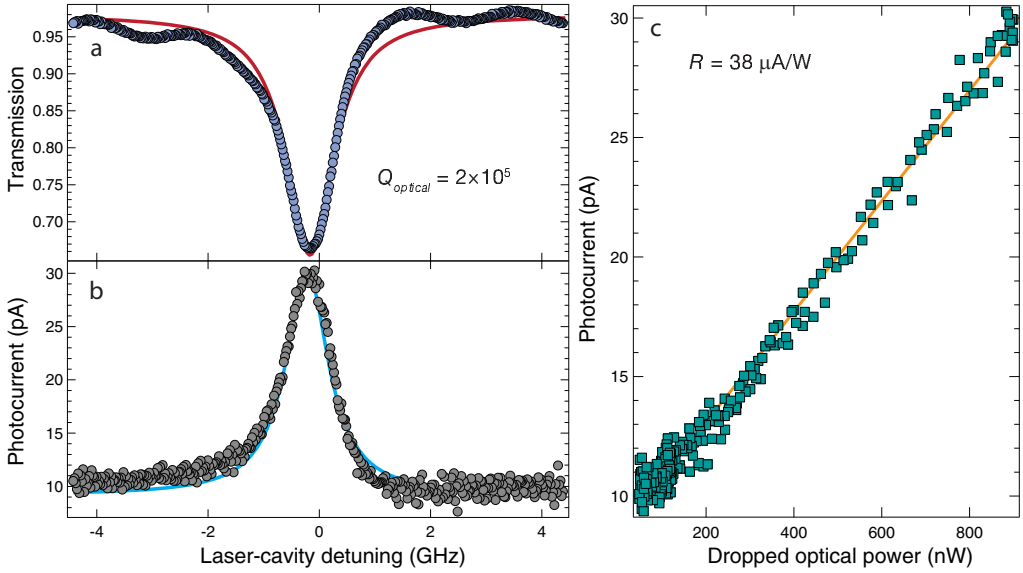

Figure 6.6: **Photocurrent generated from CNT** (**a**)Transmission of the microdisk resonator mode we excite measured through a tapered optical fiber (**b**) Photocurrent response measured across the CNT as the laser is scanned over the optical resonance. (**c**) The photocurrent shows a linear dependence with optical power. The responsivity is 38 μA/W

primarily quasi-static interactions between the CNTs and the optical cavity. In this section, we show that we could take advantage of the low noise and high sensitivity nature of optical field and use it to detect the mechanical motion of the CNTs.

We optically detect the mechanical motion of a CNT driven electrically by a AC voltage applied between the CNT and the gate. The electrical drive is provided by a network analyzer and the optical signal detected on a photodiode is connected to the return port of the network analyzer. We gradually approached the CNT to the optical cavity until strong mechanical resonance peaks are observed on the network analyzer. The gate voltage is then varied as the spatial position of the microtweezers remain fixed. The result (Fig.6.4.2a) shows that the mechanical frequency of a CNT can be tuned by almost a decade with less

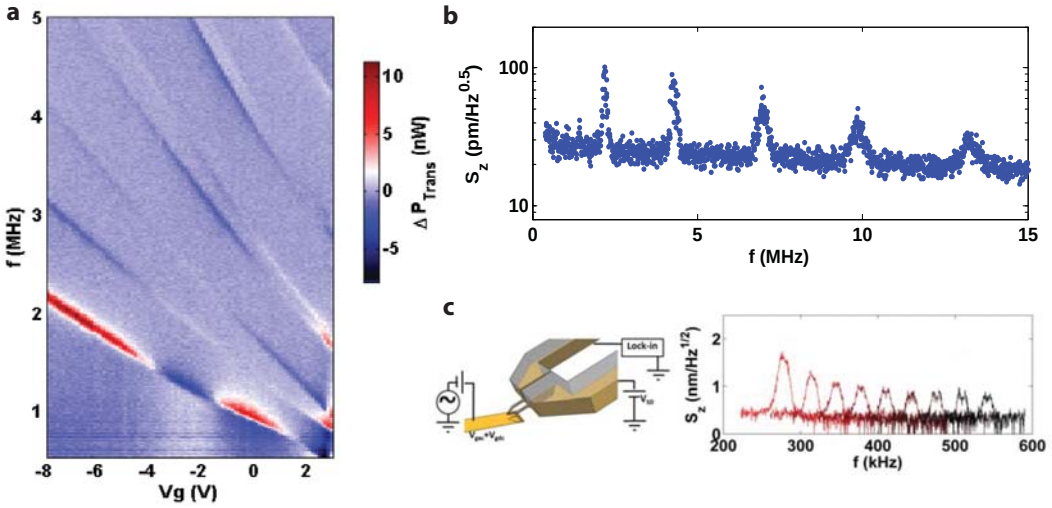

Figure 6.7: **Optical detection of CNT mechanics**(**a**) Electrical drive and optical detection of CNT. V_g is the gate voltage between the tweezers and the CNT. (**b**) Thermal Brownian motion of the CNT measured optically by positioning the CNT inside the evanescent optical field. (**c**) Thermal Brownian motion of the CNT measured electrically under similar conditions. It is evident that the optical detection has a superior sensitivity.

than 10 V change in gate voltage. The fundamental mechanical mode for example, is tuned from < 500 kHz to ~ 2.3 MHz when the gate voltage is changed from 0 V to 8 V. This is in stark contrast to conventional micromechanical oscillators where the tuning range is usually within a few percent. Note that there are several sign flips in the mechanical spectrum as the gate voltage is varied. This is likely a reflection of the locality of the interaction between the optical field and the CNT. As the gate voltage varies, the tension in CNT is changed therefore the shapes of the mechanical modes are also affected. The sign flip reflects the optical field detecting spatially different part of the CNT. We show in the following sections that as we further improve the interaction strength between the optical and mechanical degree of freedom, we could image the mechanical mode shape of a single CNT using optical detection.

We also show that we can detect the thermal Brownian motion of the CNT through the optical cavity. Figure 6.4.2b shows the power spectrum of the optical transmission obtained when the gate AC drive is turned off, i.e. the CNT is only driven by environment thermal noise. There are five mechanical modes readily seen with a noise floor at 30 pm/ $\sqrt{Hz}$. To compare, we also measure the Brownian motion with electrical readout with the gate at similar conditions. The optical readout is an order of magnitude more sensitive than electrical readout in this case.

6.5 CNT-optical cavity dynamics with ultrahigh Q and ultrahigh finesse Si_3N_4 optical cavities

In order for the CNT-optical cavity system to form an efficient feedback system, a high optical quality factor and high finesse cavity is necessary. This is evident from the optomechanical oscillation threshold equation in chapter 2, where the threshold for self-sustaining oscillation is inversely proportional to Q_{opt}^3 and g_{om}^2. Increasing the cavity finesse, i.e. increasing the quality factor while keeping the same optical modal volume, would also increase the optomechanical coupling coefficient g_{om}. We design and fabricated Si_3N_4 micro optical cavities that have intrinsic optical quality factors as high as 5 million and finesse over 40000 using the optimized process we developed and described in section 6.3.

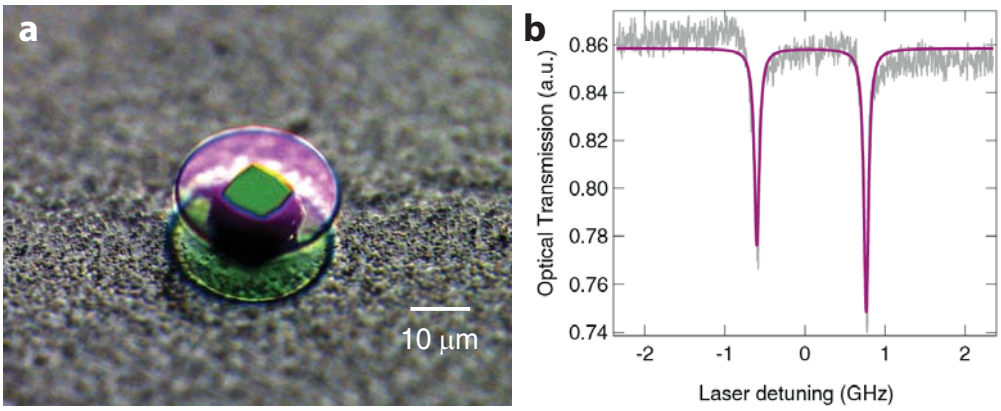

Figure 6.8: **High Q and high finesse Si_3N_4 optical cavity (a)**A photo of the high Q silicon nitride optical cavity taken by a microscope. The sample is positioned to tilt at ~ 45° and is illuminated laterally. **(b)** A typical transmission spectrum of the high Q cavity. The loaded optical quality factor here is $Q_{\text{tot}} \sim 4 \times 10^6$.

6.5.1 Near-field photocurrent imaging of the optical cavity field with a CNT

We can use the CNT as a optical field sensor to image the optical evanescent field by spatially scanning the CNT while monitoring the photocurrent. The high optical quality factor cavity exhibit a fully split resonance doublet because of the inhomogeneities induced scattering between the clockwise and counter-clockwise propagating optical mode 6.5. The split is fully resolved in the high Q cavity because the linewidth $\gamma < 100$MHz of the resonance are much narrower than the previous generation of devices with $\gamma \sim 500$ MHz. The two split modes are two standing waves that are spatially π out of phase with each other as illustrated in figure 6.5.1a. When a CNT is positioned perpendicular to the standing wave, because of its small diameter, it has different spatial overlaps with the two modes resulting in a difference in the detected photocurrent intensity. Figure 6.5.1b shows the optical transmission and the photocurrent generated from

the CNT where the discrepancies on the to modes are evident.

The CNT is then scanned along the standing wave pattern (Y-direction) while we monitoring the optical transmission and photocurrent. While the optical transmission remains relatively unperturbed, the photocurrent signal shows a clear alternating structures when plotted on a colormap as in figure 6.5.1c. We analyze these data by fitting a Lorentzian curve to the photocurrent signal. The peak of the fitted curves as a function of Y is plotted in figure 6.5.1d, where we extracted a periodicity of 400 nm. This is consistent with the periodicity of the standing wave predicted by the optical excitation wavelength of our cavity (1600 nm) and the refractive index of Si_3N_4 ($n_{SiN} = 2$).

6.5.2 Optical near-field imaging of the mechanical modes of a CNT

We elaborated in the previous sections that the localized optical mode could provide spatial information on the mechanical modal profile of the CNTs. With the improved sensitivity, we show that we can scan the optical mode along the CNT to image the mechanical mode shape of the CNT. The setup here is similar to the electrical drive and optical detect scenario. Instead of changing the gate voltage, we move the CNT in the X-direction while monitoring the mechanical mode with a network analyzer. Figure 6.5.2a illustrate the localized interaction of the optical mode with the different mechanical modes of the CNT. As the CNT is moved along in X, the optical mode would have a different response depending on the spatial structure of the mechanical modes.

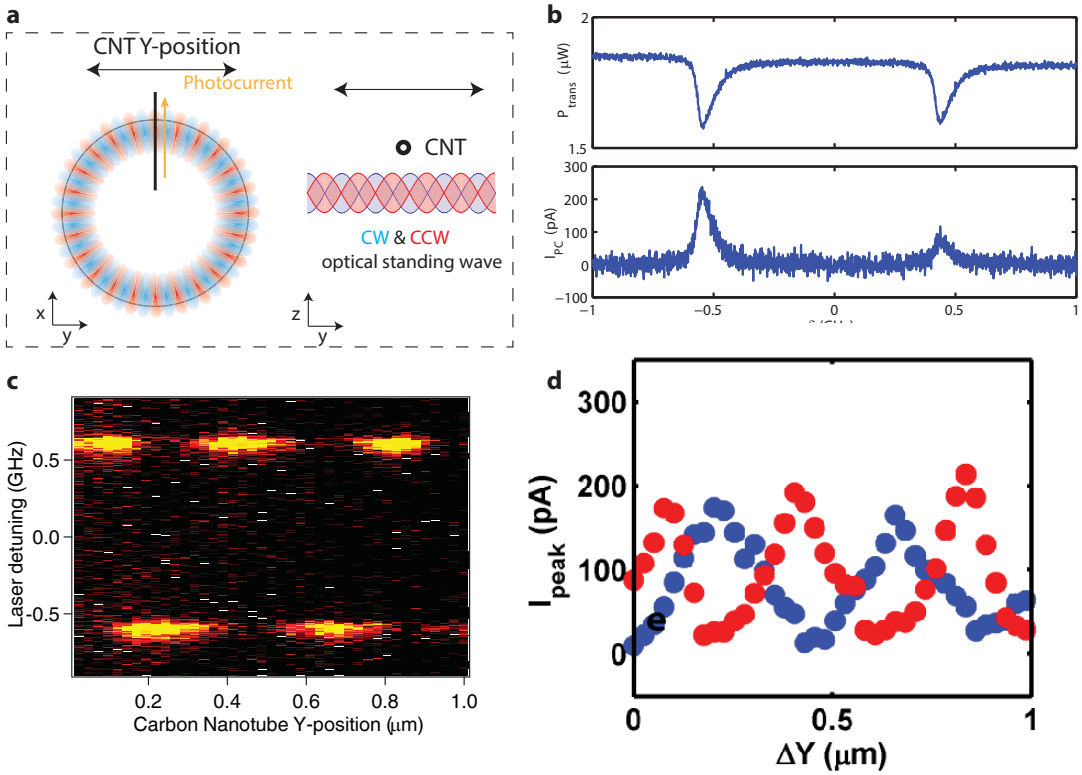

Figure 6.9: **Photocurrent imaging of optical standing wave with CNT** (**a**)A schematic of the standing wave interaction with the CNT. (**b**) The optical transmission spectrum (top) and the photocurrent signal detected in the carbon nanotube. The asymmetry in the photocurrent signal is prominent. (**c**) photocurrent imaging of the optical mode as the CNT is scanned in y-direction. (**d**) The peak intensity of the two standing wave modes as the CNT is moved showing a period of $\sim 0.5\mu m$

Figure 6.5.2b shows the spectrum of the mechanical mode detected by the optical signal. Three distinct mechanical modes with different frequencies are clearly identifiable. The blue and the white color corresponds to a different sign on the signal from the network analyzer. We can see that as the CNT is scanned along X, the high frequency mechanical modes exhibit sign flips where as the lowest frequency mechanical modes merely changes signal strength. This is because as the optical mode is moved from one mechanical antinode to another, there is a π phase change in the mechanical vibration. Therefore the low fre-

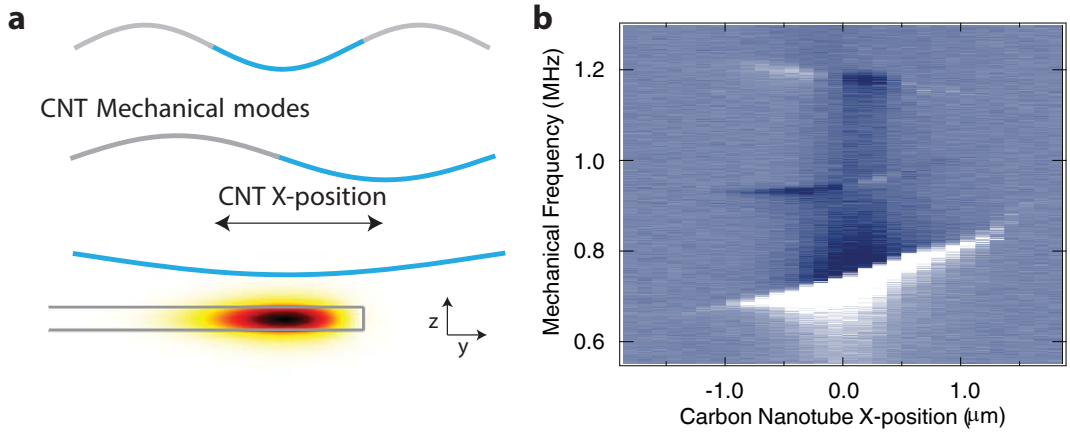

Figure 6.10: **Detecting CNT mechanical mode shapes** (**a**)Concept of detecting mechanical mode shape of a CNT using localized optical mode. (**b**) Electrical driving and optical detection of the mechanical mode revealing phase-flips (blue to white) that corresponds to node in the CNT vibration.

quency mechanical mode has only one antinode in the range of scanning where as the high frequency mechanical mode indeed exhibit phase flips as we illustrate in figure 6.5.2a. This is the first time that the mechanical mode shape of such a small object is imaged using optical method. The slight shift in the frequencies of the three modes is due to the CNT experiencing a changing electrostatic force while moved relative to the optical cavity.

6.5.3 Ultrasensitive detection of CNT thermal Brownian motion

We shown in section 6.4.2 that we can detect the thermal Brownian motion of CNTs using the optical cavity readout. As the cavity quality factor is dramatically improved, we show in this section that we can detect many mechanical modes simultaneously with >30 dB signal to noise ratio (SNR) in the power

spectrum. Traditionally, detecting the mechanical motion of a CNT usually involves advanced techniques such as lock-in detection and have low signal to noise ratio. Because of the sensitive cavity optomechanical interaction, we show that not only we have large spectral SNR, we can also detect the thermal Brownian motion of the CNT in real time as shown in figure 6.5.3b.

We couple 20 μW of light into the optical cavity and tune the laser wavelength

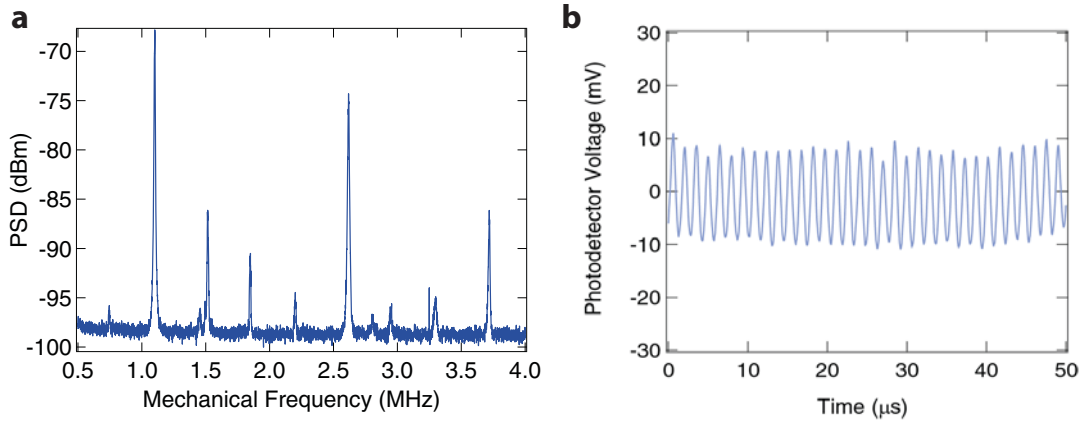

Figure 6.11: **Thermal Brownian motion of a CNT measured with high Q optical cavity** (**a**)Thermal Brownian motion spectrum of a CNT revealing > 30 dB SNR in spectral power. (**b**) The real time signal measured corresponding to the fundamental mechanical mode of a CNT exicted by environmental thermal force.

to be at the center of an optical resonance. The transmitted light is coupled to a photodetector and fed into a digital oscilloscope (Picoscope 5244B) where the real time and FFT spectrum signals are recorded. Figure 6.5.3a shows the optical power spectrum of the transmitted light through the optical cavity. The peaks corresponds to different mechanical modes of the CNT. We extract the mechanical quality factor of the lowest frequency mechanical mode by fitting a Lorentzian curve. The mechanical quality factor we measured appears to be

$Q_m \sim 100$.

Our high SNR real time photodetection reveals a striking feature of the CNT mechanics. Figure 6.5.3b shows a small section of the raw data the oscilloscope collects highlighting real time detection of the CNT thermal Brownian motion. These vibrations are the fundamental flexure mode of the CNT excited by the environmental thermal phonons. If we take a shorter time window to perform the FFT, we can see that the measured mechanical quality factor is much higher than if the data is acquired for a long time. This phenomena is called spectral diffusion and it has been observed in other type of systems [110, 111, 112]. The spectrum is smeared out by the fact that the frequency of the mechanical oscillator is varying at a time-scale that is shorter than the rate the spectrum is recorded. Figure 6.5.3 suggests that the actual quality factor of the CNT oscillator is much higher than if measured with a much slower technique such as using a lock-in detection method.

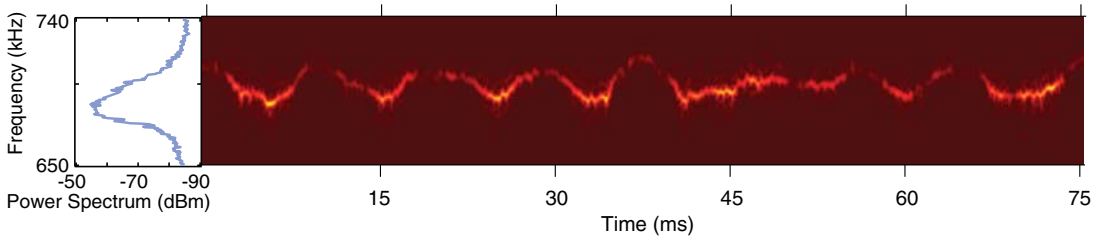

Figure 6.12: **Spectral diffusion of CNT(a)** The power spectrum of the fundamental flexural mode of a CNT taking over 1 second of averaging. **(b)** Same set of data taken with a much shorter FFT time window (1ms) showing that the actual mechanical quality factor is masked by the temporal fluctuation of the mechanical frequency.

6.5.4 CNT cavity optomechanics and nonlinear mechanics

So far, we have demonstrated the optical cavity provide a localized and sensitive means of detecting the CNT mechanical motions. The ultimate goal of this experimental construction is to take the advantage of the low noise and highly efficient optomechanical interaction to control the CNT dynamics. One application is to make a compact self-sustaining CNT optomechanical oscillator. The unique feature of this device is that it could provide decades of frequency tuning range as oppose to only a few percent in traditional MEMS oscillator. We show in this section that we are indeed operating in a regime where the light can affect the mechanical properties of the CNT through optical forces.

We position the CNT as close to the cavity as possible without touching the surface of the cavity. We scan the laser across the standing wave mode that spatially overlaps with the CNT and record the transmission on the FFT spectrum analyzer. At $P_{\text{in}} = 20 \sim \mu$W, we observe both a spring effect and an amplification effect. Figure 6.5.4 shows the linewidth and center frequency for the fundamental mechanical mode of a CNT as a function of laser wavelength ω_{L}. As the laser is tuned into the optical resonance, the mechanical mode of the CNT stiffens and the linewidth reduces. Note that the measure mechanical quality factor improved to a saturation value of Q_m ~300 from Q_m ~110. The actual mechanical linedwidth could be much narrower as our previous analysis shown due to spectral diffusion. It is likely that the amplification and spring effect is due to photothermal effect as the almost purely dissipative optomechanical coupling does not provide a coherent feedback force [113].

Finally, we show that we could excite and measure the nonlinear dynamics of the CNT by increasing the interaction strength of the CNT and the optical

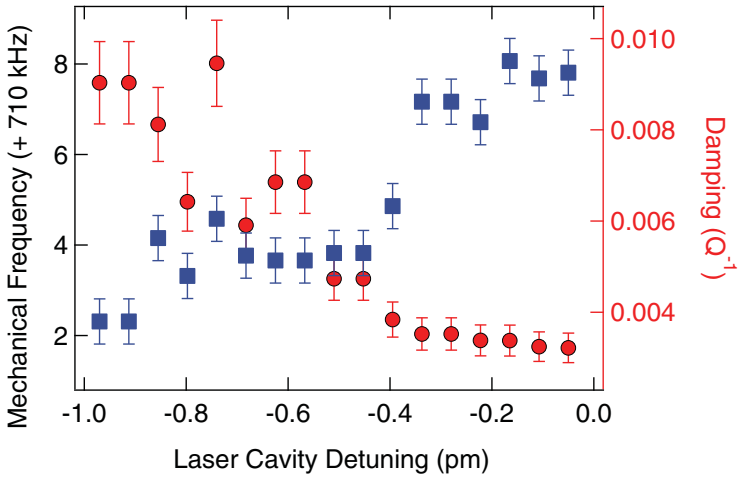

Figure 6.13: **Optomechanical effect in CNT resonators** Spring effect and amplification of the mechanical vibration due to optical forces. As the laser in tuned into the cavity resonance, the mechanical mode of the CNT stiffens and the linewidth improves as the laser drives the cavity stronger.

cavity. We incrementally step the CNT close to the optical cavity with the laser tuned into the optical resonance at large optical input power $P_{\text{in}} = 20 \sim \mu$W. As the CNT is brought closer to the cavity, the optical evanescent field interacts stronger with the CNT through improving the optomechanical interaction strength g_κ. We observe that the CNT mechanical spectrum grows and also higher order harmonics start to appear. We also observe that in the time domain, when a CNT is driven strongly, period doubling could occur. This is possibly a result of the Duffing nonlinearity in the CNT when it vibrates in large amplitude where the mechanical motion is coupled to the spring constant through tension in the CNT [114].

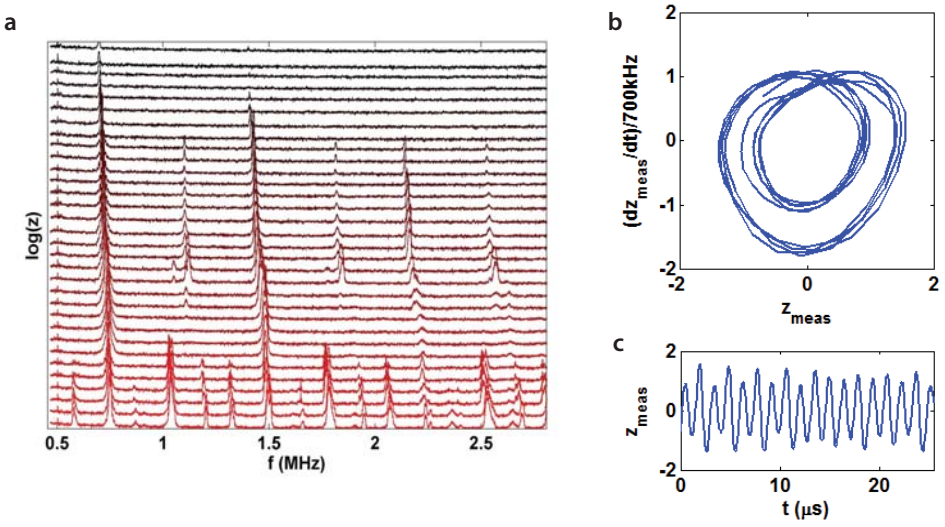

Figure 6.14: **Nonlinear dynamics with CNT** (**a**) The spectrum of a CNT shows signs of period doubling and tripling as the CNT is driven stronger and stronger through approaching the optical cavity. (**b**) Real time trace of a CNT when driven strongly shows period doubling behaviour

6.6 Conclusion

We demonstrate a novel and versatile platform for ultrasensitive detection of CNTs, a string of only a few nm in diameter, using optical microdisk resonators. We devised electrically conductive microtweezers to achieve nm precision in position a suspended CNT over a high Q Si_3N_4 optical cavity. We showed that we could measure the mechanical vibration of the CNT in real time and even control the mechanics of the CNT through optomechanical interactions. The ultrahigh CNT displacement sensitivity would allow the CNT to be used as an ultrasensitive mass and force sensor. The control over the dynamics of the CNT could enable measuring very interactions, for example a CNT interacting with a single spin, in real time. Furthermore, studying the real time dynamics of CNTs may shed light into the fundamental dissipation mechanism that ultimately lim-

its the quality factor of CNT oscillators [115].

CHAPTER 7

CONCLUSION AND OUTLOOK

We explored in this thesis the interaction of many optomechanical systems and a unique system where a high quality optical microscale resonator is coupled to a nanoscale carbon nanotube mechanical resonator.

Synchronization in a large array of integrated micromechanical resonators could be used for low noise frequency sources. Through low loss optical fibers, mechanical resonators could be synchronized even when they are very far apart. The amazing phenomena of synchronization in a large coupled system could be considered merely as a 'ground state' of a coupled nonlinear system. As the coupled system grow in size and complexity, one could imagine that more and more intricate high energy stable states could appear. The importance of complex networks has long been realized. For example, intelligence emerge in a vast complex network of simple neurons. Our work shows a scalable platform that one could combine optomechanics with existing technologies in nanophotonics such as waveguiding, switching and phase shifting and even electronic circuits. Very recently, we demonstrated that we could optically tune suspended cavities through integrated heaters that overhangs the optical cavity while not perturbing the optical field. One concept for a future device would be large optical coupled resonator arrays controlled through arrays of metal heaters wired to a circuit control board to demonstrate controllable synchronization and oscillation state switching.

Our technology of ultrasensitive displacement sensing of a carbon nanotube with an optical microcavity is mature for further exploration. Examples include atomic level mass sensing, near-field scanning optical microscopy and the more

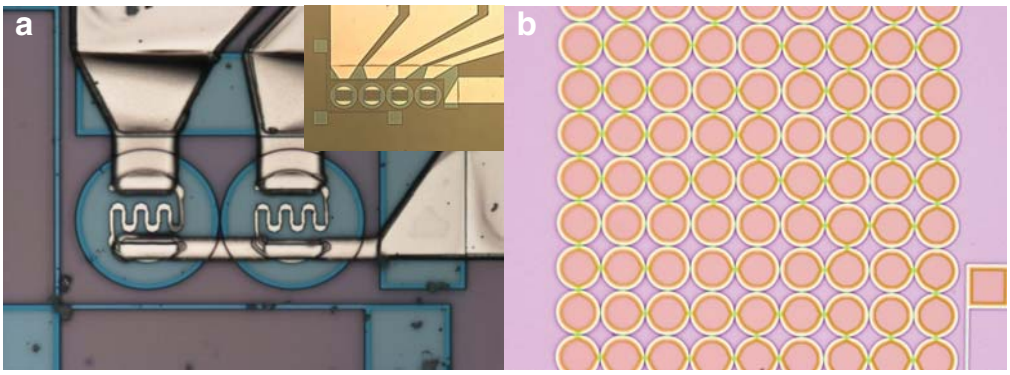

Figure 7.1: **Large scale and tunable optomechanical oscillator arrays**. (**a**) Recent effort on integrating suspended metal heaters for thermo-optic tuning of free-standing optomechanical structures (**b**) Large optomechanical oscillator arrays fabricated on a Si_3N_4 substrate. Combining thermo-optic tuning and the large scale array fabrication could put these devices into full operation.

fundamental aspect of CNT properties such as mechanical dissipation mechanisms, strongly coupled exitons and polaritons and spin coupled to mechanical vibrations. The optical cavity could also be optimized for even higher coupling efficiency, such as using nanobeam photonic crystal cavities.

Our work serves an initial exploration of the new dynamics emerge out of several well understood optomechanical resonators and the unique properties of a special mechanical oscillator coupled to an optical microcavity. A further speculation is that these 'coupled' technologies can be integrated together. The required level of scaling and sensitivity would be possible due to the low loss and low noise of light. It is possible to form a even large networks of oscillators and sensors enabling a new paradigm of devices.

BIBLIOGRAPHY

[1] H. G. Craighead. Nanoelectromechanical Systems. *Science*, 290(5496):1532–1535, November 2000.

[2] M. Lipson. Guiding, modulating, and emitting light on Silicon-challenges and opportunities. *Journal of Lightwave Technology*, 23(12):4222–4238, December 2005.

[3] Lorenzo Pavesi and David J. Lockwood. *Silicon Photonics*. Springer Science & Business Media, March 2004.

[4] Markus Aspelmeyer, Tobias J. Kippenberg, and Florian Marquardt. Cavity optomechanics. *Rev. Mod. Phys.*, 86(4):1391–1452, December 2014.

[5] V. B. Braginsky and A. B. Manukin. Measurement of weak forces in physics experiments. January 1977.

[6] G. Anetsberger, O. Arcizet, Q. P. Unterreithmeier, R. Rivire, A. Schliesser, E. M. Weig, J. P. Kotthaus, and T. J. Kippenberg. Near-field cavity optomechanics with nanomechanical oscillators. *Nat Phys*, 5(12):909–914, December 2009.

[7] Carsten Schmidt. *Mode dynamics in coupled disk optical microresonators*. Jena, 2013.

[8] Hermann A Haus. *Waves and fields in optoelectronics*. Prentice-Hall, Englewood Cliffs, NJ, 1984.

[9] SM Spillane, TJ Kippenberg, OJ Painter, and KJ Vahala. Ideality in a fiber-taper-coupled microresonator system for application to cavity quantum electrodynamics. *Physical Review Letters*, 91(4):043902, July 2003.

[10] E. Gavartin, P. Verlot, and T. J. Kippenberg. A hybrid on-chip optomechanical transducer for ultrasensitive force measurements. *Nat Nano*, 7(8):509–514, August 2012.

[11] Jasper Chan, T. P. Mayer Alegre, Amir H. Safavi-Naeini, Jeff T. Hill, Alex Krause, Simon Grblacher, Markus Aspelmeyer, and Oskar Painter. Laser cooling of a nanomechanical oscillator into its quantum ground state. *Nature*, 478(7367):89–92, October 2011.

[12] E. Verhagen, S. Delglise, S. Weis, A. Schliesser, and T. J. Kippenberg. Quantum-coherent coupling of a mechanical oscillator to an optical cavity mode. *Nature*, 482(7383):63–67, February 2012.

[13] Florian Marquardt, J. G. E. Harris, and S. M. Girvin. Dynamical Multistability Induced by Radiation Pressure in High-Finesse Micromechanical Optical Cavities. *Phys. Rev. Lett.*, 96(10):103901, March 2006.

[14] M. Poot, K. Y. Fong, M. Bagheri, W. H. P. Pernice, and H. X. Tang. Back-action limits on self-sustained optomechanical oscillations. *Phys. Rev. A*, 86(5):053826, November 2012.

[15] Mian Zhang, Gustavo S. Wiederhecker, Sasikanth Manipatruni, Arthur Barnard, Paul McEuen, and Michal Lipson. Synchronization of micromechanical oscillators using light. *Phys. Rev. Lett.*, 109:233906, Dec 2012.

[16] Siddharth Tallur and Sunil A Bhave. A Silicon Electromechanical Photodetector. *Nano Letters*, 13(6):2760–2765, June 2013.

[17] K L Ekinci and M L Roukes. Nanoelectromechanical systems. *Review of Scientific Instruments*, 76(6):061101, 2005.

[18] Kerry J Vahala. Back-action limit of linewidth in an optomechanical oscillator. *Physical Review A*, 2008.

[19] Douglas M Photiadis and John A Judge. Attachment losses of high Q oscillators. *APL*, 85(3):482–484, 2004.

[20] Ron Lifshitz. Phonon-mediated dissipation in micro- and nanomechanical systems. *Physica B: Condensed Matter*, 316-317:397–399, May 2002.

[21] Garrett D Cole, Ignacio Wilson-Rae, Katharina Werbach, Michael R Vanner, and Markus Aspelmeyer. Phonon-tunnelling dissipation in mechanical resonators. *Nature Communications*, 2:231, March 2011.

[22] Ron Lifshitz and M Roukes. Thermoelastic damping in micro- and nanomechanical systems. *Physical Review B*, 61(8):5600–5609, February 2000.

[23] O Arcizet, R Rivière, A Schliesser, G Anetsberger, and Tobias J Kippen-

berg. Cryogenic properties of optomechanical silica microcavities. *Physical Review A*, 80(2):021803, August 2009.

[24] Feng-Chia Hsu, Jin-Chen Hsu, Tsun-Che Huang, Chin-Hung Wang, and Pin Chang. Reducing support loss in micromechanical ring resonators using phononic band-gap structures. *Journal of Physics D: Applied Physics*, 44(37):375101, August 2011.

[25] Matt Eichenfield, Jasper Chan, Ryan M Camacho, Kerry J Vahala, and Oskar J Painter. Optomechanical crystals. *Nature*, 462, 2009.

[26] Scott S Verbridge, Jeevak M Parpia, Robert B Reichenbach, Leon M Bellan, and H G Craighead. High quality factor resonance at room temperature with nanostrings under high tensile stress. *Journal of Applied Physics*, 99(12):124304, 2006.

[27] Gustavo S. Wiederhecker, Long Chen, Alexander Gondarenko, and Michal Lipson. Controlling photonic structures using optical forces. *Nature*, 462(7273):633–U103, December 2009.

[28] Jessie Rosenberg, Qiang Lin, and Oskar J Painter. Static and dynamic wavelength routing via the gradient optical force. *Nat Photon*, 3(8):478–483, July 2009.

[29] Tobias J Kippenberg and Kerry J Vahala. Cavity Optomechanics: Back-Action at the Mesoscale. *Science*, 321(5893):1172–1176, August 2008.

[30] Yuxin Sun and Hironori Tohmyoh. Thermoelastic damping of the axisymmetric vibration of circular plate resonators. *Journal of Sound and Vibration*, 319(1-2):392–405, January 2009.

[31] Yuxin Sun and Masumi Saka. Thermoelastic damping in micro-scale circular plate resonators. *Journal of Sound and Vibration*, 329(3):328–337, February 2010.

[32] K Y Yasumura, T D Stowe, E M Chow, T Pfafman, T W Kenny, B C Stipe, and D Rugar. Quality factors in micron- and submicron-thick cantilevers. *Journal of Microelectromechanical Systems*, 9(1):117–125, 2000.

[33] Christiaan Huygens. *Horologium oscillatorium: sive, De motu pendulorum ad horologia aptato demostrationes geometricae*. F. Muguet, 1673.

[34] Steven H Strogatz. *Sync: the emerging science of spontaneous order*. Hyperion, New York, 1st ed edition, 2003.

[35] Igor Belykh, Enno de Lange, and Martin Hasler. Synchronization of Bursting Neurons: What Matters in the Network Topology. *Phys. Rev. Lett.*, 94(18):188101, May 2005.

[36] Adilson E. Motter, Seth A. Myers, Marian Anghel, and Takashi Nishikawa. Spontaneous synchrony in power-grid networks. *Nat Phys*, 9(3):191–197, March 2013.

[37] I. Mahboob and H. Yamaguchi. Bit storage and bit flip operations in an electromechanical oscillator. *Nature Nanotechnology*, 3(5):275–279, May 2008.

[38] Mahmood Bagheri, Menno Poot, Mo Li, Wolfram P H Pernice, and Hong X Tang. Dynamic manipulation of nanomechanical resonators in the high-amplitude regime and non-volatile mechanical memory operation. *Nature Nanotechnology*, Oct 2011.

[39] F.C. Hoppensteadt and E.M. Izhikevich. Pattern recognition via synchronization in phase-locked loop neural networks. *IEEE Transactions on Neural Networks*, 11(3):734–738, May 2000.

[40] S. Kaka, M. R. Pufall, W. H. Rippard, T. J. Silva, S. E. Russek, and J. A. Katine. Mutual phase-locking of microwave spin torque nano-oscillators. *Nature*, 437(7057):389–392, 2005.

[41] FB Mancoff, ND Rizzo, BN Engel, and S Tehrani. Phase-locking in double-point-contact spin-transfer devices. *Nature*, 437(7057):393–395, September 2005.

[42] Seung-Bo Shim, Matthias Imboden, and Pritiraj Mohanty. Synchronized oscillation in coupled nanomechanical oscillators. *Science*, 316(5821):95–99, April 2007.

[43] M Zalalutdinov, KL Aubin, M Pandey, AT Zehnder, RH Rand, HG Craighead, JM Parpia, and BH Houston. Frequency entrainment for micromechanical oscillator. *Applied Physics Letters*, 83(16):3281–3283, October 2003.

[44] Duncan J. Watts and Steven H. Strogatz. Collective dynamics of small-world networks. *Nature*, 393(6684):440–442, 1998. 10.1038/30918.

[45] Georg Heinrich, Max Ludwig, Jiang Qian, Bjoern Kubala, and Florian Marquardt. Collective dynamics in optomechanical arrays. *Physical Review Letters*, 107(4):043603, July 2011.

[46] F Marquardt, JGE Harris, and SM Girvin. Dynamical multistability induced by radiation pressure in high-finesse micromechanical optical cavities. *Physical Review Letters*, 96(10):103901, March 2006.

[47] Florian Marquardt. Quantum mechanics: The gentle cooling touch of light. *Nature*, 478(7367):47–8, Oct 2011.

[48] J L Arlett, E B Myers, and M L Roukes. Comparative advantages of mechanical biosensors. *Nature Nanotechnology*, 6(4):203–15, Apr 2011.

[49] C. A. Holmes, C. P. Meaney, and G. J. Milburn. Synchronization of many nanomechanical resonators coupled via a common cavity field. *Phys. Rev. E*, 85:066203, Jun 2012.

[50] M Cross, A Zumdieck, Ron Lifshitz, and J Rogers. Synchronization by Nonlinear Frequency Pulling. *PRL*, 93(22):224101, November 2004.

[51] M. Hossein-Zadeh and K.J. Vahala. Observation of injection locking in an optomechanical rf oscillator. *Applied Physics Letters*, 93(19):191115–191115–3, 2008.

[52] Francesco Massel, Sung Un Cho, Juha-Matti Pirkkalainen, Pertti J Hakonen, Tero T Heikkilä, and Mika A Sillanpää. Multimode circuit optomechanics near the quantum limit. *Nature Communications*, 3:987–, August 2012.

[53] Max Ludwig and Florian Marquardt. Quantum many-body dynamics in optomechanical arrays. *arXiv e-prints: 1208.0327*, August 2012.

[54] A Tomadin, S Diehl, M D Lukin, P Rabl, and P Zoller. Reservoir engineering and dynamical phase transitions in optomechanical arrays. *arXiv e-prints: 1206.6321*, June 2012.

[55] ML Gorodetsky, AD Pryamikov, and VS Ilchenko. Rayleigh scattering in high-q microspheres. *Journal of the Optical Society of America B-Optical Physics*, 17(6):1051–1057, June 2000.

[56] TJ Kippenberg and KJ Vahala. Cavity opto-mechanics. *Optics Express*, 15(25):17172–17205, 2007.

[57] C. K. Law. Interaction between a moving mirror and radiation pressure: A hamiltonian formulation. *Phys. Rev. A*, 51(3):2537–2541, Mar 1995.

[58] Matt Eichenfield, Ryan Camacho, Jasper Chan, Kerry J. Vahala, and Oskar Painter. A picogram- and nanometre-scale photonic-crystal optomechanical cavity. *Nature*, 459(7246):550–555, 05 2009.

[59] T. Carmon, H. Rokhsari, L. Yang, T. J. Kippenberg, and K. J. Vahala. Temporal behavior of radiation-pressure-induced vibrations of an optical microcavity phonon mode. *Physical Review Letters*, 94(22):223902, 2005.

[60] Ivan S. Grudinin, Hansuek Lee, O. Painter, and Kerry J. Vahala. Phonon laser action in a tunable two-level system. *Physical Review Letters*, 104(8):083901, February 2010.

[61] Gustavo S. Wiederhecker, Sasikanth Manipatruni, Sunwoo Lee, and Michal Lipson. Broadband tuning of optomechanical cavities. *Optics Express*, 19(3):2782–2790, January 2011.

[62] Matt Eichenfield, Jasper Chan, Amir H. Safavi-Naeini, Kerry J. Vahala, and Oskar Painter. Modeling dispersive coupling and losses of localized optical and mechanical modes in optomechanical crystals. *Optics Express*, 17(22):20078–20098, October 2009.

[63] SG Johnson, M Ibanescu, MA Skorobogatiy, O Weisberg, JD Joannopoulos, and Y Fink. Perturbation theory for maxwell's equations with shifting material boundaries. *Physical Review E*, 65(6):066611, June 2002.

[64] RE Mirollo and SH Strogatz. Amplitude death in an array of limit-cycle oscillators. *Journal of Statistical Physics*, 60(1-2):245–262, July 1990.

[65] PR Saulson. Thermal noise in mechanical experiments. *Physical Review D*, 42(8):2437–2445, October 1990.

[66] B. Hauschildt, N. B. Janson, A. Balanov, and E. Schoell. Noise-induced cooperative dynamics and its control in coupled neuron models. *Physical Review E*, 74(5):051906, November 2006.

[67] SV Hoeye, A Suarez, and S Sancho. Analysis of noise effects on the nonlinear dynamics of synchronized oscillators. *Ieee Microwave and Wireless Components Letters*, 11(9):376–378, September 2001.

[68] Kevin Burrage, Pamela Burrage, Desmond J. Higham, Peter E. Kloeden, and Eckhard Platen. Comment on "numerical methods for stochastic differential equations". *Physical Review E*, 74(6):068701, December 2006.

[69] Peter E Kloeden and Eckhard Platen. *Numerical solution of stochastic differential equations*, volume 23. Springer, Berlin, corr. 3rd print edition, 1999.

[70] J Wilkie. Numerical methods for stochastic differential equations. *Physical Review E*, 70(1):017701, July 2004.

[71] Charles S Peskin. *Mathematical aspects of heart physiology*. Courant Institute of Mathematical Sciences, New York University, New York, 1975.

[72] Steven M. Reppert and David R. Weaver. Coordination of circadian timing in mammals. *Nature*, 418(6901):935–941, August 2002.

[73] S. H. Strogatz. Exploring complex networks. *Nature*, 410(6825):268–276, March 2001.

[74] A.B. Shkarin, N.E. Flowers-Jacobs, S.W. Hoch, A.D. Kashkanova, C. Deutsch, J. Reichel, and J.G.E. Harris. Optically Mediated Hybridization between Two Mechanical Modes. *Phys. Rev. Lett.*, 112(1):013602, January 2014.

[75] T. P. Purdy, D. W. C. Brooks, T. Botter, N. Brahms, Z.-Y. Ma, and D. M. Stamper-Kurn. Tunable Cavity Optomechanics with Ultracold Atoms. *Phys. Rev. Lett.*, 105(13):133602, September 2010.

[76] T. Herr, V. Brasch, J. D. Jost, C. Y. Wang, N. M. Kondratiev, M. L. Gorodetsky, and T. J. Kippenberg. Temporal solitons in optical microresonators. *Nat Photon*, 8(2):145–152, February 2014.

[77] I. Bargatin, E. B. Myers, J. S. Aldridge, C. Marcoux, P. Brianceau, L. Duraffourg, E. Colinet, S. Hentz, P. Andreucci, and M. L. Roukes. Large-Scale Integration of Nanoelectromechanical Systems for Gas Sensing Applications. *Nano Lett.*, 12(3):1269–1274, March 2012.

[78] S. Tallur, S. Sridaran, S.A. Bhave, and T. Carmon. Phase noise modeling of

opto-mechanical oscillators. In *Frequency Control Symposium (FCS), 2010 IEEE International*, pages 268–272, June 2010.

[79] H.C. Chang, X. Cao, U.K. Mishra, and R.A. York. Phase noise in coupled oscillators: Theory and experiment. *Microwave Theory and Techniques, IEEE Transactions on*, 45(5):604–615, 1997.

[80] T.H. Lee and A. Hajimiri. Oscillator phase noise: a tutorial. *IEEE Journal of Solid-State Circuits*, 35(3):326–336, March 2000.

[81] Arkady Pikovsky, Michael Rosenblum, and Jrgen Kurths. *Synchronization: A Universal Concept in Nonlinear Sciences*. Cambridge University Press, April 2003.

[82] G. Len Aveleyra, C. A. Holmes, and G. J. Milburn. Synchronization in a mechanical resonator array coupled quadratically to a common electromagnetic field mode. *Phys. Rev. E*, 89(6):062912, June 2014.

[83] Deepak K. Agrawal, Jim Woodhouse, and Ashwin A. Seshia. Observation of Locked Phase Dynamics and Enhanced Frequency Stability in Synchronized Micromechanical Oscillators. *Phys. Rev. Lett.*, 111(8):084101, August 2013.

[84] Matthew H. Matheny, Matt Grau, Luis G. Villanueva, Rassul B. Karabalin, M.C. Cross, and Michael L. Roukes. Phase Synchronization of Two Anharmonic Nanomechanical Oscillators. *Phys. Rev. Lett.*, 112(1):014101, January 2014.

[85] Mahmood Bagheri, Menno Poot, Linran Fan, Florian Marquardt, and Hong X. Tang. Photonic cavity synchronization of nanomechanical oscillators. *Phys. Rev. Lett.*, 111:213902, Nov 2013.

[86] Qiang Lin, Jessie Rosenberg, Darrick Chang, Ryan Camacho, Matt Eichenfield, Kerry J Vahala, and Oskar J Painter. Coherent mixing of mechanical excitations in nano-optomechanical structures. *arXiv*, physics.optics, 2009.

[87] Mian Zhang, Gustavo Luiz, Shreyas Shah, Gustavo Wiederhecker, and Michal Lipson. Eliminating anchor loss in optomechanical resonators using elastic wave interference. *Applied Physics Letters*, 105(5):051904, August 2014.

[88] Heng-Chia Chang, Xudong Cao, Umesh K. Mishra, and R.A. York. Phase noise in coupled oscillators: theory and experiment. *IEEE Transactions on Microwave Theory and Techniques*, 45(5):604–615, May 1997.

[89] Mani Hossein-Zadeh, Hossein Rokhsari, Ali Hajimiri, and Kerry J. Vahala. Characterization of a radiation-pressure-driven micromechanical oscillator. *Phys. Rev. A*, 74(2):023813, August 2006.

[90] King Yan Fong, Menno Poot, Xu Han, and Hong X. Tang. Phase noise of self-sustained optomechanical oscillators. *Phys. Rev. A*, 90(2):023825, August 2014.

[91] D.B. Leeson. A simple model of feedback oscillator noise spectrum. *Proceedings of the IEEE*, 54(2):329–330, February 1966.

[92] Yoshitomo Okawachi, Kasturi Saha, Jacob S. Levy, Y. Henry Wen, Michal Lipson, and Alexander L. Gaeta. Octave-spanning frequency comb generation in a silicon nitride chip. *Optics Letters*, 36(17):3398, September 2011.

[93] Pascal DelHaye, Katja Beha, Scott B. Papp, and Scott A. Diddams. Self-Injection Locking and Phase-Locked States in Microresonator-Based Optical Frequency Combs. *Phys. Rev. Lett.*, 112(4):043905, January 2014.

[94] S. Tallur, S. Sridaran, S.A. Bhave, and T. Carmon. Phase noise modeling of opto-mechanical oscillators. In *Frequency Control Symposium (FCS), 2010 IEEE International*, pages 268–272, June 2010.

[95] Mian Zhang, Gustavo S. Wiederhecker, Sasikanth Manipatruni, Arthur Barnard, Paul McEuen, and Michal Lipson. Synchronization of Micromechanical Oscillators Using Light. *Phys. Rev. Lett.*, 109(23):233906, December 2012.

[96] Ray H. Baughman, Anvar A. Zakhidov, and Walt A. de Heer. Carbon Nanotubes–the Route Toward Applications. *Science*, 297(5582):787–792, August 2002.

[97] Sumio Iijima and Toshinari Ichihashi. Single-shell carbon nanotubes of 1-nm diameter. *Nature*, 363(6430):603–605, June 1993.

[98] E. D. Minot, Yuval Yaish, Vera Sazonova, Ji-Yong Park, Markus Brink, and Paul L. McEuen. Tuning carbon nanotube band gaps with strain. *Physical Review Letters*, 90(15):156401, 2003. PRL.

[99] Phaedon Avouris, Marcus Freitag, and Vasili Perebeinos. Carbon-nanotube photonics and optoelectronics. *Nat Photon*, 2(6):341–350, 2008.

[100] Vera Sazonova, Yuval Yaish, Hande stnel, David Roundy, Toms A. Arias, and Paul L. McEuen. A tunable carbon nanotube electromechanical oscillator. *Nature*, 431(7006):284–287, September 2004.

[101] B. H. Schneider, S. Etaki, H. S. J. van der Zant, and G. A. Steele. Coupling carbon nanotube mechanics to a superconducting circuit. *Sci. Rep.*, 2, 2012. 10.1038/srep00599.

[102] S. Stapfner, L. Ost, D. Hunger, EM Weig, J. Reichel, and I. Favero. Cavity-enhanced optical detection of carbon nanotube brownian motion. *arXiv preprint arXiv:1211.1608*, 2012.

[103] Arthur Barnard, Mian Zhang, Michal Lipson, and Paul McEuen. Micro-tweezers for studying vibrating carbon nanotubes. page 37003, March 2014.

[104] W. W. Stoffels, E. Stoffels, and K. Tachibana. Polymerization of fluorocarbons in reactive ion etching plasmas. *Journal of Vacuum Science & Technology A*, 16(1):87–95, January 1998.

[105] H. Dersch, J. Stuke, and J. Beichler. Lightinduced dangling bonds in hydrogenated amorphous silicon. *Applied Physics Letters*, 38(6):456–458, March 1981.

[106] Paul E. Barclay, Kartik Srinivasan, Oskar Painter, Benjamin Lev, and Hideo Mabuchi. Integration of fiber-coupled high-QSiNx microdisks with atom chips. *Applied Physics Letters*, 89(13):131108, September 2006.

[107] M. F. Islam, D. E. Milkie, C. L. Kane, A. G. Yodh, and J. M. Kikkawa. Direct Measurement of the Polarized Optical Absorption Cross Section of Single-Wall Carbon Nanotubes. *Phys. Rev. Lett.*, 93(3):037404, July 2004.

[108] Maria Barkelid and Val Zwiller. Photocurrent generation in semiconducting and metallic carbon nanotubes. *Nat Photon*, 8(1):47–51, January 2014.

[109] Arnaud Gloppe, Pierre Verlot, Eva Dupont-Ferrier, Aurélien G. Kuhn, Benjamin Pigeau, Sven Rohr, Alessandro Siria, Philippe Poncharal, Pascal Vincent, Guillaume Bachelier, and Olivier Arcizet. Quantum-limited, cavity-free nano-optomechanical vectorial coupling with sic nanowires

and carbon nanotubes. In *CLEO: 2013*, page JM3A.2. Optical Society of America, 2013.

[110] J. R. Klauder and P. W. Anderson. Spectral Diffusion Decay in Spin Resonance Experiments. *Phys. Rev.*, 125(3):912–932, February 1962.

[111] W. P. Ambrose and W. E. Moerner. Fluorescence spectroscopy and spectral diffusion of single impurity molecules in a crystal. *Nature*, 349(6306):225–227, January 1991.

[112] Kazunari Matsuda, Tadashi Inoue, Yoichi Murakami, Shigeo Maruyama, and Yoshihiko Kanemitsu. Exciton fine structure in a single carbon nanotube revealed through spectral diffusion. *Phys. Rev. B*, 77(19):193405, May 2008.

[113] I. Favero and K. Karrai. Cavity cooling of a nanomechanical resonator by light scattering. *New J. Phys.*, 10(9):095006, September 2008.

[114] A. Eichler, J. Moser, J. Chaste, M. Zdrojek, I. Wilson-Rae, and A. Bachtold. Nonlinear damping in mechanical resonators made from carbon nanotubes and graphene. *Nat Nano*, 6(6):339–342, June 2011.

[115] Arthur W. Barnard, Vera Sazonova, Arend M. van der Zande, and Paul L. McEuen. Fluctuation broadening in carbon nanotube resonators. *PNAS*, 109(47):19093–19096, November 2012.